

Dissertation

submitted to the
Combined Faculty of Mathematics, Engineering and Natural Sciences
of Heidelberg University, Germany
for the degree of
Doctor of Natural Sciences

Put forward by

Maurus Hans

born in Hadamar, Germany

Oral examination on the 8th of November 2022

Physical Computing on a Versatile Setup for Ultra-cold Potassium

Referees: Prof. Dr. Markus K. Oberthaler
Jun.-Prof. Dr. Lauriane Chomaz

Abstract

This thesis reports on a setup for a quasi two-dimensional Bose-Einstein condensate of ^{39}K , which is an isotope well suited for interaction tuning due to a broad magnetic Feshbach resonance, and presents the application of the setup to a specific type of physical computing.

The first part gives an overview of the experimental components to prepare a quasi two-dimensional condensate with a configurable shape. Particular focus is put on the control of the magnetic field for the adjustment of atomic interactions and the configurable potential, which is realized with a digital micromirror device. The imaging setup is presented in detail and a strategy for absorption imaging at high magnetic field is elaborated. This strategy is necessary to properly exploit the magnetic Feshbach resonance. It relies on a scheme for an approximately closed four level optical cycle.

The second part introduces an approach for the implementation of a shallow artificial neural network with a physical system. Subsequently, a specific implementation that utilizes a quasi one-dimensional Bose-Einstein condensate is presented. Regression and interpolation of a non-linear function are performed successfully as a proof-of-concept, and the results are compared for different experimental parameters.

Zusammenfassung

Diese Arbeit beschreibt einen experimentellen Aufbau für ein quasi zweidimensionales Bose-Einstein-Kondensat aus ^{39}K , ein Isotop das aufgrund einer breiten magnetischen Feshbachresonanz gut für die Einstellung der atomaren Wechselwirkung geeignet ist, und stellt die Anwendung des Aufbaus für eine bestimmte Art von physikalischem Rechnen vor.

Der erste Teil gibt einen Überblick über die experimentellen Komponenten zur Herstellung eines quasi zweidimensionalen Kondensats mit einer konfigurierbaren Form. Besonderes Augenmerk liegt auf der Steuerung des Magnetfeldes zur Einstellung der atomaren Wechselwirkung und dem konfigurierbaren Potential, das mit einem Digital Micromirror Device realisiert ist. Der Aufbau wird im Detail vorgestellt und eine Strategie für Absorptionsabbildungen bei hohem Magnetfeld ausgearbeitet. Diese Strategie ist notwendig, um die magnetische Feshbachresonanz voll auszunutzen. Sie beruht auf einem Schema für einen näherungsweise geschlossenen, optischen Vierniveauzyklus.

Im zweiten Teil wird ein Ansatz für die Implementierung eines flachen künstlichen neuronalen Netzes mit einem physikalischen System vorgestellt. Anschließend wird eine konkrete Umsetzung mit einem quasi eindimensionalen Bose-Einstein-Kondensat gezeigt. Regression und Interpolation einer nichtlinearen Funktion werden als Proof-of-Concept erfolgreich durchgeführt, und die Ergebnisse werden für verschiedene experimentelle Parameter verglichen.

Contents

1	Introduction	13
2	Fundamentals	17
2.1	Properties of Potassium	17
2.2	Level Structure and Zeeman Effect	18
2.3	Atom-Light Interactions	22
2.4	Atom-Atom Interactions and Feshbach Resonances	25
2.5	Cooling and Trapping	27
2.5.1	Magneto-optical Traps	27
2.5.2	Sub-Doppler Cooling and Grey Molasses	29
2.5.3	Trapping Potentials and Evaporative Cooling	33
2.6	Bose-Einstein Condensation and Gross-Pitaevskii Equation	35
3	Experimental Tools and Sample Preparation	39
3.1	Experiment Control and Vacuum System	40
3.2	Magnetic Field Setup	42
3.3	Laser Systems	46
3.4	Preparation of the Ultra-cold Sample	48
3.4.1	Magneto-optical Traps	50
3.4.2	Grey Molasses	51
3.4.3	Magnetic Trap	52
3.4.4	Dipole Traps	52
3.5	Arbitrary Trapping Potentials in Two Dimensions	54
3.5.1	Implementation of the DMD	55
3.5.2	Preparation and Characterization of the Quasi One-dimensional BEC	57
4	Absorption Imaging at High Magnetic Field	63
4.1	Closing the Optical Cycle	64

Contents

4.1.1	Scheme for High Field Imaging	66
4.1.2	Optimal Intensity Ratio and Calibration	69
4.2	Overview of the Imaging Setup	73
4.3	ProEM Imaging	75
4.3.1	Characterization of the Objective	78
4.3.2	Imaging Assembly	81
4.3.3	Calibration	83
4.4	Pixis Imaging	84
4.5	Laser System for Imaging	86
5	Physical Computing	89
5.1	Fundamentals	90
5.2	Implementation	93
5.2.1	Physical Encoding	94
5.2.2	Reservoir Evolution and Readout	96
5.2.3	Training Procedure and Overfitting	100
5.3	Experimental Results	104
5.3.1	Evolution Times	104
5.3.2	Averaged Density Profiles	106
5.3.3	Avoid Overfitting	108
5.3.4	Generalization	109
5.4	Discussion	111
6	Final Remarks	115
6.1	Conclusion	115
6.2	Outlook	116
A	Refocussing with Secondary Lens	119
B	Lists of Components	121
B.1	Vacuum Setup and Experimental Control	121
B.2	Laser Setup	122
B.3	Experimental Setup at Science Chamber	124
C	Control Circuits for Magnetic Fields	127
C.1	H-bridge	127
C.2	Passbank	130

D Technical Drawings	133
D.1 Objective (ProEM imaging)	134
D.2 Objective (Pixis imaging)	134
D.3 Distances in Vertical Plane at the Glass Cell	135
D.4 Objective Holder	137
D.5 H-bridge	141
D.6 Passbank	142
List of Publications	143
Bibliography	145
Acknowledgements	157

Introduction

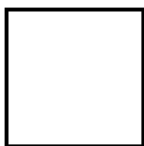
To facilitate calculations and predictions, people have long built computing devices and the oldest known computer dates back to Ancient Greece. It is a sophisticated mechanism used to predict positions of astronomical bodies and eclipses [1]. This mechanism is an example for an analogue computer, which provides a physical model system whose dynamical quantities are utilized for the calculation. With the advances of technology and increased manufacturing precision analogue computers for Fourier analysis [2, 3] or the prediction of tides [4] were developed at the end of the 19th century. The demand for analogue computers significantly increased with World War II as they were used for calculating trajectories for fire control [5] and as guidance system for rockets [6]. With the success of integrated circuits and microprocessors, analogue systems were superseded by their digital counterparts, which are less error-prone to noise and can be universally programmed. Due to this development computers today are predominantly digital computers. However, the implementation of computational tasks with physical systems might become more important again, for example in machine learning [7]. Another example is the field of quantum simulation [8, 9], where results are obtained from a quantum physical model system.

Different physical systems can be employed for quantum simulation, and this thesis focusses on Bose-Einstein condensates, which have become a tool well suited for the task. After being described theoretically by Bose and Einstein in 1924 [10, 11], the first condensates were observed experimentally with dilute atomic gases about 70 years later [12–14]. This coherent state of matter can directly reveal its quantum mechanical nature and its realization opened

the door to many ground-breaking experiments. With the development of new techniques and technological advances ultra-cold systems evolved to a versatile and highly controllable tool. Examples for such developments are optical trapping [15], which can be used to shape optical potentials and enables a multitude of trapping configurations, or magnetic Feshbach resonances [16]. These resonances can be exploited to tune the atomic interactions with an external magnetic field, and thus give easy access to a fundamental parameter of the experiment. The level of control allows for testing of theoretical predictions or the investigation of phenomena not easily described by theory.

The first part of this thesis describes a setup for the preparation and manipulation of a Bose-Einstein condensate of ^{39}K . It is particularly versatile and suitable for simulation tasks as the atomic interaction can be set precisely over a wide range and the shape of the quasi two-dimensional condensate can be controlled. The interaction is set with the help of a broad magnetic Feshbach resonance [17], and the control system for the magnetic field is described in detail in this thesis. A scheme for absorption imaging at high magnetic field is presented, which is necessary to properly exploit the Feshbach resonance. The configurable potential is realized by direct imaging of a digital micromirror device [18, 19], and an overview of the setup is given.

In the second part of this thesis the experimental setup is used to perform a simulation task which is connected to artificial neural networks. After early implementations of neural networks on analogue computers [20] the implementation shifted to digital computers, and machine learning has become a prominent research topic with the advances in digital computer technology over the last decades. A particular framework of machine learning that facilitates its implementation on hardware is reservoir computing [21, 22], which is a non-linear network with a linear output layer. By replacing the non-linear network with a physical system the framework can be applied to very different fields such as photonics, electronics or mechanics [23–25]. In this thesis we utilize a Bose-Einstein condensate and demonstrate the regression and interpolation of a non-linear function as a proof-of-concept. The experiments presented take place predominantly in the classical regime, but they give an interesting perspective on the storage and retrievability of information, and they point the way towards implementations that exploit the quantum mechanical nature of the system. The framework is rather general and the data processing with the linear output layer might be inspiring for other applications.



Structure of the thesis

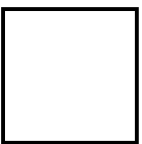
In **chapter 2** concepts of atomic physics relevant for this thesis are discussed, in particular the atomic level structure, interactions, cooling and trapping of atoms and properties of Bose-Einstein condensates.

In **chapter 3** the experimental setup is presented. The magnetic field coils and the laser system for manipulation of the atomic cloud are discussed, and the preparation of the ultra-cold sample is introduced. The setup for trapping the sample with a configurable potential is shown and the resulting quasi one-dimensional cloud is characterized.

In **chapter 4** a scheme for absorption imaging of the atomic cloud at high magnetic fields is introduced. The optimal parameter settings are investigated and the calibration of the column density is discussed. Moreover, the experimental setup for imaging and its implementation is presented.

In **chapter 5** an experimental implementation of a shallow neural network is presented. Basic concepts of machine learning and physical implementations are introduced, and the specific implementation with a BEC as non-linear resource is shown. Parameters of the implementation are varied and their effect on the learning process is investigated.

In **chapter 6** the results of the thesis are summarized, and prospects on experimental upgrades and future projects are given.



CHAPTER 2

Fundamentals

Since the identification of spectral lines by Fraunhofer, the investigation of atomic properties has led to fundamental discoveries, such as the Bohr atom model and quantum mechanics. Over the last century the field of atomic quantum physics has grown rapidly, and it has become not only possible to precisely measure atomic properties, such as resonances, but also to exploit these properties to manipulate atoms. Among many other developments, this led to laser cooling [26] and the experimental realization of Bose-Einstein condensation [12–14].

This chapter gives a short review of some key concepts of atomic physics relevant for the work presented in this thesis. It starts out with the properties of potassium and its level structure. Atomic interactions with light, and with other atoms are discussed. Building on these basic concepts, methods for cooling and trapping of atoms are introduced. The chapter is concluded with a discussion of the phenomenon of Bose-Einstein condensation.

2.1 Properties of Potassium

The experimental setup presented in this thesis makes use of the potassium isotope ^{39}K , and its key properties are given in this section. All values are taken from [27], which gives a good overview of the potassium isotopes. ^{39}K is the most abundant isotope of potassium, which is an alkali with one valence electron. Its electronic spin is thus $S = 1/2$, and the nuclear spin is $I = 3/2$. Being made up from an even number of elementary particles it is a composite

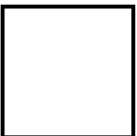
boson. Its level structure at vanishing magnetic field is given in [fig. 2.1](#). The ground state is $^2S_{1/2}$ and the first excited state is split into the levels $^2P_{1/2}$ and $^2P_{3/2}$ due to the fine structure. The transitions between the states are called D1 and D2 line referring to the Fraunhofer D line, which stems from the same atomic transitions in sodium. The states are split further due to the hyperfine structure, leading to the $F = 1$ and $F = 2$ state in the ground state manifold, separated by 461.7 MHz. The hyperfine manifold of the excited states consists of two and four states for $^2P_{1/2}$ and $^2P_{3/2}$, respectively. The manifold of the $^2P_{3/2}$ state features a rather small splitting of only 33.8 MHz, which is close to the natural linewidth of $2\pi \times 6.035$ MHz. The single lines are not resolvable with doppler-free absorption spectroscopy [28] and can not be addressed selectively for cooling in a magneto-optical trap (see [section 2.5.1](#)). In analogy to rubidium systems we call the transitions from the $F = 1$ and $F = 2$ ground state *cooler* and *repumper* transitions, respectively, and the laser systems are called accordingly.

2.2 Level Structure and Zeeman Effect

Alkali atoms are composite particles made from protons, neutrons, and electrons, that each carry an intrinsic spin and may additionally carry orbital angular momentum. However, when probing the atom with optical frequencies, the relevant states can be described by few quantum numbers. This section shortly reviews the level structure of alkali atoms and how it is influenced by an external magnetic field, based on [29, 30, 27].

For our experiments the atoms can be treated as hydrogen-like, and only the ground and first excited state are of interest. The one valence electron is described by its orbital angular momentum \mathbf{L} and spin \mathbf{S} (with quantum numbers L and S , respectively). Due to spin-orbit interaction, these couple together to form the total electronic angular momentum $\mathbf{J} = \mathbf{L} + \mathbf{S}$ with quantum number J , where $|L - S| \leq J \leq |L + S|$ (in integer steps). The angular momentum is responsible for the fine structure of the excited state, which is observed in [fig. 2.1](#) as a level splitting in $J = 1/2$ and $3/2$.

Additionally, there is a further, significantly smaller splitting of the states, called hyperfine splitting. The nucleus as a composite structure has not only a charge but also higher electromagnetic multipole moments. Their interaction with the electron is governed by the nuclear spin \mathbf{I} (with quantum number I). It couples to the electronic angular momentum \mathbf{J} at low magnetic field to form the total angular momentum $\mathbf{F} = \mathbf{J} + \mathbf{I}$ with its quantum number F , for which



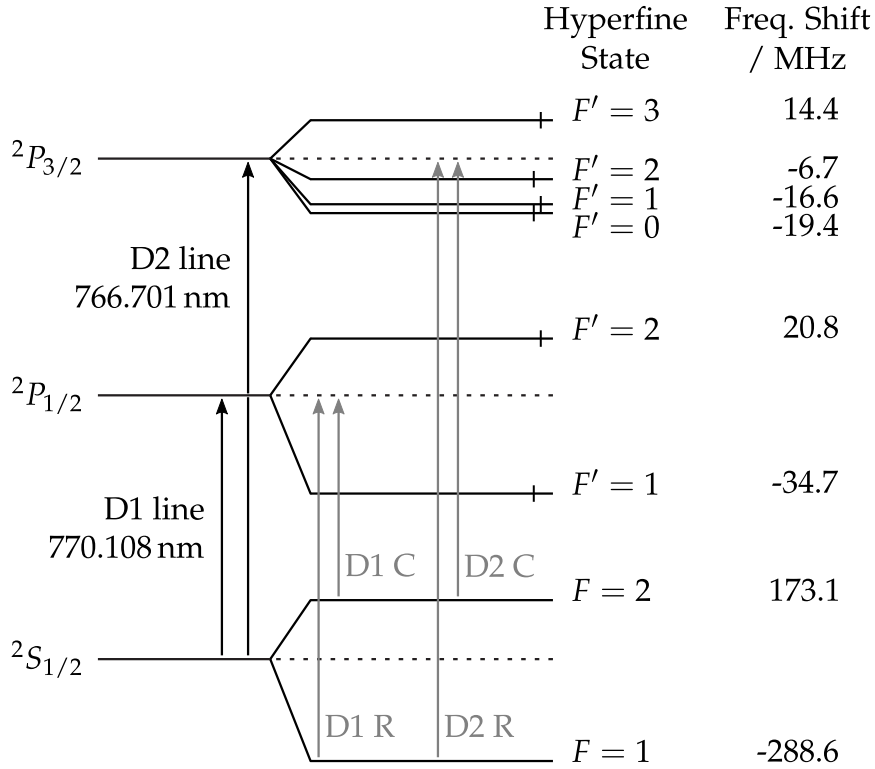


Figure 2.1: Level scheme of ^{39}K . The ground state is $^2S_{1/2}$ and the first excited state exhibits a fine structure splitting into $^2P_{1/2}$ and $^2P_{3/2}$. The transitions from the ground state are called D1 and D2 line, respectively. The ground state consists of two states due to the hyperfine splitting of 461.7 MHz, and in analogy to rubidium we call the transition from the ground state $F = 1$ the cooler (C) and from and $F = 2$ the repumper (R) transition. The excited states are split due to the hyperfine structure, and the natural line widths of the transitions are indicated by the black bars ($2\pi \times 6.035$ MHz for $^2P_{3/2}$). The hyperfine splitting of the excited state is small compared to the natural line width and thus hard to resolve. Values taken from [27].

holds $|J - I| \leq F \leq |J + I|$ (in integer steps). The Hamiltonian describing the hyperfine structure is given by

$$\mathcal{H}_{\text{hfs}} = \frac{a_{\text{hfs}}}{\hbar^2} \mathbf{J} \cdot \mathbf{I} + \frac{b_{\text{hfs}}}{\hbar^2} \frac{3(\mathbf{I} \cdot \mathbf{J})^2 + \frac{3}{2}(\mathbf{I} \cdot \mathbf{J}) - \mathbf{I}^2 \mathbf{J}^2}{2I(2I - 1)J(2J - 1)}, \quad (2.1)$$

where a_{hfs} and b_{hfs} are the magnetic dipole and the electric quadrupole constants, respectively. This completes the contributions to the level scheme at vanishing magnetic field presented in [fig. 2.1](#).

The situation becomes more complicated when a non-vanishing external magnetic field \mathbf{B} is considered. Each state with quantum number F actually consists of $2F - 1$ substates that are degenerate if no magnetic field is present. By applying a field the degeneracy is lifted and the substates exhibit different eigenenergies. This is called the Zeeman effect and can be described by the Hamiltonian

$$\mathcal{H}_Z = \mu_B / \hbar (g_J \mathbf{J} + g_I \mathbf{I}) \cdot \mathbf{B}, \quad (2.2)$$

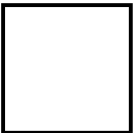
where g_J, g_I are the electron and nuclear g -factors, respectively. Each of the $2F - 1$ magnetic substates is characterized by its magnetic quantum number m_F , which is the projection of the total angular momentum \mathbf{F} onto the magnetic field \mathbf{B} . The quantum number m_F can take the values $-F \leq m_F \leq F$ in integer steps. Without loss of generality we assume the orientation of the magnetic field to be in z -direction, $\mathbf{B} = B_z \hat{z}$. Then, the operator relevant for the projection is F_z . It commutes with the Hamiltonian,

$$[F_z, \mathcal{H}_{\text{hfs}} + \mathcal{H}_Z] = 0. \quad (2.3)$$

This means that for any state there is one quantum number m_F which is a valid description at all magnetic field strengths.

In general, the energy eigenstates can not be described by a single state in the basis of the quantum numbers F, m_F , but the states and the shifts of their energies have to be calculated by diagonalizing the Hamiltonian $\mathcal{H}_{\text{hfs}} + \mathcal{H}_Z$. For the special case of $J = 1/2$ this can be done analytically, resulting in the Breit-Rabi formula [31]. [Figure 2.2](#) shows the resulting energies for the ground state and the $^2P_{3/2}$ excited state manifolds. We assign numbers to the states at high magnetic field, resulting in the states $|g_1\rangle$ to $|g_8\rangle$ and $|e_1\rangle$ to $|e_{16}\rangle$ in the ground and excited state manifolds, respectively.

In the limit of low magnetic field, the eigenstates can be approximated by single states in the F, m_F -basis, and the Zeeman energy shift can be approximated to be linear to the strength of the field \mathbf{B} and to m_F . We can also



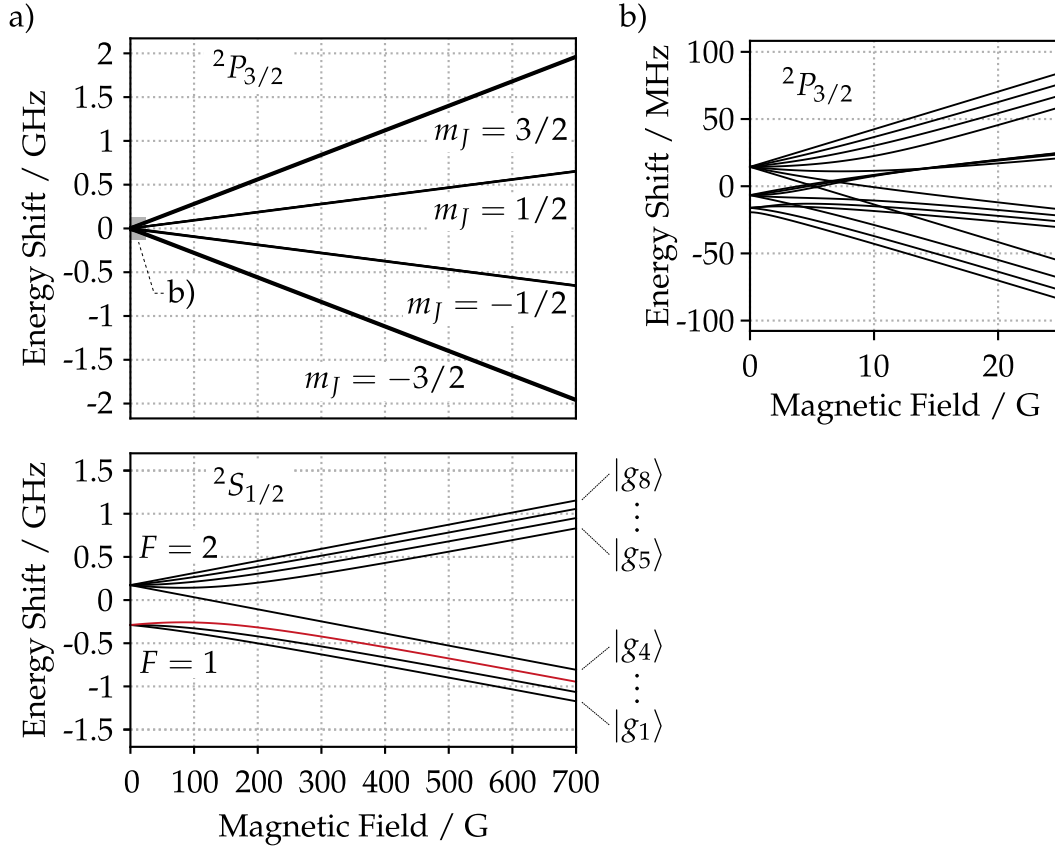


Figure 2.2: Energy shifts of the hyperfine states with external magnetic field. Part a) shows the energy shifts of the levels of the $^2S_{1/2}$ ground state hyperfine manifold (lower graph) and the $^2P_{3/2}$ excited state hyperfine manifold (upper graph). At vanishing magnetic field all magnetic sublevels are energetically degenerate, and the states can be well described by the total angular momentum F , as annotated for the ground states. When a magnetic field is applied, the states reorder according to the Zeeman energy. The transition can be seen in part b) which shows a zoom for the excited states at low magnetic field. At high magnetic field states with the same m_J quantum number group together, which is shown in part a) for the excited state, and the states become pure in the m_J, m_I -basis. We assign numbers to the states at high magnetic field which is shown in the figure for the ground states $|g_1\rangle$ to $|g_8\rangle$. We work mostly with the state $|g_3\rangle$, which is indicated in red and connects to $|F, m_F\rangle = |1, -1\rangle$ at vanishing field.

represent each state in the basis of m_J and m_I , which are the projections of the states momenta \mathbf{J} and \mathbf{I} along the magnetic field, respectively. Similar to the total angular momentum they take values $-J \leq m_J \leq J$ and $-I \leq m_I \leq I$ in integer steps. However, in this basis the state is a superposition of several $|m_J, m_I\rangle$ states, which have to fulfil the requirement $m_F = m_J + m_I$.

Increasing the magnetic field further affects the coupling of the electronic and nuclear angular momenta. The simple representation of the eigenstates in the F, m_F -basis is no longer possible and the energy shifts become more complicated. For very high field the internal coupling between \mathbf{J} and \mathbf{I} can be neglected and both couple to the magnetic field independently (Back-Goudsmit region¹). In this region the eigenstates can be approximated by single states in the m_J, m_I -basis. Then, the energy shift of the states can be estimated directly from eq. (2.2), and it is proportional to $(g_J m_J + g_I m_I) B_z$. The high field limit can be observed in fig. 2.2 a) for the excited state manifold, where the four branches in the plot belong to different m_J states.

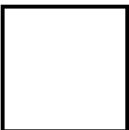
Quantum numbers that allow to describe an eigenstate with a single state are usually called good quantum numbers, making F, m_F good quantum numbers in the low field limit and m_J, m_I good quantum numbers in the high field limit. As a final note, m_F is a good quantum number for all fields (see eq. (2.3)). This simplifies tracing the eigenstates in the Breit-Rabi diagram as states with the same m_F do not cross each other, one knows m_F at low field, and one can easily estimate $m_F = m_J + m_I$ in the high field limit.

2.3 Atom-Light Interactions

The interaction of atoms with an electro-magnetic field is one of the most versatile tools at hand of the experimentalist. This section gives a short introduction to atom-light interactions by showing the key results obtained from a semi-classical model of a two-level atom in a radiation field, following [29].

The atomic model includes a ground and an excited state connected by an atomic transition with frequency ω_0 . It is irradiated with light of frequency ω that is detuned to the atomic transition by $\delta = \omega - \omega_0$. On resonance ($\delta = 0$), the population of the system coherently cycles back and forth between the two states, which is called Rabi cycling. The cycling frequency Ω (Rabi frequency) is proportional to the applied field (i.e. the square root of the intensity) and the

¹Often, Back-Goudsmit is equated with the Paschen-Back regime, which strictly speaking refers to the mixing of the fine structure due to the Zeeman effect [32]. Of course, at a magnetic field that high, the hyperfine structure is mixed as well.



dipole matrix element, which encodes properties of the dipole transition. The interaction with the light changes the eigenstates, and their associated energies shift. This is called light shift and its direction is given by the detuning, where negative detuning (red-detuned) lowers the ground state energy and positive detuning (blue-detuned) raises it.

In addition, the atom can incoherently decay from the excited to the ground state and reset the coherent cycling. This spontaneous process is rather complex as a photon is randomly emitted into one of infinitely many modes, and it can not be properly handled within the theoretical framework presented here. However, we can model the process by an exponential decay of the excited state population with a rate Γ . This is the natural linewidth of the transition, and the decay leads to a natural lifetime of the excited state of $\tau = 1/\Gamma$. The exponential decay and the before-mentioned model lead to a set of differential equations, the optical Bloch equations, that describe the dynamics of the system.

Solving the optical Bloch equations for the steady state reveals some interesting properties of the system. The initial coherences from the Rabi cycling process have decayed due to the incoherent decay of the excited state. This limits the steady state population ρ_{ee} of the excited state to be at most equal to the population ρ_{gg} of the ground state. Specifically, the imbalance between the two states is given by

$$w = \rho_{gg} - \rho_{ee} = \frac{1}{1 + s} , \quad (2.4)$$

with the off-resonance and on-resonance saturation parameter given by

$$s = \frac{s_0}{1 + (2\delta/\Gamma)^2} , \quad s_0 = \frac{2|\Omega|^2}{\Gamma^2} = I/I_{\text{sat}} . \quad (2.5)$$

The last term defines the on-resonance saturation intensity I_{sat} as the light intensity where the Rabi frequency equals the spontaneous decay rate. It is given by

$$I_{\text{sat}} = \pi \hbar c \frac{\Gamma}{3\lambda_0^3} = \frac{\hbar}{12\pi c^2} \omega_0^3 \Gamma , \quad (2.6)$$

where λ_0 and ω_0 are the wavelength and frequency at resonance. The saturation process limits the total scattering of photons from a laser beam, which is given by the product of the decay rate Γ of the excited state and its population

ρ_{ee} . Keeping in mind that the population is normalized to one, the latter can be extracted from eq. (2.4) and the total scattering rate γ is estimated to be

$$\gamma = \Gamma \rho_{ee} = \frac{\Gamma}{2} \frac{s_0}{1 + s_0 + (2\delta/\Gamma)^2}. \quad (2.7)$$

In the limit of very high intensities the scattering saturates $\gamma \rightarrow \Gamma/2$.

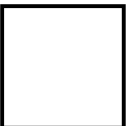
Due to the interaction with the light field the atoms can experience a force. Commonly, this force is separated in two parts, where one is important if the frequency of the light field is close to resonance and the other if it is far away. Close to resonance, atoms scatter photons as discussed above, and these photons carry a momentum $\hbar k$. When the atom absorbs and emits a photon, the total momentum of the scattering process has to be conserved and thus the momentum of the atom has to change accordingly. As the atom absorbs photons from the light field where they all share the same momentum, but subsequently emits the photons spontaneously in random directions, contributions of the latter average out. Thus, a net momentum is transferred and the atom experiences a force proportional to the number of scattered photons, which is called scattering or radiative force.

Far away from resonance, the scattering of photons ceases as described by eq. (2.7). However, the light shift of the atomic levels is still present, and the energy shift ΔE_g of the atom's ground state far away from resonance ($\Omega \ll |\delta|$) is given by

$$\Delta E_g = \frac{\hbar \Omega^2}{4\delta} = \frac{3\pi c^2}{2\omega_0^3} \frac{\Gamma}{\delta} I, \quad (2.8)$$

where we used eq. (2.5) and eq. (2.6) to derive the expression on the right. The energy shift depends on the Rabi frequency and therefore on the intensity of the light. A spatially varying intensity is experienced by the atom like a spatial potential, and associated forces act on the atom. This force is commonly called the dipole force.

For multi-level atoms, the situation becomes slightly more complicated. Whether a transition between two states can take place depends in general on the dipole matrix element that couples the states. Still, knowing the quantum numbers of the states one can make use of a set of transition rules to estimate possible transitions. These rules ensure the conservation of angular momenta in the atom-photon system. This means in particular that the magnetic quantum number can only be changed by $\{-1, 0, +1\}$ when the atom absorbs a photon of polarization $\{\sigma^-, \pi, \sigma^+\}$. For emission, the polarizations are reversed.



2.4 Atom-Atom Interactions and Feshbach Resonances

In the scope of ultra-cold atomic experiments, interactions between atoms play an important role. They are vital during evaporative cooling, which is necessary to reach Bose-Einstein condensation, but may also contribute to unwanted atom losses. Depending on the atomic species, the interaction between the atoms can be controlled by a Feshbach resonance. This section gives a short introduction and mainly follows [33], where scattering theory and Feshbach resonances are discussed in more detail. A comprehensive review is given in [34].

The interaction between two neutral atoms is often described by a van der Waals potential with an attractive part and a short-range repulsive part, as sketched in fig. 2.3 a) for the open channel. Scattering can in general be described by a partial wave expansion of ingoing and outgoing waves that solve the Schrödinger equation in the potential. At the low temperatures of our atomic sample the typical particle wavelength is much larger than the interaction potential. Hence, the form of the potential plays a minor role and the complicated scattering problem boils down to spherically symmetric contact interactions. A single parameter is sufficient for its description, which is the s-wave scattering length a . The scattering process leads to a phase shift $\delta = -ka$ between an ingoing wave with momentum k and the outgoing wave. It is directly connected to the effective atomic interaction, where a negative scattering length means attractive interactions and vice versa.

So far, the description only took into account the single-channel problem, where the atomic states are unaltered. Mostly, this is a good approximation for alkali atoms at low temperature. However, the properties of the scattering in one channel can be significantly altered by a nearby bound state in a closed channel. This is called a Feshbach resonance. A sketch of the potentials is provided in fig. 2.3 a), where a bound state with energy E_{res} in the closed channel and the open channel with threshold energy E_{th} are shown. If the energies are close, atoms can form an intermediate bound state during the scattering event. This molecular state is not stable due to energy and momentum conservation, but it strongly influences the scattering process and hence the s-wave scattering length a . In our case, the energy of the bound state can be shifted by an external magnetic field. This leads to a magnetically tuned Feshbach resonance, which can be described by

$$a(B) = a_{\text{bg}} \left(1 - \Delta / (B - B_0) \right) . \quad (2.9)$$

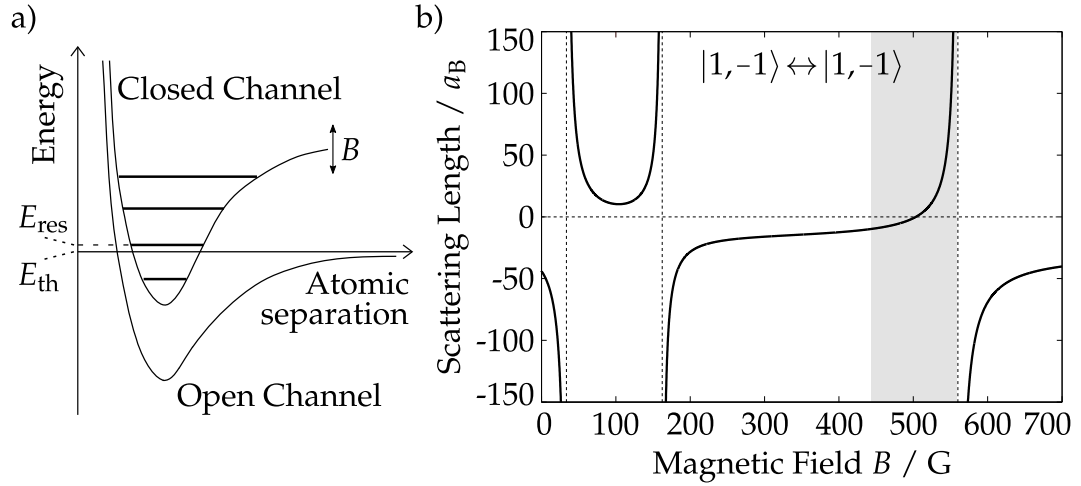


Figure 2.3: Feshbach resonances in ^{39}K . Part a) shows a sketch of the energy versus the separation of two atoms. The lower curve depicts the scattering potential (open channel) with the threshold energy E_{th} for infinite distance, and the upper curve the molecular potential (closed channel) with bound states. The energy of a bound state is indicated with E_{res} , and it can be tuned via an external magnetic field B . When the energy E_{res} matches the threshold energy E_{th} , a Feshbach resonance occurs. Although a bound state can not be formed due to momentum conservation, the atoms can scatter to an intermediate state in the closed channel. This coupling varies the interaction between the atoms and hence the scattering length. For our atomic species ^{39}K , this is indicated in part b) for the intra-species resonances between atoms in the state $|F, m_F\rangle = |1, -1\rangle$. The scattering length is negative at vanishing magnetic field, and preparation of the atomic sample and the experiments take place close to the resonance at 562 G (shaded area). Part a) adapted from [33], part b) adapted from [35].

The background scattering length a_{bg} corresponds to the scattering length far off resonance, the field B_0 to the magnetic field exactly on resonance, and the parameter Δ to the width of the resonance.

For our ground state $|g_3\rangle$, which corresponds to $|F, m_F\rangle = |1, -1\rangle$ at low magnetic field, the intra-species resonances are depicted in fig. 2.3 b). As the scattering length is below zero at vanishing magnetic field, most experiments are performed at the broad resonance at $B_0 = 562.2$ G (shaded area). It has a width of $\Delta = 55$ G [17] and thus allows for a good adjustment of the atomic interaction over a broad range, covering negative and positive



interactions. The other ground states of the $F = 1$ manifold exhibit a similar broad resonance at a slightly lower field.

2.5 Cooling and Trapping

The following section gives an introduction to the cooling and trapping techniques used at our experiment to prepare ultra-cold atomic samples. This section follows the typical experimental sequence starting at high temperatures with dissipative methods that rely on photon scattering, such as the magneto-optical trap and grey molasses. Subsequently, we focus on conservative traps and discuss further cooling to very low temperatures via evaporation. The section is based on [29] and gives additional information specific to our atomic species ^{39}K .

2.5.1 Magneto-optical Traps

The magneto-optical trap (MOT) is one of the workhorses of cold atom physics, and a starting point for many experiments. It combines cooling in velocity space and trapping in real space, and relies on the radiative force from the scattering of photons.

Figure 2.4 provides a sketch that shows the working principle of a MOT in one dimension. The cooling in velocity space is implemented as follows. From the left and the right laser light is shone in with the same handedness and frequency ω_L . It is red-detuned to the atomic transition by δ . For a moving atom the frequency of the laser beam appears shifted by the Doppler effect. While it is red-shifted further away from the resonance of the transition when the atom moves along the beam, it is blue-shifted into resonance if the atom moves in opposite direction to the beam. Hence, an atom is more likely to scatter photons if it is counter-propagating the laser beam and is slowed down by the resulting radiative force. This is called Doppler cooling.

Additionally, spatial confinement is realized with an inhomogeneous magnetic field. A simplified level scheme is sufficient to understand the principle, and fig. 2.4 shows a single ground state with magnetic quantum number $m = 0$ and an excited state with three magnetic substates. The magnetic field is zero in the centre and increases outwards, which lifts the degeneracy of the substates $m \in \{-1, 0, 1\}$ due to the Zeeman effect. Note that the lower branch always belongs to the state $m = -1$ as the direction of the magnetic field is reversed in the centre. The spatial dependence of the magnetic field

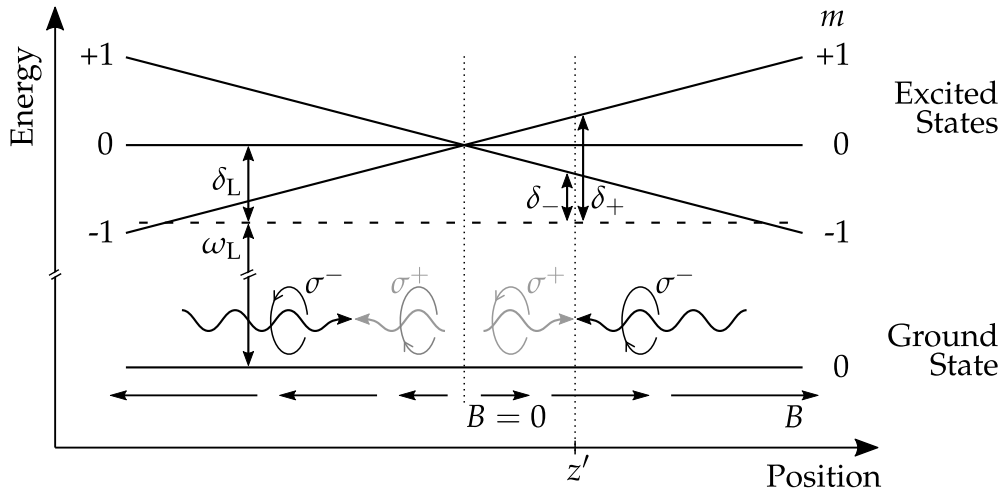
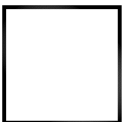


Figure 2.4: Working principle of a magneto-optical trap in one dimension. The sketch shows a simplified level structure with one ground state and an excited state with three magnetic substates, $m \in \{-1, 0, +1\}$. Their degeneracy is lifted by an inhomogeneous magnetic field B , which is zero at the centre of the trap and increases outwards. The energy of the levels is indicated by the black lines, where the labelling of the magnetic substates switches in the centre as the magnetic field changes direction. From both sides circular polarized laser light with the same handedness and with frequency ω_L is shone in (black wavy arrows). It is red-detuned to the $m = 0$ state by δ_L and can drive σ^- transitions when incoming (black) and σ^+ transitions after crossing the centre (grey). With this setup two mechanisms can be exploited. First, velocity-dependent scattering processes slow down atoms that move away from the centre due to the Doppler effect. Atoms that move in opposite direction to the laser see the frequency blue-shifted into resonance. Second, space-dependent scattering processes accelerate the atoms towards the centre. The inhomogeneous magnetic field shifts the level structure of the atoms due to the Zeeman effect. Hence, the detuning δ_- of the substate $m = -1$ is shifted into resonance while the detuning δ_+ of the substate $m = +1$ is shifted further away, as it is indicated at position z' . This enhances scattering with the incoming laser light (indicated in black) and leads to a confinement at the centre of the trap. The principle can be applied in three dimensions.



directly translates to the detunings δ_- and δ_+ of the $m = -1$ and $m = +1$ state, respectively. Going away from the centre, the $m = +1$ state is tuned further out of resonance, while the $m = -1$ state is tuned in resonance. As the latter state is addressed only by the σ^- light, which points in the direction of the centre, a radiative restoring force keeps the atoms in the centre close to the zero-point of the magnetic field.

The principle can be extended to three dimensions with three pairs of counter-propagating laser beams and a quadrupole magnetic field. A big advantage of the MOT is that it can capture and cool atoms from room-temperature background gas, as it has a large capture velocity range. This results from atoms being slowed over an extended distance in the gradient field, when the Doppler shift of the resonance is compensated by the change of the magnetic field. Finally, the temperature of the atomic cloud is limited by the residual scattering of photons. It is called the Doppler temperature $T_D = \hbar\Gamma/(2k_B)$, with Γ the natural linewidth of the transition.

For multi-level atoms the picture becomes slightly more complicated. The MOT is usually realized with the cooling transition $F = 2 \rightarrow F' = 3$ (cf. level scheme in fig. 2.1), where the atoms are pumped to the stretched states $|F, m_F\rangle = |2, \pm 2\rangle$ and $|F', m_{F'}\rangle = |3, \pm 3\rangle$ by the circularly polarized light. Technically, this would lead to a closed transition. In the $F' = 3$ excited state hyperfine manifold of ^{39}K , however, the different substates are energetically very close, and the atoms are also excited to the other states. From these states, atoms can decay back to the $F = 1$ ground state where they are not addressed by the light. To excite the atoms from the $F = 1$ ground state a second laser beam is employed that repumps the atoms back to the $F = 2$ ground state, therefore the laser is usually called repumper. For rubidium, the atom loss is a small effect and a low repumper intensity is sufficient. In ^{39}K the decay is significant and equal intensities of cooling and repumping light are used, leading to a rather high temperature on the order of 1 mK for the MOT [36].

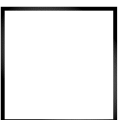
2.5.2 Sub-Doppler Cooling and Grey Molasses

Cooling below the Doppler limit was completely unexpected when observed for the first time [37]. It made the necessity of theoretical models beyond the simple two-level atom obvious, as the multi-level structure and optical pumping between the states has to be taken into account for the explanation of the phenomenon. This chapter gives a short introduction to Sisyphus cooling, a prominent sub-Doppler technique, and grey molasses cooling.

Sisyphus cooling utilizes two effects, the non-adiabatic movement of atoms in a light field potential and associated optical pumping effects. This part follows [38], and we restrict ourselves to the case of linear polarizations. The principle of the mechanism is depicted in fig. 2.5 a). In our example, the light field is provided by two counter-propagating laser beams with orthogonal polarization, which is called $\text{lin}\perp\text{lin}$ configuration. This leads to a spatial gradient of the polarization, which switches back and forth between linear and circular. The model atom has two ground states $|g_{-1/2}\rangle$ and $|g_{+1/2}\rangle$ with associated magnetic quantum numbers $m = \mp 1/2$, respectively. For red-detuned light these states experience a negative light shift that depends on the polarization of the light. Hence, the energy of the ground states varies with the position and is shown in the centre of fig. 2.5 a). Additionally, the populations of the steady-state of resting atoms are indicated by the size of the black dots. The energy of the two ground states alternates spatially, and the state with lower energy is always favoured. An atom with finite velocity moves non-adiabatically through this potential and trades its kinetic energy with potential energy, as shown in the lowest graph. If the atom reaches the top of the curve it has gained the maximal amount of potential energy. When excited at this position, the atom is likely to spontaneously decay to the lower state due to the circular polarization of the light. The decay radiates away the energy difference between the two ground states. The atom is thus cooled, and the process can be repeated until it has not enough energy left to climb the potential hill any more.

Often, the cooling scheme is realized using counter-propagating beams with σ^+ and σ^- . This leads to a linear polarization of the laser beam which rotates spatially. The theoretical description is very different as no light shifts appear in the rest frame of the atom. However, transforming to the rotating frame of the polarization for a moving atom leads to shifts in the energy of the states and an unbalanced interaction with the counter-propagating laser beams, which provides the cooling.

The scheme can be extended to three dimensions with three pairs of beams as before for the MOT. This leads to more complicated polarization geometries where both $\text{lin}\perp\text{lin}$ and $\sigma^+-\sigma^-$ play a role. While the former dominates for large detuning, the latter is more important in the region of small detuning [39]. For ^{39}K the conventional Sisyphus cooling proves difficult due to the small hyperfine splitting of the $^2P_{3/2}$ excited state. Still, temperatures as low as $25\ \mu\text{K}$ have been reached [40, 41, 36].



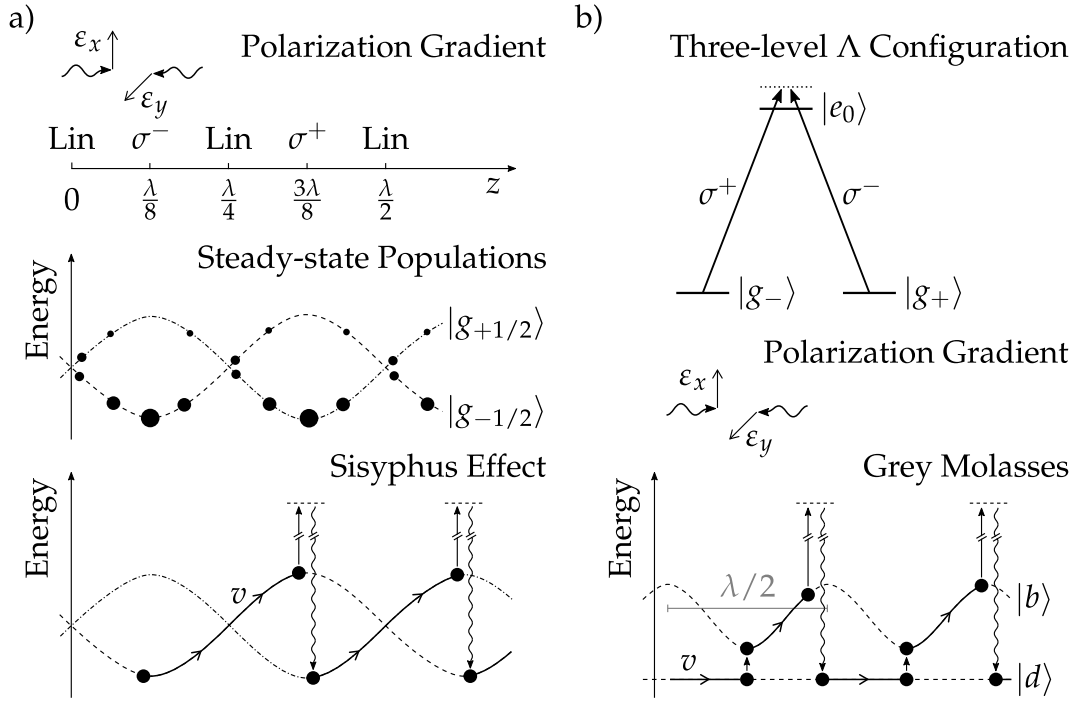


Figure 2.5: Sisyphus and grey molasses cooling. Part a) shows the principle of Sisyphus cooling. A polarization gradient is created by two counter-propagating laser beams with orthogonal polarization (lin \perp lin), resulting in a polarization that goes back and forth between linear and circular. The atomic ground states $|g_{-1/2}\rangle$ and $|g_{+1/2}\rangle$ experience a light shift that spatially modulates the energy of the states. In the steady-state, most atoms populate the lower state as indicated by the size of the black dots. When an atom moves non-adiabatically with velocity v it can trade kinetic with potential energy. Scattering a photon in the maximum of the potential it will most likely decay back to the lower state. The difference in energy is dissipated by the spontaneous emission and leads to cooling of the atom. In part b) the ingredients for grey molasses cooling are depicted. When hitting the Raman condition in a three-level Λ configuration the two ground states $|g_-\rangle$ and $|g_+\rangle$ can be rewritten in a dark state $|d\rangle$ and a bright state $|b\rangle$. For an atom at rest only the latter state couples to the excited state $|e_0\rangle$. At a finite velocity the Raman condition is not fulfilled and $|d\rangle$ is not stationary. Thus, only resting atoms are trapped in the dark state (VSCPT). Similar to Sisyphus cooling, a polarization gradient can be applied by the incoming light which modifies only the energy of the bright state. Motional coupling can transfer atoms from $|d\rangle$ to $|b\rangle$ when the states are energetically close. Subsequently, potential and kinetic energy can be traded and dissipated via excitation and spontaneous emission, resulting in cooling of the atom. Part a) adapted from [38].

Grey molasses cooling combines velocity-selective coherent-population trapping (VSCPT) with Sisyphus cooling. First, we introduce VSCPT following [42]. It is a sub-recoil scheme that keeps resting atoms in a dark state. An effective three-level Λ system is necessary for the technique, which is depicted in fig. 2.5 b). The two ground states $|g_{-}\rangle$ and $|g_{+}\rangle$ have magnetic quantum numbers $m = \mp 1$, respectively. They are connected to an excited state $|e_0\rangle$ with $m = 0$ by the transitions σ^{+} and σ^{-} . These transitions are in Raman condition, which means that they have the same detuning relative to the excited state. We can rewrite the ground states in the superpositions $|d\rangle = |g_{-}\rangle + |g_{+}\rangle$ and $|b\rangle = |g_{-}\rangle - |g_{+}\rangle$. For an atom at rest one can show that $|d\rangle$ is a dark state that does not couple to the excited state, whereas the bright state $|b\rangle$ does. For a moving atom, however, the Raman condition is not fulfilled any more due to Doppler shifts. On the level of the states this means that the dark state $|d\rangle$ is no energy eigenstate of the moving atom, and if the atom is initially in $|d\rangle$ it will eventually be transferred to the bright state $|b\rangle$. In this state it can scatter photons and experience associated changes in velocity. These changes are in the fashion of a random walk, which means that there is no spatial dependence of energy of the bright state. The energy diagram shown at the bottom of fig. 2.5 b) would have two flat lines for dark and bright state for the VSCPT scheme. The cooling of the atoms relies only on the decreasing transfer probability to the bright state, as the atom spends more time in the dark state the slower it becomes, and random changes of the atomic velocity due to scattering. This is a diffusive process, but ultimately atoms might reach temperatures below the photon recoil as the last emitted photon may leave the atom at a velocity close to zero.

To enforce the cooling process instead of relying on diffusion, one can combine VSCPT with sub-Doppler cooling. We follow [43] for a short discussion of the technique. As for Sisyphus cooling, two counter-propagating beams with orthogonal linear polarization are employed to form a gradient of the polarization. The bright state $|b\rangle$ couples to the excited state and is affected by light shifts, while the dark state $|d\rangle$ is not. An atom that is moving in the dark state can be transferred to the bright state via a non-adiabatic passage, which is also called motional coupling. One can show that this takes place predominantly at the valleys of the bright state as indicated in fig. 2.5. If the light frequency is blue detuned to the resonance of the transition, light shifts lead to an increase of the bright state's energy. As before, the atom can climb the resulting potential hill and trade potential energy with kinetic energy. Being in the bright state the atom can be excited and decay back to



the dark state, and the energy difference is radiated away by the process of spontaneous emission. This procedure repeats until the atom is sufficiently slow to stay in the dark state where no further scattering takes place.

Experimentally, the complicated level structure of Alkali atoms permits no strictly dark states, but there are grey states that couple only weakly to the excited states and can be utilized. Furthermore, the technique we discussed in one dimension can be applied in three dimensions by using three pairs of light beams. For the species ^{39}K the first successful implementations were realized on the D1 transition (cp. fig. 2.1) coupling both $F = 1$ and $F = 2$ ground states to the excited state $F' = 2$ in a $\sigma^+ - \sigma^-$ configuration [44, 45]. Thus, two light frequencies in Raman condition are necessary, which are both blue detuned to the excited state hyperfine manifold. The publications report temperatures as low as $6\ \mu\text{K}$.

2.5.3 Trapping Potentials and Evaporative Cooling

Laser cooling has a practical limit, which is typically on the order of $1\ \mu\text{K}$. To achieve the lower temperatures and high phase-space densities necessary for Bose-Einstein condensation traps for neutral atoms and cooling techniques are needed that do not rely on the scattering of photons.

Magnetic traps confine atoms by the interaction of a magnetic field \mathbf{B} with the magnetic moment $\boldsymbol{\mu}$ of the atom. As discussed in section 2.2, the level structure of an atom shifts with the strength of an external magnetic field due to the Zeeman effect. For a spatially inhomogeneous field this leads to a conservative potential and an associated force $\mathbf{F} = \nabla(\boldsymbol{\mu} \cdot \mathbf{B})$, which is experienced by the atom. The energy shifts of the levels can be read of in the Breit-Rabi diagram (cf. fig. 2.2). A state with a positive slope is attracted to a low field (low field seeker) to minimize its energy, and vice versa (high field seeker). For realistic setups these energy shifts are small compared to the energy of particles at room temperature, which makes pre-cooling of the atomic sample necessary.

A static magnetic field may have local minima while local maxima are forbidden [46], and the simplest configuration with a local minimum is a quadrupole field produced by two identical coils with opposed currents. This configuration has zero field at the central point, and from there the field strength rises in all directions. It thus traps low field seekers. However, the configuration is impractical for very low temperatures as losses can occur

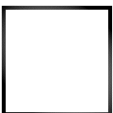
at the zero point due to spin flips into a high field seeking state (Majorana losses). More complex geometries or a time-dependent magnetic field can circumvent this problem.

In our setup a simple quadrupole trap is included for intermediate trapping, state selection and compression. It traps the ground state $|g_3\rangle$, which is connected to $|F, m_F\rangle = |1, -1\rangle$ at low field and the only low field seeker of the $F = 1$ substates. For our application, losses play no role as the cloud is too hot.

Dipole traps provide a conservative potential in space by inducing a dipole moment via atom-light interaction. This results in a shift of the internal levels of an atom in presence of a laser beam that is detuned from resonance (cf. section 2.3). When the light is red-detuned to the resonance the atomic ground state levels are shifted to lower energies, and vice versa. Similar to magnetic traps this leads to a potential landscape depending on the spatially varying intensity I of the light. Associated with this potential is a trapping force that is proportional to derivative ∇I . Thus, atoms are attracted to regions of maximal intensity for red-detuned light while they are repelled from those regions for blue-detuned light. Usually, the potential minimum of a trap is approximated by a harmonic trap and experimentally characterized by its trap frequency f . A comprehensive overview and quantitative analysis of optical dipole traps can be found in [47].

The most simple red-detuned (attractive) dipole trap is a focussed Gaussian beam. It is characterized by its width in the focus, called the beam waist w_0 . The divergence of the beam and thus the steepness of confinement along the beam is described by the Rayleigh range $z_R = \pi w_0^2 / \lambda$, where λ is the wave length of the light. It is the distance from the focus, where the beam width w has increased to $w = \sqrt{2}w_0$. By overlapping several Gaussian beams, different trap shapes and a strong confinement in all directions can be realized.

Repulsive traps with blue-detuned light are typically more complicated to set up, as the light has to encase the atomic cloud. They have the advantage that atoms are confined in regions of low intensity, which reduces scattering and associated heating effects. There are many techniques to form laser beams for trapping, and we restrict ourselves to two that are relevant for our experimental setup. The first technique uses the interference between two laser beams under a shallow angle to create a standing wave. As the light repels the atoms, they are trapped in between the resulting sheets of light. Such a trap is often referred to as a pancake trap, and it traps the atoms in one



dimension. The second technique makes use of a digital micromirror device (DMD), which is an array of small mirrors that can be addressed individually [48]. Imaged onto the atomic cloud it can provide configurable trapping potentials in two dimensions [18].

Evaporative cooling relies on the scattering of atoms among each other in the atomic cloud instead of atom-light scattering. The scattering processes distribute the energy among the atoms and allow for the development of a thermal cloud. Evaporative cooling slowly removes atoms with high energies while letting the remaining atoms redistribute their energies and rethermalize by elastic collisions. This leads to a lower temperature of the remaining atoms. The evaporation is usually forced by lowering the trap depth for dipole traps or cutting away atoms with an rf knife for magnetic traps. To achieve good cooling it is important that the rethermalization is faster than the cooling rate. The final temperature is limited by the number of atoms in the beginning and atom loss due to inelastic collisions.

For ^{39}K two challenges have to be overcome for successful evaporative cooling to a Bose-Einstein condensate that are both connected to the inter-atomic interaction strength. First, the background interaction at vanishing magnetic field is negative and small (cp. fig. 2.3). This prevents efficient rethermalization and leads to a collapse of the atomic cloud at sufficiently low temperatures as the atoms effectively attract each other [49]. It can be prevented by keeping the atomic cloud in a dipole trap and applying a homogeneous magnetic field to tune the interaction strength to a positive value with the help of a Feshbach resonance. Second, the sample has to be pre-cooled sufficiently as the collisional cross-section has a Ramsauer minimum at $400\ \mu\text{K}$ [50]. This can be overcome with the grey molasses described above.

2.6 Bose-Einstein Condensation and Gross-Pitaevskii Equation

A major task of our experimental setup is the preparation of a Bose-Einstein condensate (BEC), as this is the starting point for most of our experiments. This section gives all information and theoretical descriptions for BECs that are relevant for this work, mainly based on [29, 51, 52].

A BEC is a state of matter that forms in a dilute gas of bosons when the

phase space density exceeds a critical value of

$$n\lambda_{\text{dB}}^3 \geq \zeta(3/2) \approx 2.61, \quad (2.10)$$

where n is the spatial density, λ_{dB} the thermal de Broglie wavelength and ζ the Riemann zeta function. In a simplified picture, the indistinguishable particles can be viewed as wavepackets with an extent on the order of λ_{dB} , which increases with lower temperature. For sufficiently low temperatures and high densities, these atomic wavepackets overlap and synchronize, forming a macroscopic matter wave. More formally, the transition to a BEC can be explained using the Bose-Einstein distribution for non-interacting, indistinguishable particles. At sufficiently low temperatures it features an energy minimum for a macroscopic population of the lowest state and infinitesimally populated higher states.

Theoretically, the mean-field dynamics of a BEC in three dimensions can be described by the **Gross-Pitaevskii equation** (GPE),

$$i\hbar \partial_t \psi(\mathbf{x}, t) = \left(-\frac{\hbar^2}{2m} \nabla^2 + V(\mathbf{x}) + g_{3\text{d}} |\psi(\mathbf{x}, t)|^2 \right) \psi(\mathbf{x}, t), \quad (2.11)$$

with mass m , external potential V and interaction strength $g_{3\text{d}}$. The order parameter $\psi(\mathbf{x}, t)$ is the complex wave-function of the macroscopically populated ground state of the condensate, and it is often written as $\psi = |\psi| \exp(i\phi)$ with condensate density $n = |\psi|^2$ and phase ϕ . The interaction strength is given by

$$g_{3\text{d}} = \frac{4\pi\hbar^2 a}{m}, \quad (2.12)$$

where a is the s-wave scattering length. This description is valid under the assumption of contact interactions, which is justified in the low temperature regime of BECs.

To estimate the reaction of the BEC to an external potential a helpful quantity is the **healing length** of the system. It is defined as

$$\xi = \frac{\hbar}{\sqrt{2mng}}, \quad (2.13)$$

and it gives a length scale on which the system reacts to potential edges or impurities. For the example of an infinite potential wall the healing length



gives a length scale on which the density drops from the background density to no density at the wall.

In the limit of a slowly varying density the kinetic term in the GPE can be neglected, which is called **Thomas-Fermi approximation**. The equation simplifies significantly and one obtains

$$\mu = V(\mathbf{x}) + gn(\mathbf{x}) , \quad (2.14)$$

where μ is the ground state chemical potential, and the atomic density distribution $n(\mathbf{x})$ is determined by the trapping potential. The expression simplifies further to

$$\mu = gn \quad (2.15)$$

for a flat background potential.

An analytic treatment of small density perturbations on a large condensate background can be derived with Bogoliubov theory. The details are given in [52], and we only discuss few points relevant for this thesis. The theory allows to construct the eigenmodes of the weakly interacting system from a set of non-interacting eigenmodes. The resulting quasi-particles give a description of the elementary excitations of the weakly interacting system. Their corresponding dispersion relation is the **Bogoliubov dispersion relation**

$$\hbar\omega = \sqrt{\frac{\hbar^2 k^2}{2m} \left(\frac{\hbar^2 k^2}{2m} + 2\mu \right)} , \quad (2.16)$$

where $\hbar\omega$ is the energy associated with a spatial mode k . In the limit of small momenta the dispersion relation becomes linear,

$$\omega \simeq c_s k , \quad c_s = \sqrt{\mu/m} , \quad (2.17)$$

where c_s is the speed of sound of the system.

By a very strong confinement of the condensate in two directions, a **one-dimensional gas** can be created. We assume a harmonic confinement with equal trapping frequencies $\omega_x = \omega_y = \omega_\perp$ in those directions. Strong confinement is achieved if the energy associated with the radial trapping frequency is big compared to the chemical potential of the system, $\hbar\omega_\perp \gg \mu$, which means that only the lowest oscillator mode in the harmonic trap is occupied. For the description of such a system the GPE can be reduced to one dimension

by replacing the three-dimensional order parameter with a one-dimensional one (connected to a line density) and the spatial derivatives accordingly. The interaction strength changes to

$$g_{1d} = \frac{4\pi\hbar^2 a}{m} \frac{1}{2\pi l_{\perp}^2} = 2\hbar\omega_{\perp} a, \quad (2.18)$$

with ω_{\perp} the radial trapping frequency and $l_{\perp} = \sqrt{\hbar/(m\omega_{\perp})}$ the associated harmonic oscillator length [53].

Throughout this thesis energies E are typically given as frequencies $f = \omega/(2\pi)$, in the sense of $E = \hbar\omega = hf$. SI units can be retrieved by multiplying with Planck's constant h .



Experimental Tools and Sample Preparation

To prepare a BEC a specialized machine and precise equipment is needed for trapping, cooling and manipulating atoms. The first BECs were created with rubidium and sodium [12, 13], and early experiments with lithium proved difficult due to instabilities arising from attractive interaction [14]. For similar reasons the preparation of a BEC of ^{39}K is no easy task, and it was first achieved by using sympathetic cooling with rubidium [54]. Utilizing a bright molasses led to the first direct preparation of a BEC of ^{39}K [50], and the preparation was improved further by employing grey molasses cooling [55].

In this chapter we give an overview of the preparation of a BEC in a configurable quasi two-dimensional potential. The first part describes the experimental setup, namely the control system and the vacuum system, the magnetic field setup and the laser setup. Next we discuss the preparation of a BEC with the apparatus and give an overview of the different stages of cooling and trapping. The last part presents the implementation of the DMD, the configuration of the trapping potential for a quasi one-dimensional BEC, and the characterization of the trap and the atomic cloud. A comprehensive list of the components used for the different parts of the experimental setup is given in appendix B.

Our experimental work builds upon results from other potassium setups [36, 56–58], new cooling strategies [44, 55] and experiences with novel trapping setups [59]. Moreover, our setup and results discussed in this section are based upon the work of our bachelor and master students that helped to set up the

main magnetic coils [60], the magnetic offset coils [61], the master laser system and spectroscopy [28], the frequency generation for the grey molasses [62], and designed and tested the DMD system [63]. A thorough overview of our setup and of the preparation of the ultra-cold sample is also given in [35], which this section is partly based on.

3.1 Experiment Control and Vacuum System

The experiment is interfaced with a computer control system by dedicated hardware, which is essentially a complex arbitrary function generator and provides a sequence of voltages to control the individual components of the experiment. The system has 80 digital TTL outputs and 32 digital-to-analog converters with a resolution of 0.3 mV and a range from -10 V to 10 V. Furthermore, the system features analog-to-digital inputs, which are used for monitoring purposes. The time resolution of the experiment control is set to $50 \mu\text{s}$ in order to allow for sufficiently long sequences. If faster switching of control signals is necessary, we use dedicated function generators that are triggered by the experimental control system. Details on the setup and the programming of the system can be found in [64].

The vacuum chamber of the experiment was originally designed for a mixture experiment and a comprehensive description can be found in [65, 66]. It is depicted in [fig. 3.1](#) and consists of two chambers connected by a differential pumping stage, which is implemented with a long and narrow tube. The left side has an oven attached that is filled with a few grams of potassium and heated to $\sim 70^\circ\text{C}$. This provides a thin potassium background vapour at a pressure of 10^{-7} to 10^{-8} mbar. From the background a 2D-MOT is loaded that creates a beam of pre-cooled atoms. The 2D-MOT is aligned such that the atomic beam travels through the differential pumping stage to the right side of the setup into the science chamber to load a 3D-MOT. The science chamber is realized as a glass cell that features wide optical access, and it is under ultra-high vacuum with a pressure of less than 10^{-11} mbar. The low pressure ensures low heating rates of the atomic cloud and allows for the preparation of ultra-cold atomic samples.



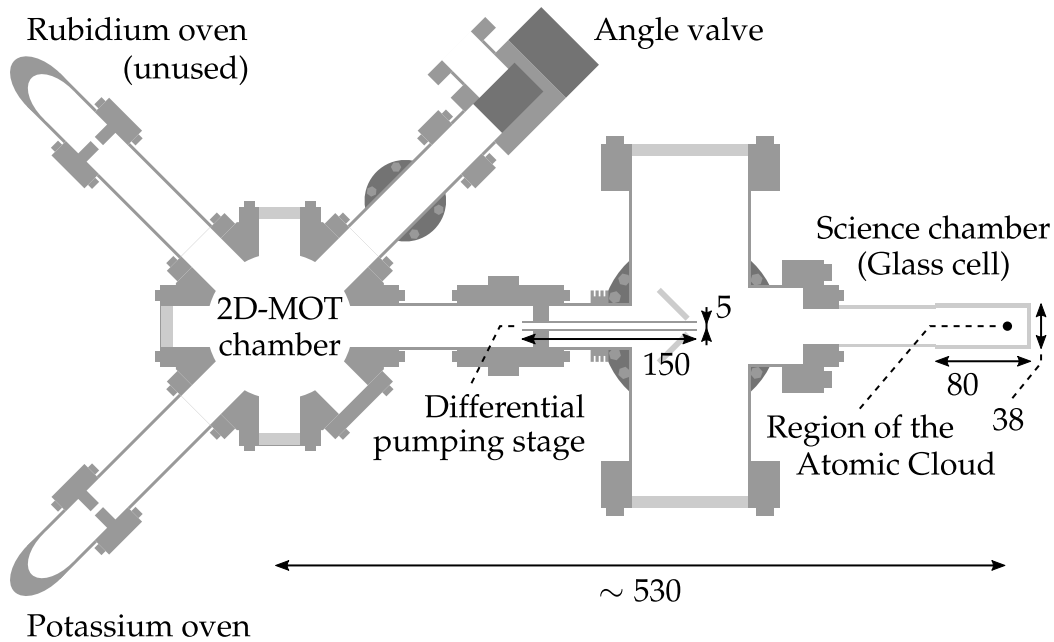


Figure 3.1: Vacuum system of the experiment. A cut through the system is shown, viewing the vacuum setup from the top. The system is divided in two regions by a differential pumping stage, which is implemented by a long tube. The left region with the 2D-MOT chamber has a relatively high pressure (10^{-7} to 10^{-8} mbar) since heating the potassium oven provides a thin background gas. The right part of the setup has ultra-high vacuum which is below 10^{-11} mbar. The experiments are performed in the science chamber, which is a rectangular glass cell. It allows components to be installed close to the atomic cloud and has good optical access. All dimensions are given in millimetres.

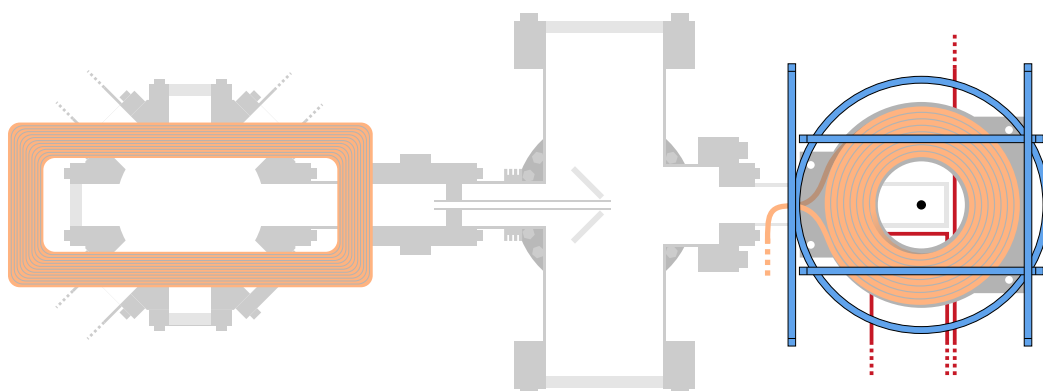


Figure 3.2: Setup of the magnetic coils. The vacuum system and magnetic coils are depicted as seen from the top. On the left side, a set of elongated coils is placed below and above the 2D-MOT chamber to provide a quadrupole field for the 2D-MOT. On the right side, the two main coils (orange) are placed below and above the glass cell, and they can provide a quadrupole or a homogeneous field. In addition, a gradient in gravity direction can be applied. To shift the centre of the magnetic field and to cancel residual offsets and gradients, three sets of offset coils (blue) and two single gradient wires close to the science chamber (red) are included.

3.2 Magnetic Field Setup

Different setups of magnetic coils are utilized to provide the magnetic field for the experiment. This section gives an overview of the different setups and discusses the main coils in more detail. The schematics of the driver circuits that control the current in the main coils are presented in appendix C.

Figure 3.2 gives a top view of the experimental setup with the different coils. On the left a set of elongated coils is mounted below and above the 2D-MOT chamber. They provide a constant quadrupole field of about 14 G/cm for the 2D-MOT. The coils are kept at constant current throughout the experimental cycle, which reduces complexity, and as the coils are placed rather far from the science chamber their influence is small and the residual magnetic field can be compensated.

Around the science chamber on the right in fig. 3.2 three different coil systems are installed. The main system is a set of two water-cooled coils, one coil above the science chamber and one coil below (details in [60]). These coils are very versatile and provide different magnetic field configurations. The direction of the current in the upper coil can be reversed, and the current



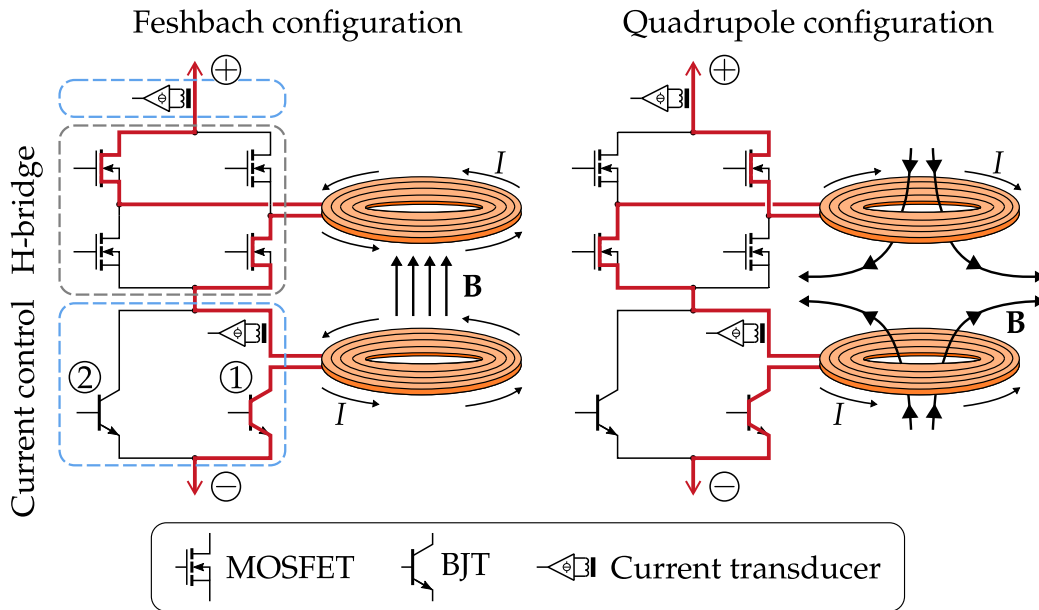


Figure 3.3: Wiring diagram of the main magnetic field coils. The current in the main coils is controlled with field effect transistors (MOSFET) arranged in an H-bridge and bipolar transistors (BJT) arranged in two passbanks to achieve different configurations of the magnetic field. Switching the direction of the current in the upper coil allows creating a homogeneous magnetic background field for Feshbach tuning of the interaction strength (left side) or a quadrupole field for the MOT (right side) with only one set of coils (current flow indicated in red). The total current in the coils is controlled by passbank 1, which regulates on half of the sum of the two current transducers. Passbank 2 acts as a shunt for the lower coil and is regulated on the difference of the transducers. A lower current in the lower coil leads to a gradient of the magnetic field and allows to levitate the atomic cloud. Adapted from [35].

in the lower coil can be smaller than in the upper coil. Thus, the coils can produce the magnetic quadrupole field for the MOT and the magnetic trap, as well as the homogeneous field necessary for Feshbach tuning. Reducing the current in the lower coil in the homogeneous field configuration creates an additional gradient in gravity direction. Choosing the proper gradient the gravitational force can be compensated and the atomic cloud is levitated magnetically.

Besides the two main coils there are three sets of offset coils that allow to apply a homogeneous magnetic field in the three spatial directions, and two

wires that are set up close to the glass cell. When the main coils are switched off the offset coils are used to cancel residual background fields in order to achieve a vanishing magnetic field in the region of the atomic cloud. In the quadrupole configuration, the offset coils are used to shift the zero-point of the magnetic field. The two wires apply a gradient field which is used to cancel residual gradients in the horizontal plane.

The electrical wiring of the main magnetic coils is depicted in [fig. 3.3](#). The two sketches show the current flow through the H-bridge and main coils. The Feshbach configuration for a homogeneous field is depicted on the left side, and the quadrupole configuration on the right side, where the direction of the current in the upper coil is reversed. The currents are measured with two current transducers, where the upper one measures the total current and the lower one the current in the lower coil. The currents are regulated with two passbanks (details on passbank in [\[60\]](#)). The total current through the coils is controlled with passbank 1, which is regulated on half of the sum of both current transducers. Passbank 2 reduces the current in the lower coil and is regulated on the difference between the two current transducers. Details on the driver circuits are presented in [appendix C](#).

To allow for fast changes of the driving current, special precautions have to be taken. The coils are equipped with TVS diodes that break down at a high voltage U_{TVS} , which is tolerable for the electric system, and thus enable a fast dissipation of the energy stored in the magnetic field. However, the field effect transistors (MOSFET) of the H-bridge have a parasitic body diode which conducts if the electrical potential at the source is higher than the potential at the drain. This can lead to a slow decay of the magnetic field as the energy is dissipated by the body diode at a small voltage. We avoided this condition by proper switching of the H-bridge, which is explained in [fig. 3.4](#).

We calibrate the homogeneous field with microwave spectroscopy on the transition between the states $|g_3\rangle$ and $|g_6\rangle$, and the error of the calibration is estimated to be on the order of 0.2 G. Details on the procedure can be found in [\[35\]](#). For Feshbach tuning the main uncertainty is the position of the resonance, which is given with an error of 1.5 G [\[17\]](#). At the typical field strength of about 550 G the homogeneous field has a residual quadratic contribution from the magnetic coils, which can not be suppressed with the offset coils and gradient wires. The quadratic contribution can be approximated by a harmonic trap in the horizontal plane with a frequency of $f = 5.5$ Hz and can be neglected for the experiments presented in this thesis.



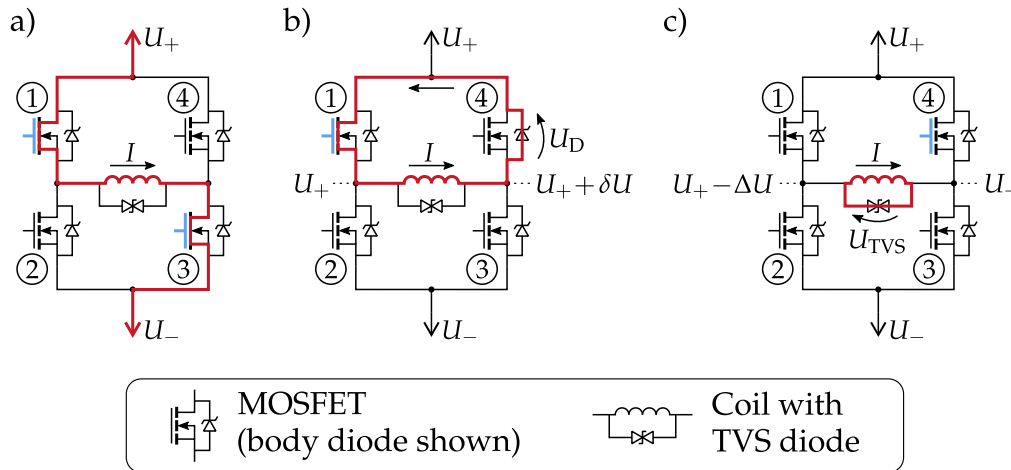


Figure 3.4: Current switching with the H-bridge. Part a) shows the current flow through the upper coil for a homogeneous field, with MOSFETs 1 and 3 conducting (indicated by the blue base), and the current I is indicated in red. When the current is reduced fast, for example by toggling the state of MOSFET 3 and thus breaking the electrical connection (part b), the energy stored in the magnetic field maintains the current. As the left side of the coil is still connected to U_+ its potential is fixed. Due to the current flow the potential on the right side of the coil has to rise. The potential $U_+ + \delta U$ at the source of MOSFET 4 becomes higher than the potential U_+ at its drain, and if the difference is high enough the body diode of the MOSFET conducts. The energy stored in the coil is dissipated by the small voltage drop U_D over the body diode, which takes rather long. To shorten the switching time, the energy has to be dissipated with a higher voltage drop. This can be achieved by toggling the state of MOSFET 1 and 4 in addition to MOSFET 3 (part c). The potential on the right of the coil is thus fixed to U_+ , and the potential left of the coil drops to $U_+ - \Delta U$ due to the current flow. Since the potential at the source of MOSFET 1 is kept lower than the potential at its drain, it maintains isolation. The potential drops until the TVS diode breaks down and dissipates the energy. With the large voltage drop U_{TVS} a fast switching time can be achieved, and this scheme is implemented in the control electronics of the H-bridge (cf. [section C.1](#))

3.3 Laser Systems

The preparation of well stabilized laser light with the right frequencies and powers is a further key ingredient to prepare ultra-cold samples. The laser setup consists of two systems, one providing resonant light for radiative cooling and trapping, the other for imaging of the atomic cloud. The imaging system is described more closely in [section 4.5](#). Two additional systems generate far red-detuned and far blue-detuned light, respectively, which is used for the dipole traps. A detailed description of the systems with technical drawings of the optical setup is given in [\[35\]](#).

Resonant light is provided on the D2 and the D1 transitions by a system which is split in three modules as depicted in [fig. 3.5](#). These modules are connected by optical fibres, which keeps the setup flexible and allows for easy maintenance. The first module includes two external cavity diode lasers which are stabilized using doppler-free absorption spectroscopy [\[67\]](#). We modulate the magnetic field at the spectroscopy cell to shift the resonance, generate the error signal with a lock-in amplifier and lock the frequency using a PI controller. The D2 light is locked onto the cross-over resonance of the ground states, and the D1 light blue-detuned to this resonance which simplifies the generation of light for the grey molasses. Both lights are amplified by home-built fibre-coupled tapered amplifiers (TA) [\[68, 28\]](#).

Subsequently, the frequency of the light is shifted with acousto-optic modulators (AOM) [\[69\]](#) in a double-pass cat-eye configuration [\[70\]](#). The AOMs shift the light frequency from the crossover of the ground states to the red to reach the resonance of the cooler transition and to the blue to reach the repumper transition. The 2D-MOT, which acts as source for pre-cooled atoms, gets D2 cooling and repumping light which is overlapped with a 50/50 beam splitter in an optical fibre. Both frequencies are amplified in one TA [\[28\]](#) leaving us with 350 mW after the optical fibre at the experiment. The 2D-MOT needs a separate push beam that contains about 7 mW D2 cooling light. For the MOT we need D2 cooling and repumping light, and for the grey molasses D1 cooling and repumping light. As MOT and grey molasses are prepared after each other in the science cell and need the same polarizations, all four frequencies are coupled into one optical fibre to be delivered to the experimental setup. This is achieved by 50/50 beam splitters for cooling and repumping lights and by a bandpass filter for D2 and D1 light as the frequencies are sufficiently far apart. At the experiment we usually get for the individual frequencies a



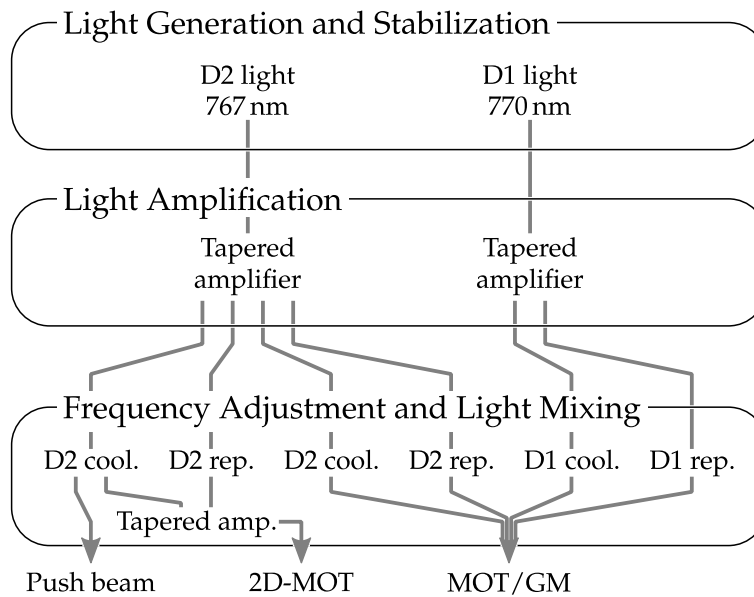


Figure 3.5: Preparation of resonant light. The two laser systems for D2 and D1 light are divided in three modules that are connected via optical fibres to simplify maintenance and make the system more flexible. In the first step two lasers provide light for the D2 and D1 transition of potassium, and they are frequency stabilized to the crossover of the respective ground states. Next, the light is amplified with TAs. In the final step the frequencies are shifted with AOMs to match the cooling and repumping transitions. The 2D-MOT needs only D2 light, and the cooler and repumper frequencies are combined in a fibre and subsequently amplified. The atom source is completed with a push beam that contains only D2 cooling light. For the MOT setup all four frequencies are combined in one optical fibre as the D1 light is needed in the same place for the grey molasses (GM).

power of 30 mW (D2 C), 20 mW (D2 R), 25 mW (D1 C) and 8 mW (D1 R).

For the D2 light the frequency and amplitude of the rf signal for the AOMs can be set by the experiment control system using custom AOM drivers. The preparation of the D1 light needs special attention as the Raman condition has to be met precisely. This means when changing the frequency of the AOM for the D1 cooling light the frequency for the repumping light has to follow accordingly. We achieve exact matching by deriving the rf signal for the repumping light from the rf signal of the cooling light by subtracting a fixed rf offset from a stable source [62].

Far-detuned light for the dipole traps is provided by high-power lasers, one for red-detuned light with a wavelength of 1064 nm and one for blue-detuned light at 532 nm. The light for the different dipole traps is derived using a flight of half-wave plates and polarizing beam splitters. Subsequently, each beam passes an AOM in single-pass configuration to regulate the power and shift its frequency in order to avoid interference with other beams. For each beam the zeroth order is blocked, and we guide the first order to the experimental setup. The individual laser beams are power-stabilized, and the control electronics is shown in [fig. 3.6](#). We found adding an attenuator and amplifier to be crucial to keep a constant load on the voltage controlled oscillator. We thus avoid small drifts in frequency that would translate in position drifts of the laser beams diffracted by the AOM.

The 1064 nm laser system generates two high power beams for the reservoir dipole trap with 12 W each, which are guided to the experiment with a free-space setup. Further beams with a maximum power of 2 W are provided via optical fibres for attractive dipole traps.

The 532 nm laser system is used for the repulsive traps formed with the pancake lattice setup and the DMD. The systems receive a maximum of 2 W and 1 W of power through liquid crystal fibres, respectively.

3.4 Preparation of the Ultra-cold Sample

To prepare a sample of ultra-cold atoms, all the different components need to be well synchronized to enable proper cooling and trapping. In short, the following steps are executed during a typical experimental run. A beam of pre-cooled atoms is prepared with the 2D-MOT and collected in a MOT in the science chamber. The atomic cloud is compressed, further cooled by grey molasses cooling and loaded in a magnetic trap. The magnetic gradient



section reviews the different experimental stages and their implementation. In the course of this thesis a DMD was implemented to achieve configurable trapping potentials in the lateral direction. An in depth discussion of the implementation of the DMD follows in [section 3.5](#).

3.4.1 Magneto-optical Traps

The magneto-optical traps are implemented using the D2 transition of ^{39}K as discussed in [section 2.5.1](#). The cooling and repumping lights are guided to the setup in a single fibre and then split into two beams per axis by a cascade of half-wave plates and polarizing beam splitters. Subsequently, the beams are guided to their destination in a free-space setup. This non-retroreflecting, non-fiberized setup allows for superb alignment, meticulous power balancing and a high polarization stability.

2D-MOT The atom source of our experimental setup is a 2D-MOT, which is loaded with ^{39}K from the background in the 2D-MOT chamber. It consists of two pairs of counter-propagating MOT beams with an $1/e^2$ -diameter of 15 mm, and a set of elongated coils that provide a quadruple field of about 14 G/cm. This cools the atoms in the plane spanned by the MOT beams and produces a beam of pre-cooled atoms perpendicular to this plane. An additional fifth beam with 2 mm diameter that contains only cooling light is shone onto the atoms towards the differential pumping stage. It plugs one side of the 2D-MOT and accelerates atoms in the direction of the science chamber. We found this beam to be very critical for proper loading of the MOT. Furthermore, we discovered that adding repumping light to the push beam makes loading the MOT significantly worse, most likely due to persisting interactions with the atoms on the way to the science chamber and associated heating.

MOT The beam of pre-cooled atoms is directed through the differential pumping stage and captured in the science cell by a MOT. It utilizes three sets of counter-propagating beams with $1/e^2$ -diameter of 13.5 mm and a quadrupole magnetic field with a gradient of about 7.5 G/cm in the strong axis. The two vertical beams have to pass the objectives located above and below the glass cell, and thus need a correction to be collimated in the atomic region. For the upper objective this is realized with a static telescope. The distances and lenses are presented in [fig. 3.7](#), and a more detailed schematic



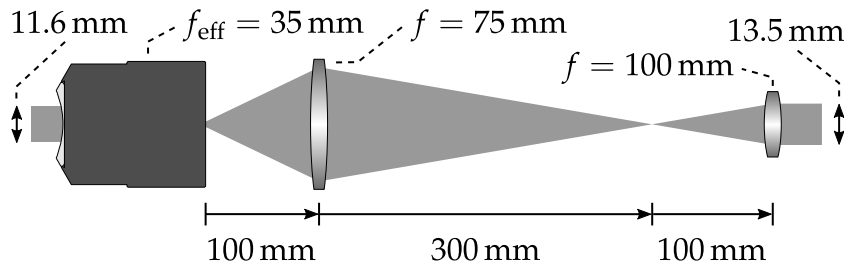


Figure 3.7: Telescope for upper MOT beam. Together with the upper objective and the two lenses a telescope is formed, which retains the collimation of the upper MOT beam and the imaging beam. The lenses are chosen to come as close to a 1:1 telescope as spacial restrictions allow.

of the implementation is shown in [fig. 4.12](#). The lower objective is central for the imaging of the cloud and its path can not be obscured. Thus, a lens with focal length $f = 35$ mm, which forms a 1:1 telescope with the objective, and a mirror are moved in with pneumatic stages during the MOT phase to guide the lower MOT beam. The MOT is loaded for about 3 s.

Compressed MOT To achieve a higher density we compress the atomic cloud at the end of the MOT phase within 5 ms by ramping up the magnetic field and ramping the frequencies further away from resonance, which results in a more compact and colder cloud.

3.4.2 Grey Molasses

A phase of grey molasses cooling follows directly after the compressed MOT. The two ground states are addressed on the D1 transition by laser light in Raman condition. The choice of the D1 transition is typical for ^{39}K as discussed in [section 2.5.2](#). Since the polarization is the same as for the MOT, the D1 light is coupled into the MOT fibre as well and the same optics for preparing the beams can be used. The cooling is initiated by switching off the magnetic field and the D2 light, and switching on the D1 light instead. The grey molasses stage takes 4 ms in total and is split in two parts. We start with high power and frequencies close to resonance to achieve strong cooling forces in the beginning and subsequently ramp the power down and the frequencies away from resonance to achieve a low temperature in the end. The D1 laser system is designed specifically to maintain the Raman condition during this process as discussed in [section 3.3](#). The stage is concluded by

switching off the cooler light for the last 0.2 ms to pump all atoms to the $F = 1$ ground state manifold. With this cooling technique the atomic cloud typically achieves a temperature of 8 μK . After the grey molasses stage the resonant light is switched off and completely blocked by mechanical shutters on the laser preparation table to ensure that the atomic cloud is not disturbed by residual light.

3.4.3 Magnetic Trap

A magnetic trap is employed following the stages of radiative trapping and cooling. It is implemented with a simple quadrupole field (22 G/cm gradient in strong axis) by the main coils, and it traps the low-field seeking substate $m_F = -1$ as discussed in section 2.5.3. After the grey molasses stage all substates are equally populated but the magnetic trap selects atoms in $m_F = -1$. Atoms in the other substates fall out of the trapping region due to gravity and the atomic cloud is left in a pure spin state. Subsequently, the gradient is slowly increased to 56 G/cm (strong axis) in order to compress the atomic cloud which increases the temperature of the atoms to typically 60 μK .

3.4.4 Dipole Traps

For cooling to degeneracy and the subsequent experiments the atoms are held in different dipole traps generated by attractive 1064 nm or repulsive 532 nm light. We start by loading the atoms into the reservoir trap from the magnetic trap by slowly ramping up the laser power and ramping down the quadrupole magnetic field afterwards. Then, we switch the H-bridge and apply a homogeneous background magnetic field on the order of 550 G to tune the interaction to about $175 a_0$ for evaporative cooling. The cooling process is enforced by lowering the depths of the dipole traps. Different traps are used to keep the high density of the atomic cloud and to achieve the two-dimensional geometry in the end. We shortly discuss the different traps, the evaporation strategy and the final preparation of the BEC. More information, especially on the mounting of the traps and the interferometer setup for the pancake trap can be found in [35].

Reservoir Trap To achieve a large trapping volume the attractive reservoir trap consists of two far red-detuned beams crossed under an angle of 10° in the horizontal plane. The beams have a waist of 50 μm and reach a power of up to 12 W each.



Condensor, Kompressor and Pancake Trap We use two more attractive traps with tighter focus, called the condensor and kompressor. They have a circular waist of $35\ \mu\text{m}$ and an elliptical waist of $17\ \mu\text{m}/51\ \mu\text{m}$, respectively. The waist of the kompressor beam is flattened in gravity direction to load a single lattice site. The beams are crossed under an angle of 10° in the vertical plane and the kompressor is aligned perpendicular to gravity. Each beam carries up to 2W of power. Furthermore, a repulsive lattice, called pancake trap, provides trapping in gravity direction. It is formed with an interferometer setup, the distance between the repulsive sheets is $5\ \mu\text{m}$ and the trapping frequency in gravity direction is 1.5 kHz. For increased stability the three traps discussed in this paragraph are mounted on a massive aluminium wedge, which ensures common motion.

Evaporation The process of evaporation consists of three stages. We start with the atomic cloud being held in the reservoir trap and the condensor, which cross under an angle of about 90° . The reservoir trap is ramped down by 90% while the intensity of the condensor is kept constant. Next, the reservoir traps are ramped down completely while the condensor is ramped down by 94%. Simultaneously, the kompressor is ramped up to the same intensity as the condensor. The atomic cloud is now held by condensor and kompressor, and a BEC is formed by ramping down the intensity of both beams further.

Final Preparations After the BEC is formed we levitate the atomic cloud magnetically and change the background magnetic field to reduce the interaction strength. The pancake trap is ramped up, and a single site of the pancake lattice is loaded as the kompressor ensures that the atomic cloud is small enough in gravity direction. At this point we ramp down the attractive dipole traps and the atomic cloud is held by the curvature of the homogeneous magnetic field in lateral direction. The interaction strength is reduced further to reduce the space occupied by the atomic cloud in the harmonic trap. Next, we switch on the DMD with a mask that resembles a big quadratic box to capture the atomic cloud. Subsequently, we adiabatically transform the mask to reach the desired potential. The optical setup for the DMD and the quasi one-dimensional trapping is discussed more closely in the next section. The preparation with harmonic trapping in lateral direction is achieved in a slightly different way which is discussed in [35].

3.5 Arbitrary Trapping Potentials in Two Dimensions

The variants of dipole traps are as wide-ranging as the amount of optical elements one can use to sculpt the shape of laser beams. One particularly versatile element is a digital micromirror device (DMD), which consists of a huge amount of small mirrors that can be addressed individually [48]. Typically, they are small squares that can be tilted along their transverse axis by $\pm 12^\circ$ and can thus be configured to reflect incident light into one or the other direction. In the context of dipole traps this can be used to provide configurable trapping potentials in two dimensions [18].

The first part of this section shows our implementation of a DMD in direct imaging configuration. The chip has 2560×1600 mirrors on an area of $19.4 \text{ mm} \times 12.1 \text{ mm}$, and we typically use the central square with size of the short axis. It is illuminated with 532 nm light and the reflection is demagnified by about a factor of 90 onto the atomic plane. Thus, we can manipulate the atoms in a region of about $130 \mu\text{m} \times 130 \mu\text{m}$. More details about the design and first tests of the setup are presented in [63].

Since the single mirrors are demagnified below the resolution of the imaging system they have to be convoluted with the point spread function of the system (cf. section 4.3.1), which leads to averaging over several pixels in the atomic plane. This can be exploited to prepare potentials that are not limited to regions with and without light, but allow for grey scales. We start by preparing masks for the DMD as grey scale images. In general, the surface of the DMD has to be treated as a grating, and the grey scale image has to be scaled with the square-root to account for interference effects. Subsequently, the image is binarized using the Floyd-Steinberg algorithm, which scans over the pixels and locally redistributes any rounding errors to surrounding pixels to get a dithered image. The resulting grey scales in the potential are important to prepare flat density distributions. It allows for the compensation of errors such as the non-uniform illumination of the DMD. Details about the algorithm can be found in [63].

In the second part of this section we discuss the preparation of a quasi one-dimensional BEC with the help of DMD and pancake trap, and characterize the atomic cloud. The preparation procedure sets the foundations for the experiments on physical computing, which are presented in chapter 5.



3.5.1 Implementation of the DMD

The optical setup for the creation of a sculpted light beam with the DMD is placed on a breadboard, which is located above the science cell. A sketch of the setup located on the breadboard is depicted in [fig. 3.8](#). The last parts of the DMD setup are not placed on the breadboard. They include the optics for overlapping of the beam from the DMD with the other vertical beams for MOT and imaging, and these components are shown in [fig. 4.6](#). The objective acts as the last telescope lens, and it is discussed more closely in [section 4.3.1](#).

We start with blue-detuned laser light from the high-power laser (cf. [section 3.3](#)), which is guided to the setup with a photonic crystal fibre providing up to 1 W power of 532 nm light. Its polarization is cleaned with a Glan-Taylor prism and a small part is coupled out onto a photodiode. The signal is fed into a PI controller, which stabilizes the laser power with an AOM setup. Subsequently, the beam is widened to a diameter of about 12 mm with a Galilean telescope to cover the central square of the DMD chip. The chip is mounted such that the tilt axis of the mirrors is aligned in gravity direction and the direction of the outgoing beam is perpendicular to the mounting plane of the individual mirrors. This ensures that all mirrors are in the focus of the subsequent imaging system. After being shaped by the mirrors of the DMD, the light is demagnified by a factor of about 90 with two 4f telescope setups. The first demagnifies the image by a factor of 4 and it is used for spatial filtering. This is necessary since the DMD acts as a grating and creates higher diffraction orders. The filtering is realized with an iris in the Fourier plane that blocks all but the central order. Thereafter, the remaining demagnification is achieved with a second 4f telescope. The beam passes a lens with high focal length, and it is then reflected out of the plane in gravity direction. With the help of a dichroic mirror, which is transparent for the imaging and MOT beams (cf. [fig. 4.6](#)), the DMD light is guided into the vertical optical axis of the experiment. The second element of the telescope is the upper objective. It completes the setup and projects the DMD image into the atomic plane. To focus the DMD light with the upper objective we re-imaged the projection of the DMD with the ProEM imaging setup. By removing the filters in front of the camera the green light can be observed directly.

Our first results are depicted in [fig. 3.9](#). They show single realizations of the atomic cloud in the form of the logo of our institute and our experiment. The cloud is not condensed since the pictures were obtained shortly after building in the setup and no proper loading strategy was applied at the time. However, they show the versatility of the setup and give an intuition of the

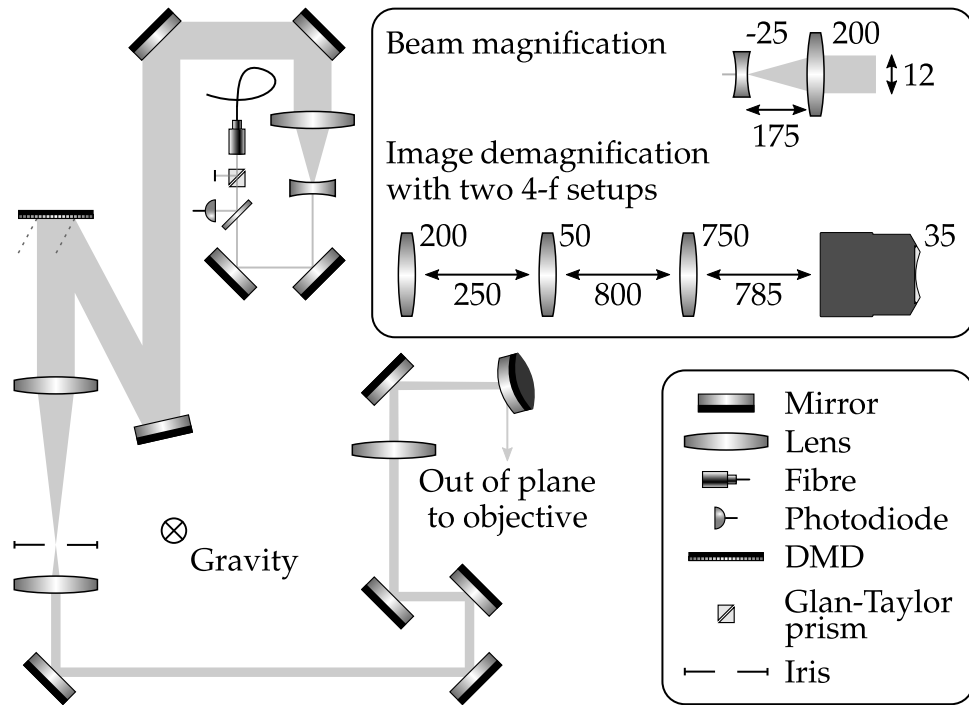


Figure 3.8: Optical setup for imprinting potentials with the DMD. The setup for the generation of the spatially modulated light with the DMD is located on a bread board above the glass cell. The 532 nm light is guided to the setup with an optical crystal fibre, its polarization is cleaned with a Glan-Taylor prism, and a small amount of light is coupled out onto a photodiode to stabilize the intensity with a PI controller. The beam is then magnified with a Galilean telescope to cover the DMD, where it is shaped by the mirrors. When being in the off-position, the light is reflected out of the beam path (dashed line). For mirrors in the on-position the light travels further towards the atoms, and the the light beam is shaped by these mirrors. In the sketch we only indicate the outer shape of the beam with the grey area. The shaped beam is demagnified by about a factor of 90 with two 4f telescopes, as indicated in the upper right. The first setup demagnifies the image by a factor of 4 and contains an iris at the focus to block all but the central mode. The second telescope is rather long. It uses the objective as second lens to demagnify the image onto the atomic plane, which is not depicted in the figure. Note that the last mirror, which is shown in the sketch, reflects the beam out of the plane downwards to the science cell. The beam is then guided onto the atoms with a mirror and a dichroic mirror, as depicted in fig. 4.6. All measurements are in millimetres.



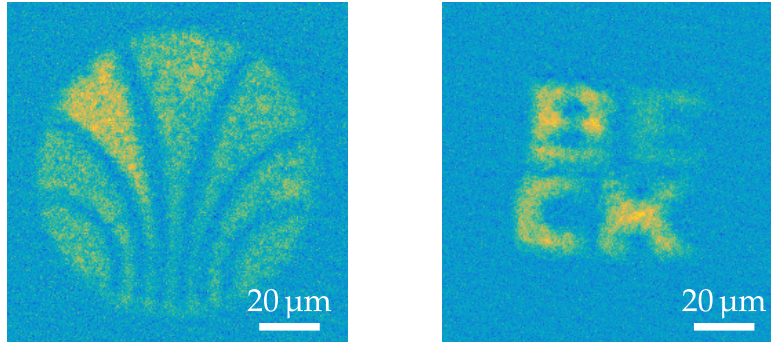


Figure 3.9: Atomic cloud in complex trapping potentials. The images show single realizations of our atomic cloud in the form of the logo of our institute (left) and the experiment (right). Note that the atomic cloud is not condensed as the images were taken just after building in the setup without thorough optimization of the loading strategy. Blue corresponds to no atomic signal.

structures that can be imprinted onto the atomic cloud.

To calibrate the DMD setup we project a disk onto the atomic cloud as shown on in the left panel of [fig. 3.10](#). It has a diameter of 1100 pix, and a distinctive pattern is formed by local maxima of the intensity. The features allow both rotation and magnification to be identified. The right panel shows an average over 100 experimental realizations of the atomic cloud. As before, it is not condensed and the imaging is not yet perfectly aligned. We find that the atomic cloud has a diameter of about $95\ \mu\text{m}$ and extract a rotation angle of 42° from the position of the holes. The total demagnification from the DMD chip is extracted to be 89, which means that one pixel has a side length of about $0.09\ \mu\text{m}$ in the atomic plane. This is well beyond the resolution of the objective and its point spread function averages over roughly 7 neighbouring mirrors (cp. [section 4.3.1](#)), thus allowing for grey scale images as discussed above.

3.5.2 Preparation and Characterization of the Quasi One-dimensional BEC

Once the BEC is created as discussed in [section 3.4](#) we can transform its shape in two dimensions with the DMD. We start with a big square mask to capture as many atoms as possible and slowly reduce its size. The sequence is shown as a flip book in the bottom left corner, starting at page 14. Every fourth image is shown, and black pixels correspond to mirrors in the on-position. The

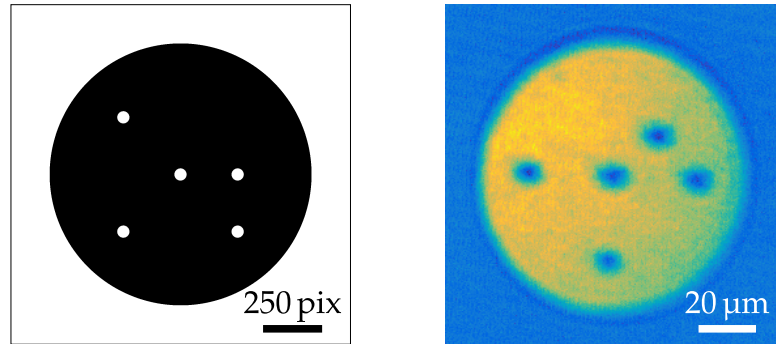


Figure 3.10: Calibration of the DMD. The left image shows a cut-out of the DMD mask which imaged into the atomic plane. In the black region mirrors are turned off (no light) and in the white region light is present. The resulting density distribution is depicted in the right image, which is an average over 100 experimental realizations (blue corresponds to no atomic signal). As before, the cloud is not in a condensed state. By mapping the holes onto each other we find that the image of the DMD is rotated by 42° which results from the mounting of DMD with respect to the atomic plane, and it is demagnified by a factor of 89. The size of a single pixel corresponds to about $0.09 \mu\text{m}$ in the atomic plane, well beyond the resolution of our objective. Thus, multiple pixels are averaged by the point spread function which allows for the generation of grey scales.

final mask for the elongated rectangular box trap is depicted in [fig. 3.11 b](#)). It results from binarizing the image shown in panel a) with the Floyd-Steinberg algorithm. This image is derived from a homogeneous box with the inner size of $1000 \text{ pix} \times 40 \text{ pix}$ and a border of 40 pix width, which corresponds to a box of $87.5 \mu\text{m} \times 3.5 \mu\text{m}$ in the atomic plane. We multiply correction factors necessary for flatness (details in paragraph below) and scale the image to a maximal value of $1/3$. This allows a background potential to be applied to the atomic cloud while scaling the height of the box walls accordingly (cf. [section 5.2](#)). Panel c) shows a mean image of the resulting condensate.

Correction Factors To achieve a flat density distribution the intensity of the box walls has to be similar along the trap. Due to the finite resolution of the optical system that projects the mask in the atomic plane the walls are broadened and extend towards the atoms. An inhomogeneous intensity can thus lead to locally varying trapping potentials. To account for the inhomogeneous illumination of the DMD with a Gaussian beam we take an image



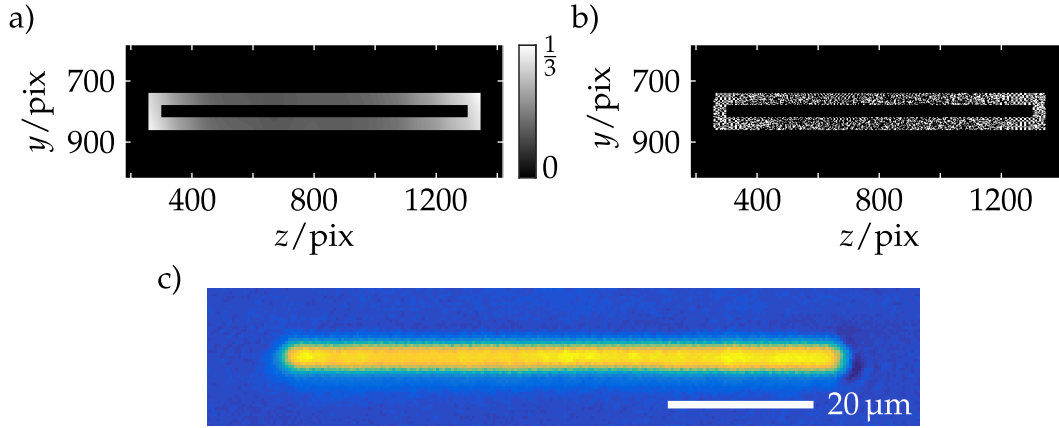


Figure 3.11: DMD mask for the elongated box trap and quasi one-dimensional condensate. We start with a uniform box and scale it by correction factors to cancel the uneven illumination of the DMD chip and other errors. The result is presented in part a), and the image is scaled to a value of $1/3$ at maximum to allow for potential shifts as performed in section 5.2. Subsequently, the image is binarized with the Floyd-Steinberg algorithm to produce a mask for the DMD, and it is depicted in part b). Panel c) shows the resulting density distribution averaged over 50 realizations.

of the DMD with all mirrors in on-position with the ProEM imaging system (filters removed) and record the intensity distribution. A two-dimensional Gaussian function is fitted to this distribution (see fig. 3.12 a). When designing a mask for the DMD this correction is divided out to level the light intensity. The effect on the mask can be seen directly by comparing the wall height in fig. 3.11 a) to the shaded area in fig. 3.12 a), which is the position of the box trap on the DMD chip. To achieve a flat density distribution further corrections are necessary. We prepare a condensate with the mask, sum its density distribution along the short axis and quantify deviations to a flat distribution. The resulting deviations are smoothed with a Gaussian filter and multiplied to the long axis of the mask as a correction factor. We repeat the procedure and find sufficient convergence after two iterations. The resulting correction factor is displayed in fig. 3.12 b) and leaves us with the approximately flat distribution depicted in fig. 3.11 c).

Characterization The atomic cloud has a length of $l_{\text{BEC}} = 85 \mu\text{m}$, and we estimate the chemical potential μ in the following. Imprinting a phase on

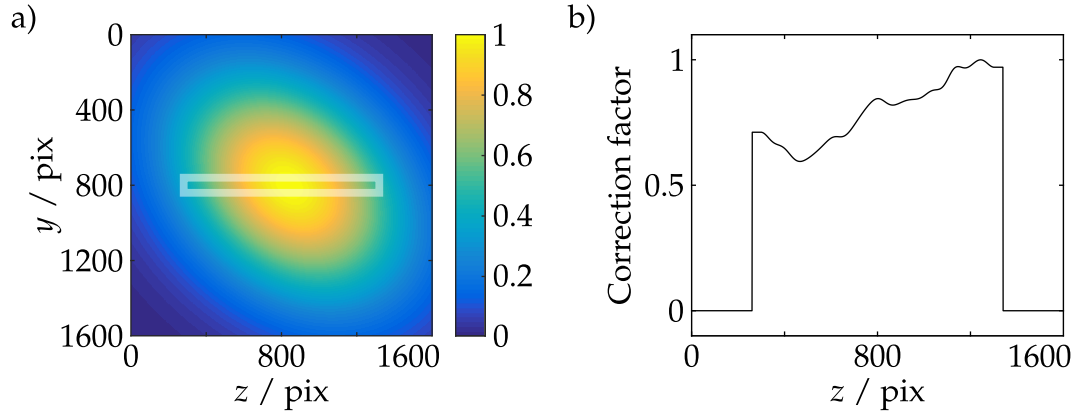


Figure 3.12: Correction factors for DMD masks. To receive a flat density distribution the walls of the box trap need to have a constant intensity along the atomic cloud. Part a) shows the correction factor for the uneven illumination of the DMD. We measure the intensity reflected by the DMD with all mirrors in on-position with the ProEM imaging system (filters removed) and fit a two-dimensional Gaussian to the distribution (scaled to one). This correction is divided out when designing a mask on the DMD to receive equal intensity over the mask. The resulting grey scale image is subsequently scaled to one to get the maximal intensity. The shaded area shows the mask for the elongated box trap. Part b) depicts an additional correction factor which is multiplied to the long axis of the mask. The factor is necessary to achieve a flat atomic distribution, and it is calculated in two iterations from comparing images of the atomic cloud to a uniform distribution.

a part of the atomic cloud produces over- and under-densities that travel along the cloud. The procedure for the phase imprint is explained in detail in [section 5.2](#), and the resulting density distribution and its time evolution are depicted in [fig. 5.5](#). Since small perturbations on the atomic cloud travel with the speed of sound c_s we can extract this quantity by tracking the movement of the density peak. We measure the travel distance with evolution time for different positions of the imprinted phase jump. The results are depicted in [fig. 3.13](#). A linear fit yields the speed of sound,

$$c_s = 3.5 \mu\text{m/ms} , \quad (3.1)$$

and following [eq. \(2.17\)](#) we can directly derive the chemical potential

$$\mu = mc_s^2 = 1.2 \text{ kHz} . \quad (3.2)$$



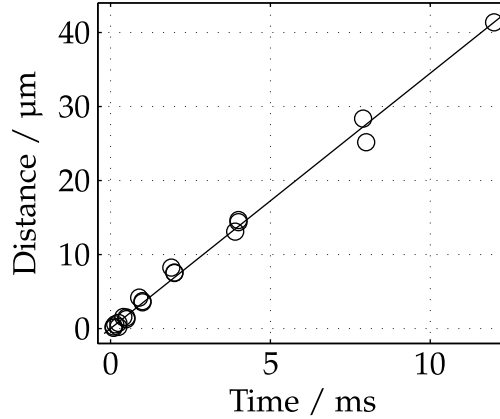


Figure 3.13: Estimation of the speed of sound. We track the movement of the over-density in the density profile after imprinting a phase on the atomic cloud. The procedure is discussed in [section 5.2](#) and a typical evolution is depicted in [fig. 5.5](#). We extract the distance that the over-density travels in a specific time. The speed of sound is given by the slope of a linear fit which yields $c_s = 3.45 \mu\text{m}/\text{ms}$.

Comparing the chemical potential to the trap frequency allows us to judge how far the system is in a one-dimensional regime. In gravity direction the trap is provided by the pancake lattice, and its trap frequency of 1.5 kHz is higher than the chemical potential. The first excited oscillator mode is at a frequency of $3/2 \times 1.5 \text{ kHz} = 2.3 \text{ kHz}$ which is twice the chemical potential. Thus, the trap should suppress higher oscillator modes in gravity direction. To evaluate the confinement in the short direction of the trap in plane we sum the image [fig. 3.11 c](#)) along the long axis. For the short axis we find a width of about $6 \mu\text{m}$, which can be compared to the healing length of the system (cf. [eq. \(2.13\)](#)). With the chemical potential estimated above we get a healing length of $\zeta = 3.3 \mu\text{m}$, which is about half the system's width and suggests that the system is well confined in this direction. Moreover, the experiments performed in the elongated box trap take place predominantly in the limit of low spatial frequency, and we did not observe excitations in the short direction. We thus treat the atomic cloud as quasi one-dimensional.

Finally, we calibrate the dipole potential caused by the light of the DMD to the chemical potential. After loading the atomic cloud in the elongated box trap we slowly ramp up a local potential which has the form of a Gaussian in the long direction and is constant in the short direction of the trap. [Figure 3.14 a](#)) shows the resulting normalized density distributions for different relative

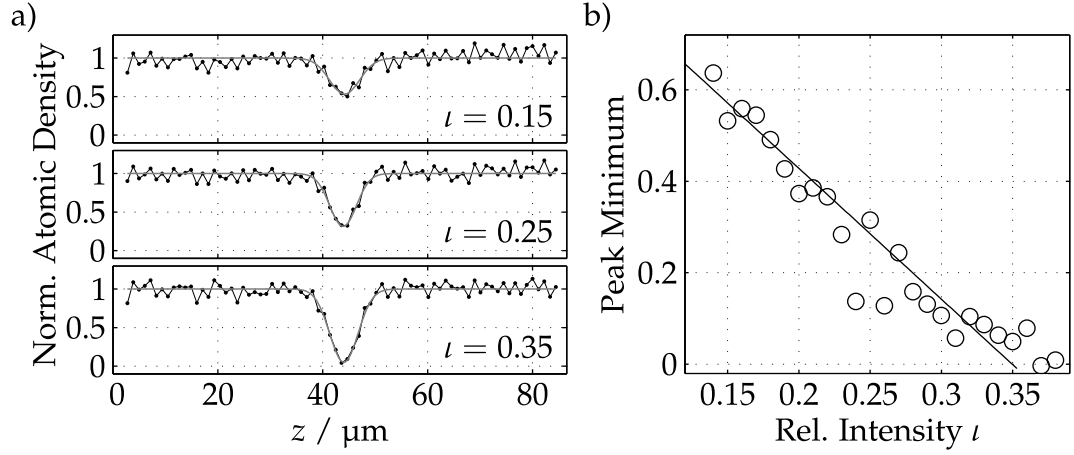


Figure 3.14: Calibration of the DMD potential. In the middle of the otherwise dark background of the elongated box trap we adiabatically ramp up a Gaussian of relative intensity ι . Panel a) shows single shots of the resulting normalized density profiles with the corresponding dip. We fit a Gaussian to the dip and extract the value of the minimum. The results are depicted in panel b) and the expected linear behaviour between the potential and the relative light intensity can be observed. We fit a linear function which is fixed to one for $\iota = 0$. At a value of $\iota_0 = 0.35$ the peak displaces all the atoms and dipole potential of the light thus equals the chemical potential.

intensities ι (height of the peak relative to the height of the box wall). Increasing ι successively, the atomic cloud is eventually displaced completely. We fit a Gaussian to the dip and extract the depth of the minimum, which is plotted in part b) against the relative intensity ι . A linear fit yields a value of $\iota_0 = 0.35$ for full displacement of the atomic cloud. The DMD was illuminated with a laser power of $P_{\text{DMD}} = 0.2 \text{ W}$ for the measurement, and we estimate the calibration factor to be

$$c_L = \mu / (\iota_0 P_{\text{DMD}}) = 17 \text{ kHz/W} . \quad (3.3)$$

With this factor we can calculate the height of the box walls, which is 3.4 kHz. Note that the potential of the light might be slightly over-estimated since the displacement of the atoms by the Gaussian slightly increases the chemical potential of the atomic cloud. We assume the calibration to be valid along the whole cloud as the correction factors ensure a flat density distribution, which should correspond to similar light intensities in the atomic plane.



Absorption Imaging at High Magnetic Field

Working with a dilute cloud of ultra-cold atoms inside a vacuum chamber makes direct measurements challenging. Two widely used techniques to extract the density distribution of the atoms are fluorescence and absorption imaging [51]. For fluorescence imaging, resonant light is applied to and absorbed by the atoms, and one measures a portion of the photons that are re-emitted by the atom in random directions with a camera. We use this technique mainly for monitoring the MOT, but also investigated possibilities for imaging in the regime of few atoms [71]. For absorption imaging, the beam of resonant light is imaged onto the camera after hitting the atomic sample. By comparing this perturbed beam with a reference beam without atomic signal, the density profile of the cloud can be extracted. For our experiments we commonly use absorption imaging, and its application and implementation in our setup is the main topic of this chapter.

The first part discusses the requirements for proper imaging of the atomic sample, in particular the need for closed cycle transitions. An absorption imaging scheme is presented that realizes such an approximately closed imaging cycle at high magnetic field using two atomic transitions. Recently, this scheme has been developed for fluorescence imaging [72]. In this thesis we show that it can be adapted to absorption imaging of dense atomic clouds. We investigate its efficiency by varying the intensity ratio of the two transitions, and show that it can be reduced to an effective two-level system for calibration.

Furthermore, the imaging setup of the experiment is introduced. It consists of different imaging systems to take pictures at various stages of the experiment. The main system (*ProEM imaging*) features an objective with a high numerical aperture and allows taking detailed images of our quasi two-dimensional BEC. The mechanical setup is described, the objective is benchmarked and an overview of the alignment procedure is given. The second high-resolution imaging setup (*Pixis imaging*) is discussed and the design of its home-built objective is shown. Finally, the laser system for the imaging setup is presented.

The setup and results discussed in this section build on the works of our bachelor students that helped to investigate the effects of the multilevel structure on the imaging processes [73, 74] and to set up the laser lock system for imaging [75]. An overview of the setup and the laser system is also given in [35], and the results on absorption imaging are published in [76].

4.1 Closing the Optical Cycle

To extract the in-situ density profile of the atomic cloud after the experiment run with a high resolution, as many photons as possible should be scattered in a short time and the measurement should take place immediately. Thus, an imaging scheme that features a closed optical cycle is desirable to avoid losses into dark states that can not be addressed by the imaging light. First, we shortly introduce our imaging scheme for vanishing magnetic field and then discuss imaging at a high field. The experiments presented in this part are performed with a three-dimensional cloud, and we use the ProEM system for imaging (details in section 4.3). Parts of this section are taken or adapted from our publication of the imaging scheme [76].

The atomic levels at vanishing magnetic field are given in fig. 2.1. In this limit the energy eigenstates of the system are pure in the quantum numbers F, m_F , and states that only differ in the magnetic quantum number m_F are energetically degenerate. When imaging the atomic sample in the $|F, m_F\rangle = |1, -1\rangle$ ground state on the D2 transition, atoms can also decay to the $F = 2$ ground state. We thus use both D2 lights with equal intensity to address both ground states. This creates a closed cycling scheme at vanishing magnetic field, as atoms from both ground states can be excited and scatter photons.

For non-vanishing magnetic field the degeneracy of the magnetic sub-states is lifted. In the limit of very high magnetic field the states of both the ground and excited state manifold are pure in the quantum numbers m_J, m_I .



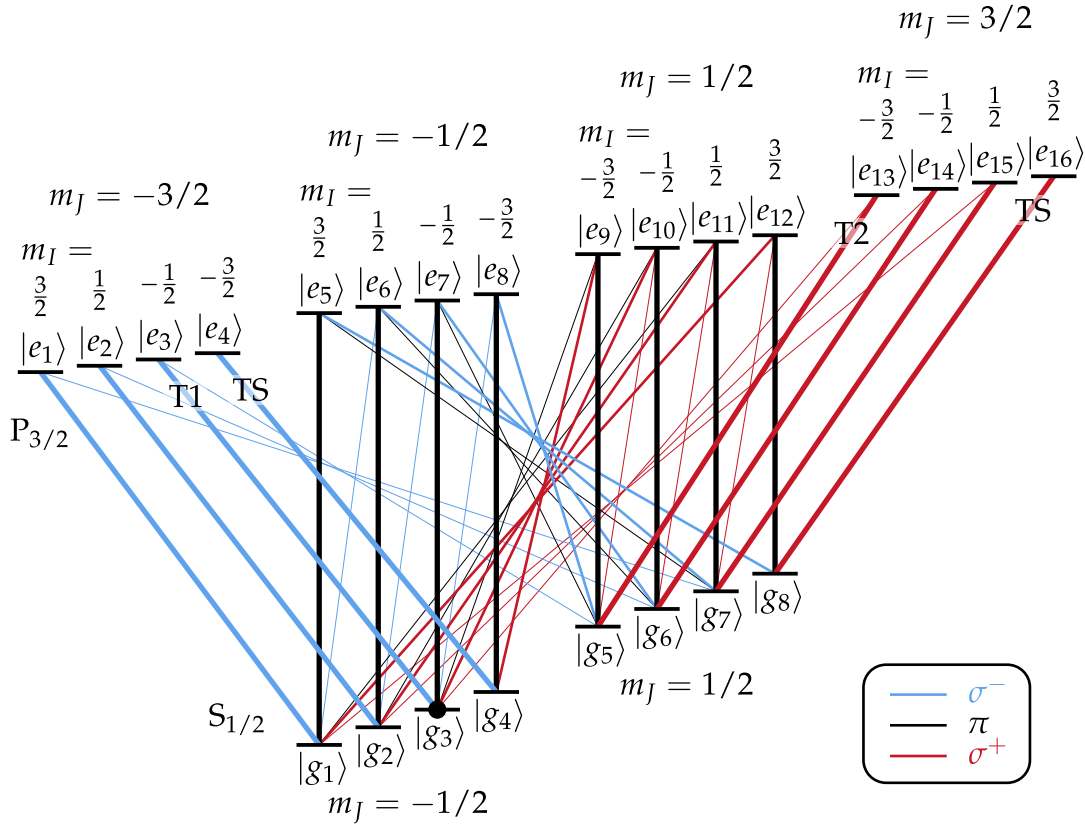


Figure 4.1: Dipole transitions of the D_2 line at 550 G. The energy eigenstates $|g\rangle$ and $|e\rangle$ are depicted for the ground state $S_{1/2}$ and the excited state $P_{3/2}$ hyperfine manifold, respectively, and the atoms are initially prepared in the state $|g_3\rangle$ indicated with the black dot. For the ground states the quantum number m_J of the predominant admixture is given, and the excited states can be described by a single m_J, m_I up to 10^{-4} . The transitions between the ground and excited states are indicated by lines, where transitions that stem from the residual admixtures in the excited states are omitted. For each transition the polarization is given by colour and its strength is displayed by the line width. With a single frequency the best results for our ground state $|g_3\rangle$ are obtained with the transition T1. However, the transition is not closed and atoms can decay to the ground state $|g_5\rangle$. Adding a second frequency to drive the transition T2 leads to an approximately closed scheme. Furthermore, the closed transitions between the stretched states (TS) are indicated. Adapted from [74].

Therefore, a closed cycling transition can be easily found for any ground state. However, at a magnetic field of 550 G, which is typical for our experiments, the ground states are still mixed in m_J, m_I . This increases the number of possible transitions, which are shown in [fig. 4.1](#). Our initial state $|g_3\rangle$, which is adiabatically connected to $|F, m_F\rangle = |1, -1\rangle$ at low field, is indicated with the black dot. The figure shows that only the stretched states with maximal or minimal magnetic quantum number feature a closed transition to an excited state (TS). Interestingly, this holds for all magnetic fields as the stretched states are always pure in m_J, m_I due to its unique m_F . This transition is commonly used for caesium experiments, where an efficient pumping scheme to a stretched state exists [[77, 78](#)]. However, such a scheme is not available in general and often the choice of the atomic ground state is fixed, for example when using Feshbach resonances. Ramping down the magnetic field and imaging the atoms at a vanishing field is not possible as it takes too long and several Feshbach resonances have to be crossed, which makes the extraction of a high quality in-situ image of the density distribution impossible. This leaves imaging the atomic cloud at high field as the only option.

4.1.1 Scheme for High Field Imaging

This section introduces a four-level imaging scheme that results in an approximately closed optical cycle at sufficiently high field. To underline its advantages, [fig. 4.2 a\)](#) compares the absorption signal for imaging at a magnetic field of 550 G when using a single transition (red points) to the improved scheme that exploits two transitions (blue points). Note that in the latter case both imaging lights are overlapped at a polarizing beam splitter and both fall on the camera. While the scattering vanishes for a single frequency after few microseconds, a significantly enhanced signal is achieved when imaging on both transitions. The number of scattered photons is estimated by

$$N_{\text{scatt}} = -\mathcal{G}(C_f - C_i), \quad (4.1)$$

with C_f and C_i the number of integrated counts of the images on the camera with and without atoms, respectively. For both images the CCD offset has been subtracted. Moreover, the images are normalized to each other by comparing a region without atomic signal to account for fluctuations in the imaging light intensity. The factor

$$\mathcal{G} = 1.07 \cdot 0.89 / 0.8 / 0.77 \quad (4.2)$$



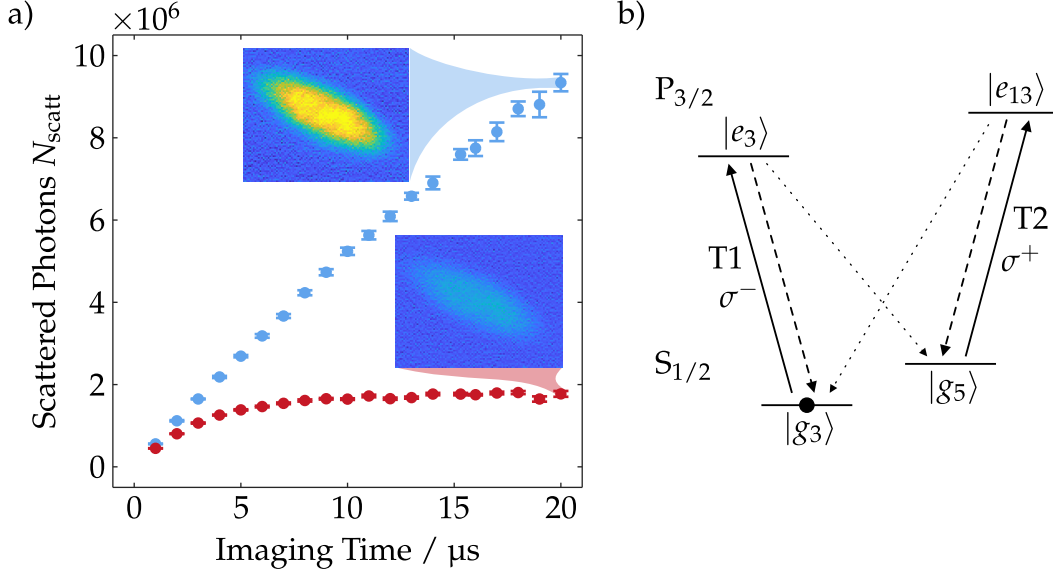


Figure 4.2: Absorption imaging at high field and imaging scheme. Part a) compares the number of scattered photons N_{scatt} when imaging with a single laser frequency (transition T1, red points) to imaging with two frequencies on both transitions T1 and T2 (blue points). Whereas the first levels off within $\sim 5 \mu\text{s}$, a significant enhancement can be observed for the latter. The difference is clearly visible in the absorption images of the atom cloud after $20 \mu\text{s}$ (same colour scale used for both images, dark blue corresponds to no scattered photons). Part b) shows the energy eigenstates relevant for the imaging scheme. Transition T1 excites atoms from the initial state $|g_3\rangle = \sqrt{p}|-1/2, -1/2\rangle + \sqrt{1-p}|1/2, -3/2\rangle$ marked by the black dot to the excited state $|e_3\rangle \simeq |-3/2, -1/2\rangle$. The basis $|m_J, m_I\rangle$ is used here and $p = 0.98$ at a magnetic field of 550 G. While most of the atoms decay back to the initial state (dashed arrow), a small leakage populates the state $|g_5\rangle = \sqrt{p}|1/2, -3/2\rangle + \sqrt{1-p}|-1/2, -1/2\rangle$ (dotted arrow). This state is not addressed by the light resonant with transition T1, leading to the ceasing scattering shown in part a). However, adding a second laser frequency to drive the transition T2 couples the state $|g_5\rangle$ to the excited state $|e_{13}\rangle \simeq |3/2, -3/2\rangle$. As atoms can decay back only into the states $|g_3\rangle$ and $|g_5\rangle$ a closed optical cycle is obtained if the excited states are sufficiently pure in the quantum numbers m_J, m_I . Adapted from [76].

includes from left to right a correction for the solid angle of the objective, the gain and quantum efficiency of the camera, and the reflection loss along the imaging path.

The different results for the absorption signal can be understood from a reduced level scheme, which is displayed in [fig. 4.2 b](#)). Using a single frequency to image the atoms in the initial state $|g_3\rangle \sim |m_J, m_I\rangle = |-1/2, -1/2\rangle$ the best results are obtained by driving the transition T1 with σ_- light to the excited state $|e_3\rangle = |-3/2, -1/2\rangle$. The nearby states (< 15 MHz) are not addressed as m_I is not changed by electric dipole transitions and the energy eigenstates of the upper hyperfine manifold are pure up to 10^{-4} in the m_J, m_I -basis. However, the ground states are mixed in this basis and the two states relevant for the imaging can be written as

$$\begin{aligned} |g_3\rangle &= \sqrt{p} |-1/2, -1/2\rangle + \sqrt{1-p} |1/2, -3/2\rangle, \\ |g_5\rangle &= \sqrt{p} |1/2, -3/2\rangle + \sqrt{1-p} |-1/2, -1/2\rangle, \end{aligned} \quad (4.3)$$

where $p = 0.98$ at 550 G. Hence, the excited state $|e_3\rangle$ can decay back in the initial state $|g_3\rangle$ and the dark state $|g_5\rangle$ as they both have an admixture of the state $|-1/2, -1/2\rangle$. Looking at the dynamics of a single atom, this 2% admixture corresponds to 34 scattering events until it has a probability of 0.5 to be in the dark state $|g_5\rangle$. Assuming a scattering rate of $\Gamma/2$, this corresponds to a timescale of $1.8 \mu\text{s}$, which is consistent with the $2.2 \mu\text{s}$ that can be extracted from the red data points.

To enhance the signal we address the state $|g_5\rangle$ with a second laser frequency. The transition T2 couples the ground state to the excited state $|e_{13}\rangle \simeq |3/2, -3/2\rangle$ with σ_+ light and closes the optical cycle to good approximation as shown in [fig. 4.2 b](#)). The blue data points in part a) confirm that the atoms continue to scatter photons on the relevant timescale. We expect to lose a small fraction of only 2% of the atoms during a typical $10 \mu\text{s}$ imaging pulse. Due to the limited purity of the excited states in the $|m_J, m_I\rangle$ basis they decay into the ground states $|g_2\rangle$ and $|g_6\rangle$, which are not addressed by the imaging light. For typical imaging intensities off-resonant coupling to other excited states is negligible as the closest transitions are detuned by at least 350 MHz.

The imaging procedure discussed here can be generalized to all alkali-like atoms, and it has been successfully used with lithium for fluorescence imaging [72]. The ground states can always be written as a superposition of maximally two $|m_J, m_I\rangle$ states. This is a consequence of the fact that the spin operator F_z commutes with the Hamiltonian as shown in [eq. \(2.3\)](#). Since $J = 1/2$ for



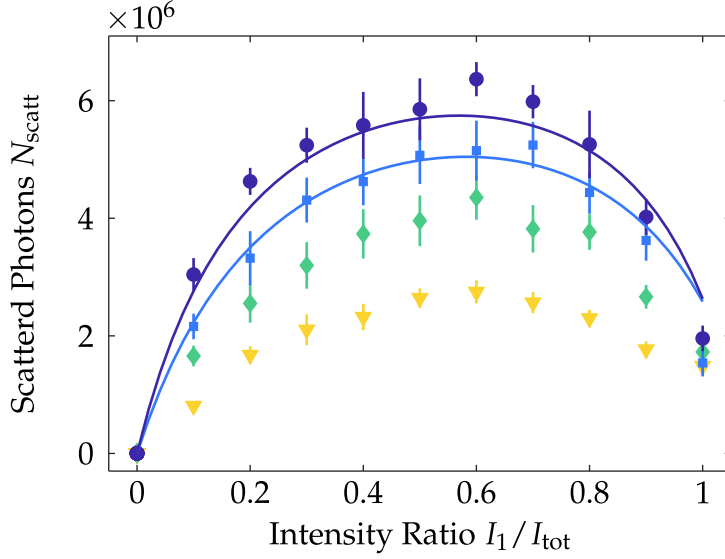


Figure 4.3: Optimization of the intensity ratio. The number of scattered photons is measured at different ratios $r = I_1/I_{\text{tot}}$ and different total intensities $I_{\text{tot}} = I_1 + I_2$. The imaging pulse length is $10 \mu\text{s}$, and the data points correspond to total intensities of $23 \text{ mW}/\text{cm}^2$ (triangles), $42 \text{ mW}/\text{cm}^2$ (diamonds), $60 \text{ mW}/\text{cm}^2$ (squares), and $79 \text{ mW}/\text{cm}^2$ (circles). For the highest intensities the largest signal is found at $r \simeq 0.5$. This optimum slightly shifts to larger ratios for decreasing light intensities, as it takes a longer time to reach the steady state. We compare the data to numerical solutions of the optical Bloch equations for the four-level system, scaled by a global factor (solid curves). Adapted from [76].

the ground states of all alkali atoms (i.e. $m_J = \pm 1/2$) there are maximally two states with the same $m_F = m_J + m_I$. Except for the stretched states with maximal $|m_F|$, all states can be written in the form of Eq. 4.3, and the imaging scheme can be applied.

4.1.2 Optimal Intensity Ratio and Calibration

In this section we investigate the optimal intensity ratio of the two frequencies for the imaging scheme and showcase the calibration for a three-dimensional trap geometry with different intensity ratios. When imaging with high intensities, this calibration is important to obtain a linear measure for the density, as the atomic system is saturable and thus responds in a non-linear

fashion.

We measure the number of scattered photons N_{scatt} (as in eq. (4.1)) during a $10 \mu\text{s}$ imaging pulse for different ratios $r = I_1/I_{\text{tot}}$. The intensities of the two imaging transitions T1 and T2 are I_1 and I_2 , respectively, and the total imaging beam intensity $I_{\text{tot}} = I_1 + I_2$ is kept constant. The results are shown in fig. 4.3 for different total intensities. The solid lines are results from numerical solutions of the optical Bloch equations for the four-level system. The curves are calculated with the effective saturation intensity estimated below and scaled by a constant factor (for details on the simulation see [74]). If transition T2 is not driven ($r = 1$) the total signal is limited by the decay into the dark state. Imaging without transition T1 ($r = 0$) results in no signal, as the initial state of the atoms is not addressed by this light. For the highest imaging intensities the maximum number of scattered photons is obtained at $r \simeq 0.5$, as expected from the steady state solution. For smaller intensities, the optimum is at higher ratios r . This results from the initial pumping dynamics starting in the state $|g_3\rangle$. The atoms have to decay spontaneously to $|g_5\rangle$ and populate it before the transition T2 can contribute. This happens on a timescale of a few microseconds for high intensities and becomes more important for low intensities as the length of the imaging pulse is kept fixed to $10 \mu\text{s}$.

To describe the absorption of light by the atomic cloud, we follow the method presented in [79] where each atom in the cloud is described as an effective two-level system including the effect of saturation. The intensity loss of the light beam can be described by

$$\frac{dI}{dz} = -\hbar\omega\gamma n, \quad (4.4)$$

where ω is the frequency of the light, γ the total scattering rate and n the atomic density [29]. Inserting eq. (2.7) for γ and assuming resonant light ($\delta = 0$) leads to

$$\frac{dI}{dz} = -\sigma_0 n \frac{1}{1 + I/I_{\text{sat}}} I \quad (4.5)$$

with saturation intensity I_{sat} and the resonant cross-section σ_0 given by

$$\sigma_0 = \frac{\hbar\omega_0\gamma}{2I_{\text{sat}}} = \frac{3\lambda_0^2}{2\pi}, \quad (4.6)$$

where λ_0 and ω_0 are the wavelength and frequency at resonance, respectively. From eq. (4.5) we can recover the Beer-Lambert law in the limit of low saturations $I \ll I_{\text{sat}}$, where the fraction approaches unity.



The atomic column density n_c is obtained by solving the differential equation (4.5), which yields

$$n_c = \int n \, dz = \frac{1}{\sigma_{\text{eff}}} \left[\ln \left(\frac{I_i}{I_f} \right) + \frac{I_i - I_f}{I_{\text{sat}}^{\text{eff}}} \right]. \quad (4.7)$$

Here, the final intensity I_f and the initial intensity I_i are the total intensities measured via the signal on the CCD camera with and without the presence of atoms, respectively. We replaced the cross-section and saturation intensity by effective values that incorporate experimental discrepancies from the theoretical values, leaving us with the effective scattering cross-section σ_{eff} and the effective saturation intensity $I_{\text{sat}}^{\text{eff}} = \alpha I_{\text{sat}}$. In particular, the deviation from the bare saturation intensity I_{sat} of a single closed two-level optical cycle captures effects of polarization, detuning fluctuations of the laser from atomic resonance, and optical pumping effects.

To estimate the effective saturation intensity $I_{\text{sat}}^{\text{eff}}$ experimentally, we take absorption images for a constant atom number with different total imaging intensities. The first term of eq. (4.7) can be estimated directly from the number of CCD counts, $I_i/I_f = C_i/C_f$. For the second term we calibrate the camera counts to the central intensity of the imaging beam. The effective saturation intensity $I_{\text{sat}}^{\text{eff}}$ is then inferred by calculating the column density n_c for different total imaging intensity I_{tot} . For the correct $I_{\text{sat}}^{\text{eff}}$ the column density stays invariant, and the procedure is exemplified in the inset of fig. 4.4 for the ratio $r = 0.5$. We find $I_{\text{sat}}^{\text{eff}} = (18 \pm 4) I_{\text{sat}}$, where I_{sat} is the saturation intensity of the bare two-level system.

To predict a value for the effective saturation intensity $I_{\text{sat}}^{\text{eff}}$ in the steady state on resonance we use that the coupled four-level system consists of two standard two-level systems with equal I_{sat} , which are only coupled to each other via the incoherent spontaneous decay of their excited states. Thus, no coherence is built up and the two subsystems can be described as being independent. Here, $\Gamma_{1 \rightarrow 2}$ is the decay rate of the states $|e_3\rangle \rightarrow |g_5\rangle$ and $\Gamma_{2 \rightarrow 1}$ of $|e_{13}\rangle \rightarrow |g_3\rangle$ (cf. fig. 4.2 b). The decay rates between the two parts are determined by the admixture $1 - p$ of the ground states, which gives the probability for a decay, the populations ρ of the respective excited states and the imaging light intensities. We get

$$\Gamma_{1 \rightarrow 2} = (1 - p) \rho_{e_3} \frac{\Gamma}{2} \frac{s_0^{(1)}}{1 + s_0^{(1)}}, \quad \Gamma_{2 \rightarrow 1} = (1 - p) \rho_{e_{13}} \frac{\Gamma}{2} \frac{s_0^{(2)}}{1 + s_0^{(2)}}, \quad (4.8)$$

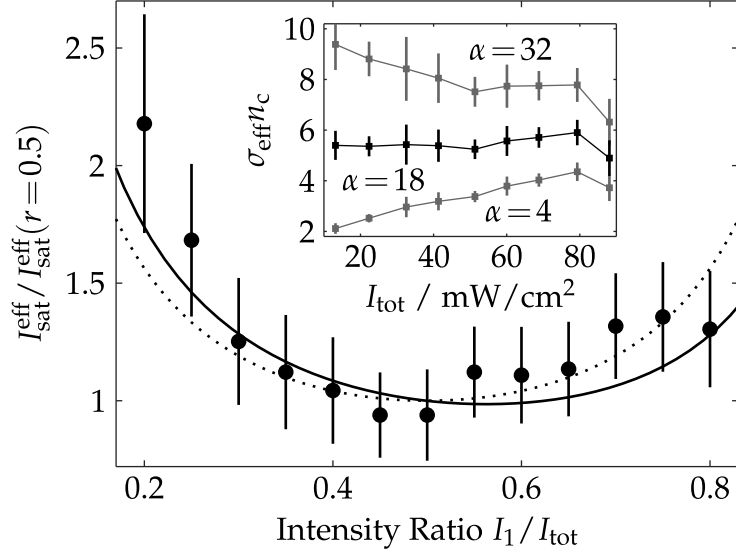


Figure 4.4: Calibration of the imaging system. For each ratio $r = I_1 / I_{\text{tot}}$, the effective saturation intensity $I_{\text{sat}}^{\text{eff}} = \alpha I_{\text{sat}}$ is estimated such that the resulting atomic column density n_c is invariant under changes of the imaging intensity I_{tot} . The inset shows this procedure for $r = 0.5$. The theoretical predictions obtained from the steady state solution and the numerical simulation of the dynamics are depicted by the dashed and solid curves, respectively. The experimental values are scaled by the mean of three points around $r = 0.5$ and the theoretical curves by their respective values at $r = 0.5$. The error bars are estimated by bootstrap resampling. Adapted from [76].

where the saturation parameters $s_0^{(1/2)} = I_{(1/2)} / I_{\text{sat}}$ contain the intensities of the imaging light. In the steady state we have $\Gamma_{1 \rightarrow 2} = \Gamma_{2 \rightarrow 1}$. Subsequently, we describe the four-level system by an effective two-level system, where the total photon scattering γ^{eff} is the sum of the photons scattered by the two individual systems,

$$\gamma^{\text{eff}} = \frac{\Gamma}{2} \frac{s_0^{(1)}}{1 + s_0^{(1)}} + \frac{\Gamma}{2} \frac{s_0^{(2)}}{1 + s_0^{(2)}} = \frac{\Gamma}{2} \frac{s_0^{\text{eff}}}{1 + s_0^{\text{eff}}}, \quad s_0^{\text{eff}} = \frac{I_{\text{tot}}}{I_{\text{sat}}^{\text{eff}}}. \quad (4.9)$$

Solving the resulting system of linear equations, we get an analytic solution for the effective saturation intensity,

$$I_{\text{sat}}^{\text{eff}}(r) = \frac{I_{\text{sat}}}{2r(1-r)}, \quad (4.10)$$



which only depends on the ratio r of the intensities and the saturation intensity of the bare two-level system I_{sat} . In the case of $r = 0.5$ the populations in the two coupled systems are equal and the effective saturation intensity is twice the value of the single two-level system. For different intensities an imbalance in population builds up which reduces the total scattering and thus increases the effective saturation intensity.

We investigate the dependence of $I_{\text{sat}}^{\text{eff}}$ on the ratio r experimentally. The results are displayed in [fig. 4.4](#), and they are compared to the analytical solution discussed before (dashed line). Furthermore, we performed numerical simulations of the optical Bloch equations of the four-level system for different ratios. The resulting relations between scattering and total intensity are scaled to the two-level system, which yields an effective saturation intensity (solid line, details in [74]). At the largest and smallest ratios, deviations between experimental and analytic behaviour arise due to the initial population dynamics of the four-level system, which is captured well by the numerical simulation. From $r \sim 0.4$ to 0.6 the effective saturation intensity varies only slightly, making the calibration of the column density robust against small changes of the imaging intensities. The remaining deviation of $I_{\text{sat}}^{\text{eff}}$ between absolute experimental and theoretical numbers is attributed mainly to instabilities of the magnetic field and imaging laser frequencies. [Section 4.3.3](#) gives a more recent calibration, where the effective saturation intensity is reduced by a factor of 2.

4.2 Overview of the Imaging Setup

Different imaging systems are implemented in the experiment that allow to measure the density distribution of the atomic cloud at the different stages from multiple angles. We start by introducing the systems that are set up in the horizontal plane, which are used to image the atoms from the side. An overview is given in [fig. 4.5](#). For the optimization and monitoring of the MOT a Guppy and a Guppy Pro camera image the fluorescence signal of the atoms. Both cameras are equipped with simple, commercial photography objectives, as a big field of view is wanted and a low resolution is sufficient. The cameras are mounted slightly out of the horizontal plane to get an impression of the atom cloud's shape. Furthermore, the fluorescence light of the MOT is imaged on a photodiode with a single lens. This setup allows for constant monitoring of the MOT fluorescence and enables easy logging of the signal. During the late stages of the experimental cycle the photodiode also detects stray light

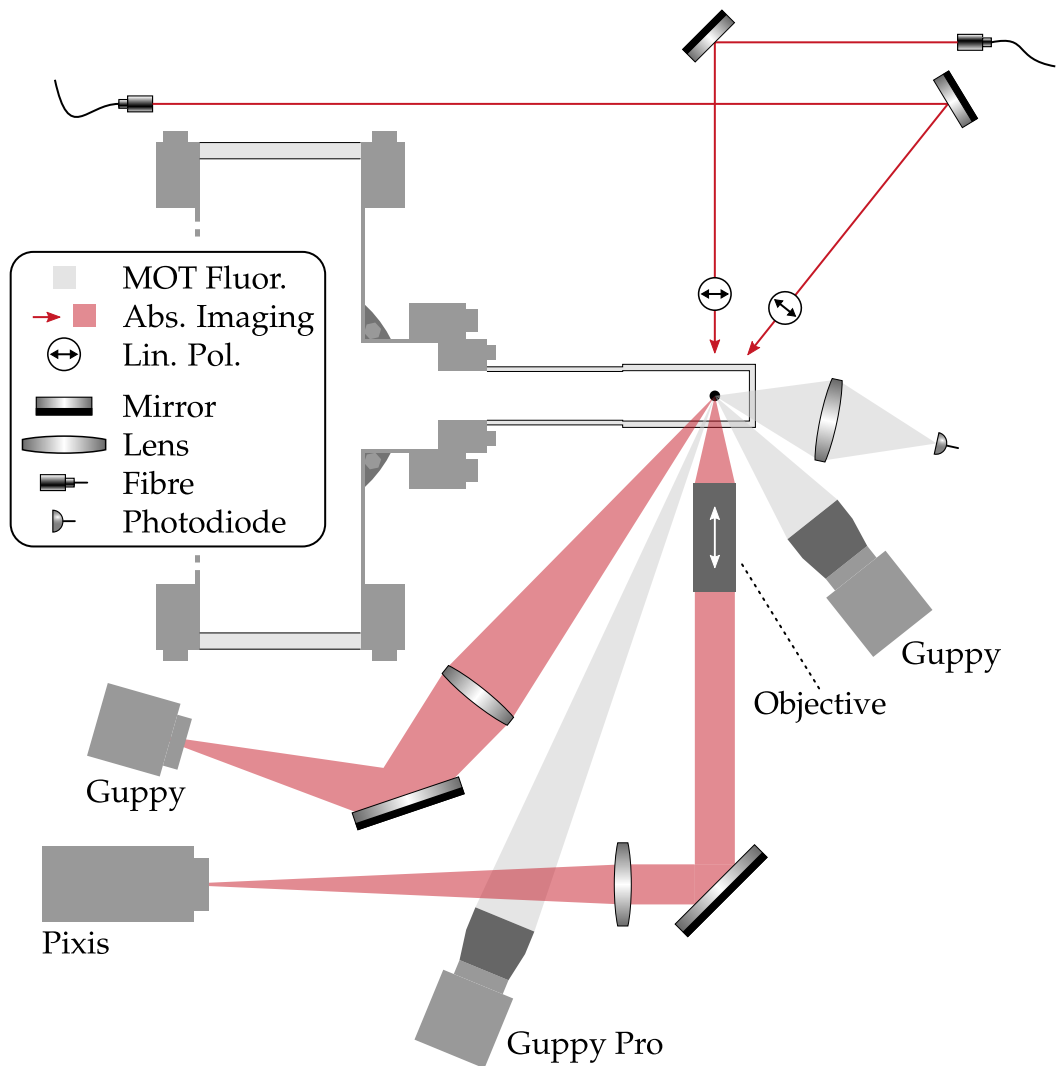


Figure 4.5: Imaging setup in the horizontal plane. The atomic cloud (indicated with the black dot) can be imaged with two cameras (Guppy and Guppy Pro) during the MOT stage by collecting fluorescence light. The cameras are tilted slightly out of the plane to allow for an impression of the cloud's shape, which is helpful during optimization. Furthermore, fluorescence light is collected with a photodiode, which gives an easily accessible quantity for permanent monitoring of the MOT. Absorption imaging provides a tool for optimization of trapping and cooling at later stages of the experimental cycle. A low resolution system is realized with a Guppy camera (magnification 0.9) and the Pixis imaging with magnification 29.0 provides a high resolution imaging system.



from the dipole traps and is thus a useful tool to judge the current status of the experiment. As it is prominently displayed on a voltmeter in the lab, many technical or human errors can be excluded quickly while troubleshooting.

The two remaining imaging systems that are shown in [fig. 4.5](#) are used for absorption imaging predominantly. They are aligned with the horizontal plane and therefore allow imaging of the atomic cloud perpendicular to gravity direction. Thus, time-of-flight measurements can be conducted as the atoms stay in focus while falling, which is useful for example to estimate the temperature of the sample. Both imaging systems can be used at low and high magnetic field, as the necessary lights for absorption imaging are all coupled into all imaging fibres and can be switched electronically (see [section 4.5](#)).

One of the two systems uses a single lens to image the atomic cloud on a Guppy camera. The magnification is calibrated using gravity and it is approximately 0.9, which means the system is slightly demagnifying. It is mostly used for optimization during early stages of the experimental cycle, including the compressed MOT, the grey molasses, the magnetic trap, loading of the crossed dipole trap, and early stages of evaporation.

The second system, called *Pixis Imaging*, provides high resolution absorption images of the atomic sample and is described more closely in [section 4.4](#).

Furthermore, our experimental setup contains a third imaging system oriented perpendicular to the horizontal plane and hence not shown in [fig. 4.5](#). It is called *ProEM imaging* and is introduced in the following section.

Technical details and a list of components can be found in [section B.3](#).

4.3 ProEM Imaging

The *ProEM imaging* system is the main imaging system of the experimental setup. It is aligned in gravity direction, which is necessary to image the two-dimensional atom cloud trapped in the horizontal plane. Because of the magnetic coils the available space in the vertical direction is rather limited and multiple systems need optical access in this axis. In addition to the imaging system this includes light from the DMD and the MOT beams. The way these systems are combined is illustrated in [fig. 4.6](#), and a detailed sketch of the vertical dimensions is given in [fig. D.3](#). Two identical objectives are placed above and below the glass cell, where the upper one projects the light from the DMD into the atomic plane and the lower one is used to image the atomic cloud. The objectives are described more closely in [section 4.3.1](#). They are

mounted on translation stages that are home-built by the institute workshop. The design as well as alignment strategies are discussed in [section 4.3.2](#).

In this section we focus on the optical properties of the imaging system. The laser beam for absorption imaging is shone onto the atomic cloud from above. It is tilted with respect to the glass cell to avoid etalon effects. Two lenses form a telescope with the upper objective, such that the beam is collimated in the atomic plane (cf. [fig. 3.7](#)). Due to spatial restrictions there are two individual secondary lenses for MOT beam and imaging beam, respectively, and the exact setup is detailed in [fig. 4.12](#). After passing the glass cell and the atomic cloud the imaging light is collected by a custom-made, commercial objective (designed and built by *Special Optics*). It is infinity-corrected and has an effective focal length of $f_{\text{eff}} = 35$ mm. A secondary lens with a focal length $f = 1000$ mm focusses the light on a ProEM camera. The lens is mounted on a piezoelectric translation stage to adjust the focus of the system in a small range. The relation between the shift of the objective and secondary lens is elaborated in [appendix A](#). In front of the camera an external shutter blocks light during the experimental cycle and is opened before the images are taken. It is not directly connected to the camera to minimize vibrations. Additionally, a single-band bandpass filter blocks all light except for the 767 nm imaging light and a 532 nm single notch filter blocks most of the high intensity DMD light. Both are necessary because the mechanical shutter takes about 50 ms to open, during which stray light from the dipole traps or DMD light could fall on the camera. [Figure 4.6](#) shows the path of the imaging beam in red, where the red shaded area after the atoms is the absorption signal (signal of a point source).

For the imaging sequence special precautions have to be taken. The camera chip has a size of 1024x2048 pix and its lower half is blacked out to serve as a storage register during the readout. In principle, the camera supports taking two pictures shortly after each other. In this mode the first picture is taken and immediately transferred to the lower half. A second picture can be taken in the upper region while the slow readout of the first is still taking place. However, we find that triggering the camera two times shortly after each other, which means that the camera is reading out the first picture while the second trigger arrives, leads to strongly enhanced fluctuations in a circular region on the image. As a workaround, we trigger the second time only after the first picture is read out as the exposed pixels of the upper region collect the photoelectrons even without a trigger.

The magnification of the imaging system is calibrated exploiting the



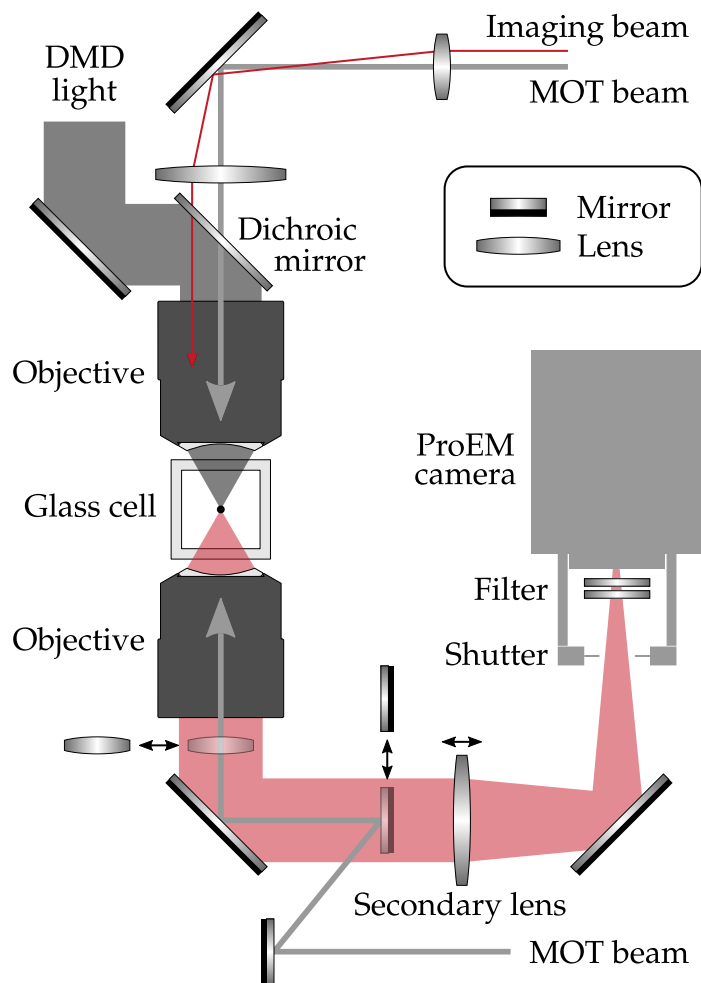


Figure 4.6: Vertical beam paths at the glass cell. The vertical beam axis is shared among different systems. For absorption imaging a resonant laser beam is shone on the atoms from above (red). The light is collected by the lower objective and imaged onto a ProEM camera. An external shutter and two filters block ambient light. Also from above, light from the DMD with a wavelength of 532 nm is overlapped with the vertical axis by a dichroic mirror. It is imaged with the upper objective onto the atoms as a repulsive potential. From both sides, the MOT beams are shone onto the atoms during the early phase of the experimental cycle. In the lower path, a retractable mirror and lens are moved into the imaging path during the MOT stage (shaded position) to ensure a collimated beam after the objective. In the upper path, the same is achieved by a static telescope for both imaging and MOT beam. For spatial restrictions both beams have an individual second lens, which is not shown in this sketch.

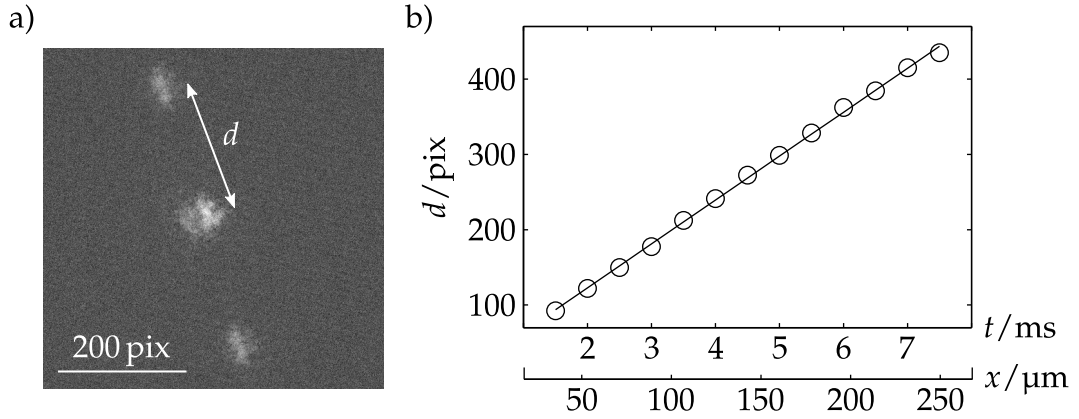


Figure 4.7: Spatial calibration of the ProEM imaging system. The left panel shows two groups of atoms that move out from the condensate in the middle of the picture after the application of a Bragg pulse (evolution time 3.5 ms). On the right, the distance d of the atoms from the condensate is plotted versus the evolution time t . With the velocity v of the atoms (see main text) the time can be converted to the distance x covered by the atoms. The slope of the linear fit reveals the calibration of the imaging system.

dynamics of the atomic cloud after a Bragg pulse. We illuminate the condensate for 0.3 ms with a retroreflected laser beam. It has a wavelength of $\lambda = 765.94$ nm and a power of about 100 mW. The laser beam forms a standing wave with wavelength $\lambda/2$ and imprints this structure as a phase onto the atoms. Thus, a momentum mode $p = 2h/\lambda$ is excited. As shown in fig. 4.7 a), atoms are ejected along the direction of the beam and move outward with velocity $v = p/m$, where m is the mass of ^{39}K . Part b) shows a plot of the distance d the atoms have moved in an evolution time t . From the wavelength of the standing wave we can calculate the velocity of the atoms and convert the time axis to distance covered by the atoms. The slope of a linear fit gives the calibration of the imaging system with $0.45 \mu\text{m}/\text{pix}$ which leads to a 35-fold magnification.

4.3.1 Characterization of the Objective

This section describes and characterizes the high resolution objective used for the ProEM imaging system and the DMD assembly. The two identical objectives are designed and manufactured by *Special Optics*, and a technical drawing is given in fig. D.1. As illustrated in fig. 4.6, they are located above



and below the glass cell, respectively, with a working distance of 3.43 mm air, 4 mm glass and 15 mm vacuum. Each objective has a numerical aperture of 0.5, the effective focal length is $f_{\text{eff}} = 35$ mm, and a total transmission of 0.91 is stated in the specifications. The radius of the field of view, where the objective is diffraction limited, is greater than $250 \mu\text{m}$ for 767 nm light and about $230 \mu\text{m}$ for 532 nm light (calculations from the manufacturer). We measure the back focus of the objective to be 7 mm behind the last surface, which coincides with the end of the objective housing.

To characterize the performance of the objective, we estimate the resolution according to the Rayleigh criterion [80]. The response of a diffraction-limited imaging system to a point source is given by an Airy function, and it is called the point spread function (PSF) of the system. For such a system the Rayleigh criterion defines the resolution by the distance between the maximum and first minimum of the PSF. Experimentally, we provide the point-like source with a gold foil target, which has holes of 650 nm diameter arranged in a grid pattern with a spacing of $20 \mu\text{m}$ [81]. The setup for the resolution measurement is shown in fig. 4.8 a). The gold foil target is illuminated with a laser beam and imaged with the objective. To emulate the glass cell, a glass window with the same thickness and type of glass is placed at the right position between the gold foil and the objective. After passing through the system, the light is re-imaged onto a Guppy Pro camera with a secondary lens ($f = 500$ mm). We start with our main wavelength of 767 nm. An example image is shown in fig. 4.8 b), where each bright dot belongs to a hole in the gold foil. From the distance between the holes we can calibrate the magnification of the imaging system. In the next step, a two-dimensional Airy function is fitted to each hole and the resolution R is estimated as the distance between the maximum and the first minimum of the Airy function. We get a resolution of $R = (0.97 \pm 0.02) \mu\text{m}$ as indicated by the central value for $\Delta d = 0$ in fig. 4.8 c). This result is close to the theoretically expected value for a diffraction limited system,

$$R_{\text{diff}} = 1.22 \lambda / (2 \text{NA}) = 0.936 \mu\text{m} , \quad (4.11)$$

where λ is the wavelength of the light and NA the numerical aperture of the setup, which is limited by the entrance pupil of the objective. The small deviation of the experimental value might stem from an imperfect alignment of the focus, which is adjusted by minimizing the spot size by eye. Furthermore, we test the robustness of the system against the position of our atomic cloud in the glass cell. This is emulated by shifting the position of the glass plate

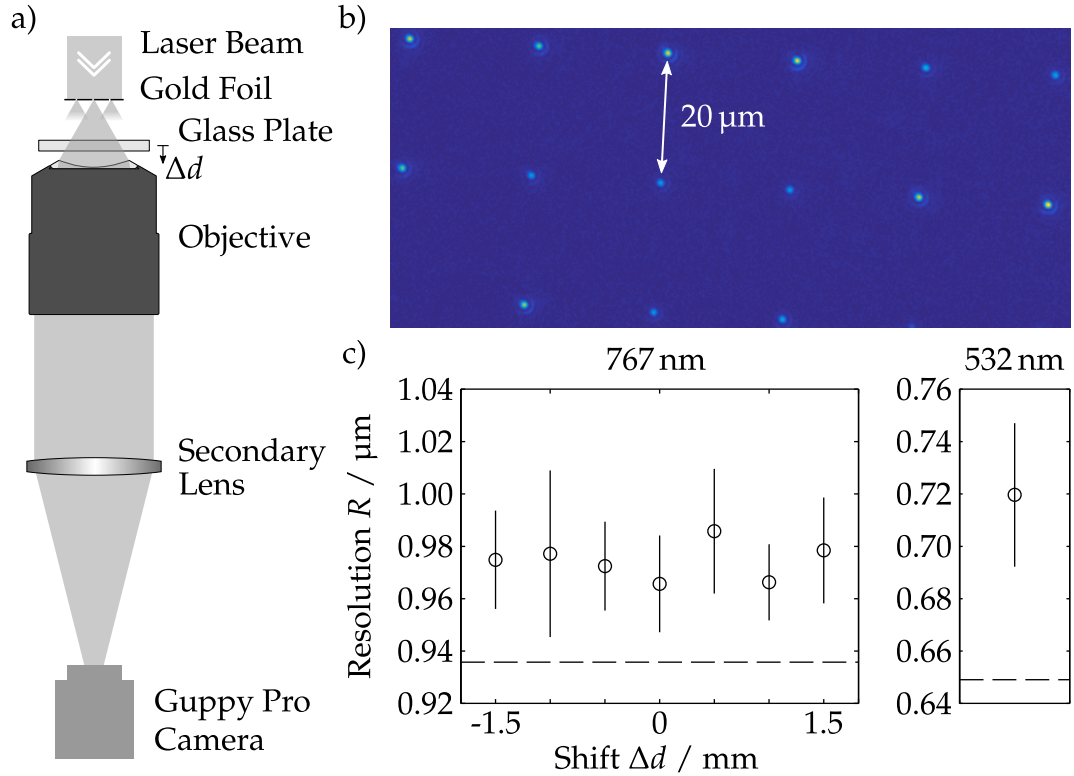


Figure 4.8: Measurement of the resolution for the ProEM objective. Part a) shows the measurement setup. A gold foil target is illuminated with a laser beam and acts as a point-like source. Subsequently, the light is diffracted by a glass plate mimicking our glass cell and collected by the objective. A secondary lens focusses the light on a Guppy Pro camera. A cut-out of an image of the gold foil target is shown in part b) where the bright spots are the images of the point-like sources. Fitting a two-dimensional Airy function to the spots, the resolution R according to the Rayleigh criterion can be extracted. Part c) gives the resolution when illuminating the target 767 nm and 532 nm , respectively, and the dashed lines indicate the diffraction limits. For 767 nm we mimic a shift of the atomic cloud in the glass cell by shifting the glass plate, and extract the resolution for different positions. Within the range of 3 mm no significant deviation in the resolution is observed. Overall, we get a resolution close to the diffraction limit, and the small deviation might result from an error of the focus, which was adjusted by eye.



and re-focussing the objective on the gold foil. Figure 4.8 c) shows that the absolute position of the glass plate is not critical, which indicates that the atomic cloud does not need to be accurately centred within the glass cell to reach a good performance of the imaging setup.

Finally, we test the objective with laser light of the wavelength 532 nm, which we use to implement a dipole trap with the DMD. The result is shown in the right plot of fig. 4.8 c) and gives a resolution of $R = (0.72 \pm 0.03) \mu\text{m}$. The deviation from the theoretical value $R_{\text{theo}} = 649 \text{ nm}$ might result from the size of the holes in the gold foil, which become resolvable for green light as their size is bigger than the wavelength. Furthermore, the focus was again adjusted by eye, which might lead to a small imprecision.

4.3.2 Imaging Assembly

To mount the objectives below and above the glass cell, we designed a holder tailored to the requirements on alignment and space available. A sketch of the setup is shown in fig. 4.9 and technical drawings of the parts can be found in section D.4. The holder is fixed to the table with three legs, two of which are located close to the vacuum chamber and one is positioned in front of the glass cell. The latter is placed in the area that is already optically blocked by the holder of the dipole traps. This way, the legs of the holder do not block any optical access. An upper and a lower support platform are screwed onto the legs. The lower platform consists of two parts to allow the assembly of the part without dismantling the holder of the magnetic coils. Both objective holders feature a tip/tilt stage with differential micrometer heads. They allow for coarse and fine adjustment, where the latter has a travel range of only $25 \mu\text{m}$ per revolution. Additionally, the upper part includes an x/y-translation stage with a range of 6.5 mm for each axis. The legs are manufactured from brass as it is rigid and non-magnetic, and the holder is made out of PEEK to inhibit eddy currents and residual magnetization of the material. The commercial components such as springs and micrometer heads are listed in table B.4.

The objective features an outer thread with a small slope. It is screwed into the tip/tilt stage, which has a matching inner thread, and is fastened with a lock nut. This allows for easy adjustment of the approximate focus position and simplifies the installation.

In the following the installation process of the lower objective is described. First, we set up a resonant guide beam to support the adjustment (cf. fig. 4.12).

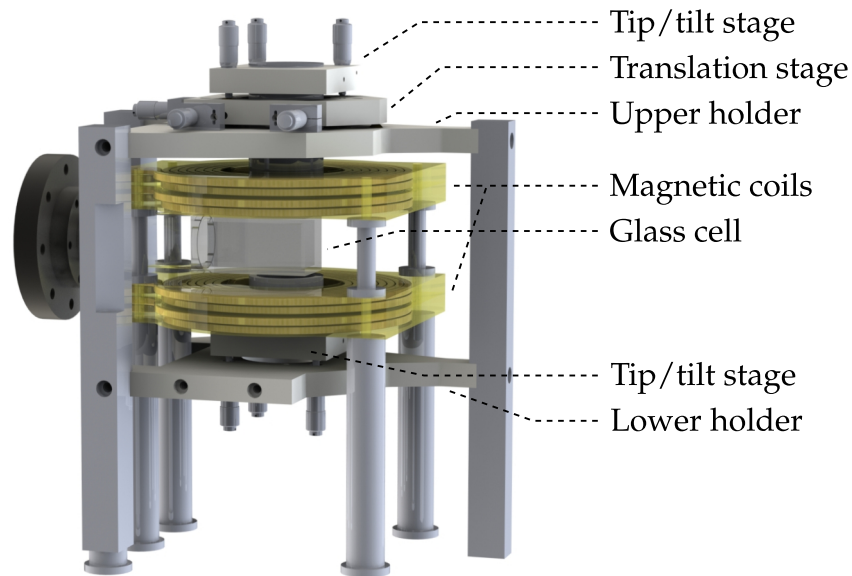


Figure 4.9: Objective holder and magnetic coils around the glass cell. Close to the glass cell in the centre of the sketch the main magnetic coils are mounted. Their front legs are placed such that they are in line with the edges of the glass cell when looking at the atomic cloud to minimize the blockage of optical access. The objectives are mounted through the coils above and below the glass cell on a tip/tilt/translation stage and a tip/tilt stage, respectively. The holders are manufactured from PEEK to prevent eddy currents and residual magnetization. They are mounted on three posts to keep most optical access, where the right post fits in a gap in front of the holder for the dipole traps (not shown here).

This beam is aligned to hit the atomic cloud and to be parallel to gravity. The latter is achieved by retro-reflecting the beam off a methanol surface back into the fibre-coupler. We choose methanol because of its low surface tension. The alignment of the beam is marked with an iris behind the planned position of the objective. Next, the objective is screwed in the holder. We place a glass plate on top of the objective and adjust the tip/tilt stage such that the guide beam is back-reflected into the fibre-coupler. Hence, the objective is aligned with gravity. Next, a lens is fixed on the back of the objective to form a one-to-one telescope. The holder with the objective is shifted such that the guide beam is centred on the iris again, which ensures proper alignment with the optical axis. For a first adjustment of the focus we measure the distance



between glass cell and objective, and set it to the theoretical working distance. A fine adjustment of the focus is achieved with the atomic cloud. A density dip is imprinted in the condensate with a dipole beam and we optimize the focus for minimal size with the micrometer screws and the secondary lens. The upper objective is built in similarly, where the remaining relative translational alignment is carried out with the micrometer screws.

The holder has proven to be very stable. After initial focussing with the secondary lens no substantial shift in the focus was observed. Keeping as much optical access available as possible is helpful for every-day lab work and further upgrades of the setup.

4.3.3 Calibration

For absorption imaging with high intensities it is important to calibrate the system for the non-linear response of the atomic cloud. [Section 4.1.2](#) discusses the calibration method for our imaging scheme and showcases it for a three-dimensional cloud. In this section we perform the calibration for a quasi two-dimensional atomic cloud with harmonic confinement in the radial direction and describe the measurement of the atom number for this configuration.

For the calibration we take absorption images with different total imaging intensities I_{tot} . The quasi two-dimensional atomic cloud is trapped in the pancake lattice with harmonic confinement in radial direction (cf. [section 3.4](#)). All images should yield the same atomic column density n_c for the correct calibration factor, and [fig. 4.10](#) shows the results for three different factors α (cf. [section 4.1.2](#)). The best result is obtained for $\alpha = 7.3 \pm 0.1$, where we estimated the error by bootstrap resampling. The lower value for α in comparison to the calibration for the three-dimensional cloud in [section 4.1.2](#) implies that more photons are scattered at a given imaging intensity, which leads to a better quality of the imaging signal. We attribute this enhancement to improved stability of the magnetic field and the imaging lasers themselves.

To extract an absolute atom number from this signal with calibrated non-linearities, a value for the effective cross-section σ_{eff} is needed. It can be obtained by detection of atomic shot noise [82] or a comparison of the experimental data to theory predictions. For this comparison we perform systematic measurements of the quasi two-dimensional cloud with harmonic confinement for different interaction strengths and different radial confinements. Both parameters change the radial expansion of the cloud in a characteristic

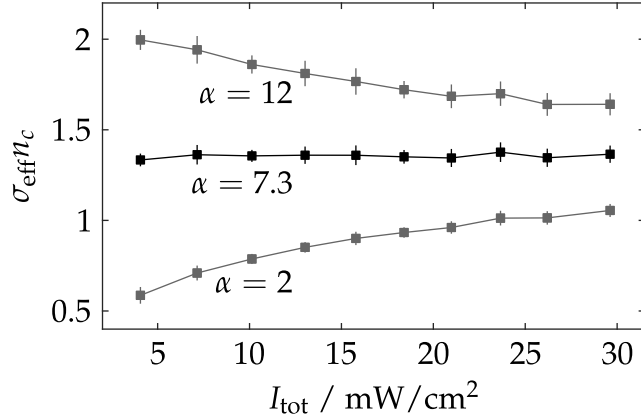


Figure 4.10: Calibration for two-dimensional atomic cloud. The cloud is confined in the radial direction with a harmonic trap (cf. section 3.4). We take absorption images with different total imaging intensities I_{tot} . As the atom number stays constant, the atomic column density n_c should as well. This is ensured by choosing the right calibration factor α as depicted by the three examples. The best results are obtained for $\alpha = 7.3$. A detailed explanation is given in section 4.1.2.

way. We compare this expansion to ground state results of a three-dimensional GPE simulation when varying the same parameters. The radial expansions of the experimental results and theoretical predictions only fit together for the correct choice of the total atom number, which we estimate to be $N = 23000$.

4.4 Pixis Imaging

The *Pixis imaging* system provides images of the atomic cloud perpendicular to gravity with a high resolution. The setup is shown in fig. 4.5. It makes use of a home-built, infinity-corrected objective made from off-the-shelf components with an effective focal length of $f_{\text{eff}} = 35$ mm. With a secondary lens ($f = 1000$ mm) the light is focussed on a Pixis camera leading to a magnification of ~ 29 . The objective blocks the MOT beams when it is in the position of the focus, and it is thus placed on a motorized translation stage and moved out during the early stages of the experimental cycle. Moreover, the motorized stage allows for easy adjustment of the focus.

The design of the home-built objective is inspired by [83, 84], and it is adapted to our setup where the first section of the beam path is fixed to 15 mm



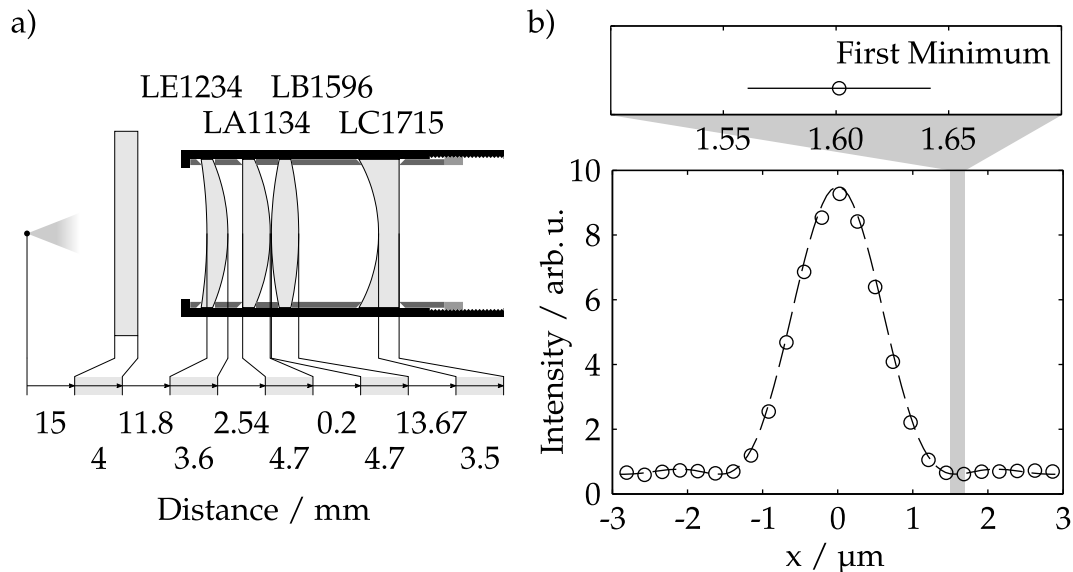


Figure 4.11: Dimensions and quality of the home-built objective. Part a) shows from left to right a point source, a part of the glass cell and a sketch of the objective along with its dimensions. The lenses of the objective are standard components manufactured by THORLABS, and the article numbers of the four lenses are stated above. The housing and spacer rings are home-built by the workshop of the institute. Part b) shows the results from measuring the resolution with the gold foil method explained in [section 4.3.1](#) at a wavelength of 767 nm. For a single point-like source a cut of the PSF and the fit with an Airy function is plotted in the lower part. The upper part gives the position of the first minimum averaged over all point-like sources of the gold foil, which is a measure for the resolution of the system.

vacuum followed by 4 mm glass. Starting with the design reported in the publications we optimized the layout of the objective iteratively using a ray tracing software. One by one, the optical elements are replaced by catalogue lenses and the remaining elements are re-optimized. The resulting design is diffraction limited and the final spacings are given in [fig. 4.11 a\)](#). All lenses are standard components from THORLABS with an 1 inch diameter. We designed spacer rings accordingly (technical drawings in [section D.2](#)), and the rings are manufactured by the institute workshop with a fitting lens tube.

The objective is tested using the gold foil method described in [section 4.3.1](#) with 767 nm laser light. The results are depicted in [fig. 4.11 b\)](#), where the lower plot shows a cut along the intensity profile of an imaged hole of the

gold foil, which is a measure for the PSF of the optical system. We estimate the resolution of the system by fitting an Airy function to the images of all point-sources of the gold foil, and calculate the resolution $R = (1.60 \pm 0.04) \mu\text{m}$ as the mean over all measured PSFs. It is depicted in the upper part of the plot. The diffraction limit $R_{\text{diff}} = 1.34 \mu\text{m}$ can be calculated from the numerical aperture $\text{NA} = 0.35$ of the system according to eq. (4.11), which demonstrates that our home-built objective works close to the diffraction limit. The NA results from the total working distance of 30.8 mm and the width of the objective's entrance pupil, which is 23.4 mm.

4.5 Laser System for Imaging

The laser setup provides light for imaging at low magnetic field, where the frequencies are close to the cooler and repumper transitions, and at high magnetic field in the region of 550 G. At this field the resonance is detuned by a large frequency of about ± 850 MHz from the D2 reference, and the two imaging lights are about 1.7 GHz apart. Since these frequencies are too far apart to be efficiently produced with AOMs we use two external cavity diode lasers which we stabilize on the D2 reference laser (cf. section 3.3) with an offset lock [85]. As shown in fig. 4.12 a) we divert a small part of the imaging light of each laser, overlap it with the reference light and detect the beating on a fast photodiode. Subsequently, the high frequency signal is mixed down and an error signal is generated, which can be shifted by an external voltage to tune the frequency of the light. The laser is then stabilized with a PI controller. A detailed description of the setup can be found in [75].

The second part of the setup contains three AOMs in double-pass cat-eye configuration. They allow for a fast switching of the imaging light with a typical pulse length of $10 \mu\text{s}$ and a regulation of the laser power. This part is connected to the first part with optical fibres to allow easy maintenance and alignment, and it is depicted in fig. 4.12 b). The beams are combined with cascaded beam splitters after the AOM paths such that every camera can be used for low and high field absorption imaging. Note that the polarizations of the two imaging lights are co-aligned for the Guppy and Pixis imaging, whereas the polarization of the high field σ^+ light for the ProEM imaging is perpendicular to the other polarizations. The lights are coupled into fibres that guide it to the experiment. Additional mechanical shutters in front of the fibres ensure that light is transferred to the experiment only during imaging (shutters not shown in schematic).



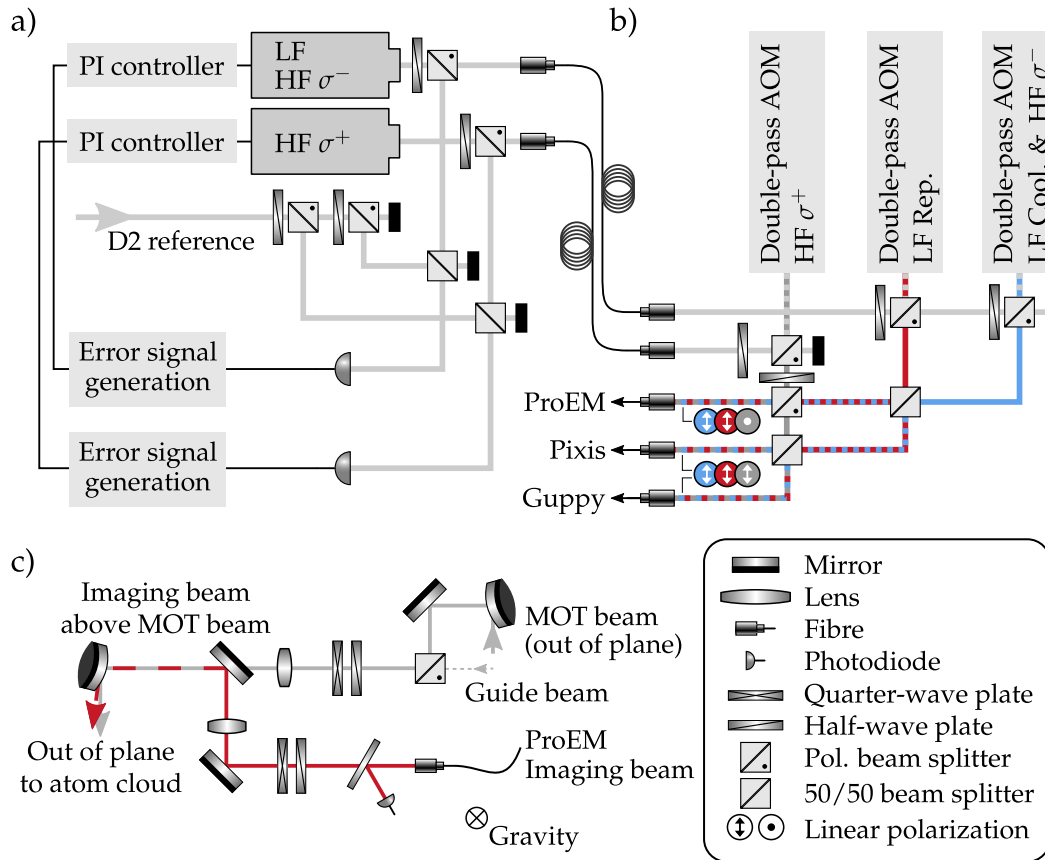


Figure 4.12: Laser system for imaging. Part a) and b) show a sketch of the laser system that produces the frequencies for low field (LF) and high field (HF) imaging. Two lasers are stabilized with an offset locked to the D2 reference laser and the light is coupled into optical fibres (part a, mirrors omitted for clarity). The frequency is then shifted by double-pass AOMs which also enable fast switching of the light. Finally, the light is mixed such that every imaging system gets all frequencies at the right polarizations (part b, mirrors omitted). Note that the polarizations for HF σ^- and HF σ^+ light are perpendicular to each other for the ProEM. Part c) depicts a sketch of the optics for the ProEM imaging beam and the upper MOT beam. For both, the final polarizations are set with a quarter-wave and half-wave plate to compensate the dichroic mirror later in the beam path. Additionally, the imaging beam is equipped with a photodiode to stabilize its power. As noted here and shown in [fig. 4.6](#), the imaging beam is set up above the MOT beam to enter the glass cell under an angle and avoid etalon effects. Part a) and b) adapted from [\[35\]](#).

The frequencies of the imaging lights are determined by the setting of the offset lock and the AOMs. For imaging at low field, one laser close to the D2 reference suffices and the light is generated with two AOM paths that shift the frequency to the cooler and repumper transitions, respectively. At high field the AOM paths are predominantly used for switching, and the frequency is set by the offset lock (for details see [75]).

The imaging light is transferred to the experimental setup with optical fibres. Figure 4.12 c) depicts the path of the ProEM imaging beam at the experiment. After the fibre out-coupler, a small part of the light is reflected onto a photodiode. At the beginning of each experimental cycle the different imaging lights are turned on one after the other to calibrate their intensities. This is done with a PI controller that tunes the rf-power of the corresponding AOMs. The light is switched off again, and the appropriate voltage is stored by a sample-and-hold circuit which is implemented in the control loop. This allows to tune the intensities of the imaging lights individually and prevents slow drifts of the system. The imaging light passes a half-wave and a quarter-wave plate to transform the linear to a circular polarization. Both plates are needed as the light passes through a dichroic mirror later in the beam path (cf. fig. 4.6), and we adjusted the wave plates to receive circular polarization after the dichroic mirror. As the polarizations of the two frequency components for high field imaging are perpendicular to each other they are transformed into left and right-handed circular light, respectively. Thus, they drive their according transition and signal-to-noise is increased in comparison to the use of linearly polarized light, which has both left- and right-handed components. Furthermore, the imaging beam passes several lenses that correct for the focussing of the upper objective. The first lens is shown here, and the distances and focal lengths are given in fig. 3.7. Due to spatial constraints we use two individual lenses for the imaging beam and the MOT beam, respectively. Both beams are reflected down towards the atomic cloud by a mirror, where the imaging beam sits above the MOT beam to enter the glass cell under an angle and avoid etalon effects.



Physical Computing

Over the last decades, artificial neural networks have gained a lot of interest in the field of machine learning and artificial intelligence. Many classes of network architectures exist, and they are used for a plethora of tasks such as data classification or regression. The networks are usually implemented in software, and their training and operation require a lot of computational power. To accelerate typical computational steps dedicated hardware is developed.

A more direct approach is the implementation of parts, or even of a whole network, in a physical system. First approaches of electronic implementations date back to the 1960s [86], and in the 1980s the first optical systems were realized [87, 88]. Shortly after the development of the liquid state machine [89] in the early 2000s a physical implementation was suggested [90] and implemented in a bucket of water [91]. The architecture was unified to the reservoir computing (RC) framework [21] together with similar concepts, and the implementation of RC or simpler models similar to kernel machines [92, 93] in diverse physical systems became popular. To name a few, there are examples of optical implementations that promise high speed analysis or classification [94–97] and electronic implementations that investigate non von Neumann architectures and might lead to lower energy consumption than traditional microchips [98]. In the field of robotics the use of complex mechanical structures as computational resource and the actuation of soft robots is investigated [99–101]. More implementations are discussed in the reviews [23–25].

In this chapter we show the implementation of an effective single-layer model in a Bose-Einstein condensate. This is a special physical system as it is well isolated from the environment and features a high level of coherence. We start by introducing both support-vector machines and reservoir computing in general and discuss requirements for the implementation in a physical system. Next, we focus on our experimental implementation and explain the training process. We then investigate different experimental parameters relevant for the learning process and discuss the results.

5.1 Fundamentals

This section gives a short overview of kernel machines and reservoir computing, and we discuss the requirements on physical systems for the implementation of such a model.

Conventional Models We start by introducing the general formalism, and this section follows mainly [22]. The task is to learn a functional relation f that maps inputs $x_i \in \mathbb{R}$ to the desired outputs $u_i \in \mathbb{R}$ as given by a training dataset $\{(x_i, u_i)\}$, where $i = 1, \dots, N$ and N is the number of training points. Although we assume the inputs and outputs to be in \mathbb{R} , they can be of higher dimension in general. To estimate the success of our procedure we calculate the root-mean-square (rms) error

$$\varepsilon = \sqrt{\frac{1}{N} \sum_k (y_k - u_k)^2}, \quad (5.1)$$

with the results $y_k = f(x_k)$ for a *non-temporal* task, where the data points $\{(x_i, u_i)\}$ are independent of each other. In a *temporal* task on the other hand, the data points have a specific order and $i = 1, \dots, N$ represents a discrete time domain. The result $y_k = f(\dots, x_{k-1}, x_k)$ depends on the earlier input values, which means that the function we want to learn has to have some sort of memory. For a non-temporal task this is not necessary.

Non-temporal tasks can not be solved using only a linear model in general. Instead, many approaches first expand the input x_i in a non-linear fashion to a high-dimensional feature vector n_i . In this space the solution can then be obtained by linear regression and can be written as $y_i = n_i \cdot w$, where the vector w is obtained from the data by minimizing eq. (5.1). Traditionally the expansion functions are called kernels, and methods using them are referred



to as *kernel machines* [92, 93]. These methods often employ the so-called kernel trick, which allows executing the calculation of inner products of elements of the feature space in the original space. As the original space is of much lower dimension, calculations are significantly cheaper to execute there. Although the training procedure is a rather simple process, the expansion function has to be chosen by hand in a trial-and-error process for many methods.

Temporal tasks can also be solved by expanding the input, but the expansion function needs to fulfil more requirements. It has to have memory, which means that the history of the input is taken into account. Such an expansion is given by the framework of *reservoir computing* (RC) [21], which was derived as a unification of the *echo state network* [102] and the *liquid state machine* [89]. The echo state network was developed to offer a practical training method for recurrent neural networks. It features a (not necessarily) randomly connected recurrent neural network, which is kept unchanged during the training process and is called the reservoir. It is driven by the temporal/sequential input signal and stores information on the history of the latest inputs. This is formalized in the echo state property [102]. The output is derived by a linear combination of weighted reservoir states, and these output weights w are trained by linear regression. The approach has been studied extensively, and more recently it was shown that echo state networks are capable of universal approximation [103]. The liquid state machine was proposed with biological learning models in mind. It is similar to the echo state network but instead of random connections the topology and connectivity of the reservoir is chosen to be locally connected to mimic neural microcircuits of the brain. Reservoirs of this type are typically called a liquid, and their operation liquid computing.

The models presented for non-temporal and temporal tasks have a similar structure. They both encode the input non-linearly in a high-dimensional feature space, where a linear readout becomes possible. An illustration of these *shallow models* is given in fig. 5.1 a) and they feature only two layers, opposed to deep neural networks with many layers.

Physical Models The feature space is not restricted to mathematical models, but appropriate physical systems can also provide such a high-dimensional space. They need to be interfaced properly to encode the input, and require some sort of memory capability to solve temporal tasks. For RC models that solve such temporal tasks the term *physical reservoir computing* is commonly used. For non-temporal tasks, however, such a term has not been coined, and many names for specific physical implementations exist or are sometimes

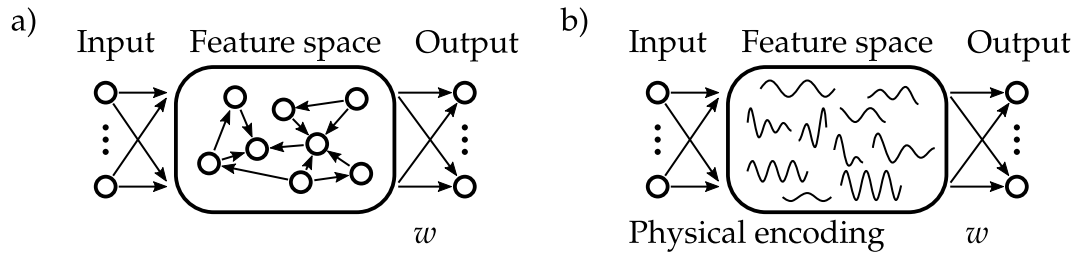


Figure 5.1: Conventional and physical implementation of a shallow model. Part a) exemplifies the conventional implementation of a shallow model with RC, where inputs are fed in a static recurrent neural network which acts as high-dimensional feature space (reservoir). The output is linearly combined from this space with the output weights w . For a physical implementation as shown in part b) the feature space is realized by an adequate physical system (indicated by waves). The input is encoded in appropriate physical quantities and the output is linearly combined from quantities read out from the physical system. Figure adapted from [23].

attributed falsely to physical reservoir computing. The term closest to the original mathematical model would be *physical kernel machines*, which was recently used to describe a photonic implementation [97]. To avoid these confusions we use the general term *physical computing* (PC). It includes physical implementations of shallow models for both non-temporal and temporal tasks. An illustration of such an implementation is given in fig. 5.1 b).

The prerequisites for a good feature space that have been discussed and formulated for conventional RC [102, 104, 105] and kernel machines [92, 93] can not easily be translated to physical systems. In [23] four rather general requirements are formulated for temporal tasks, which we can adapt here. First, the feature space has to be high-dimensional to capture the different inputs. Second, the feature space should exhibit non-linear behaviour to act as a non-linear mapping. Thus, inputs that are not linearly separable can become linearly separable after evolution (and vice versa). Third, the feature space should be tolerant to noisy inputs and distinguish them from actual changes in the input. For non-temporal tasks, these prerequisites on the feature space should suffice. For temporal tasks the fourth criterion is that the feature space should additionally exhibit a fading memory to store information on the latest inputs. If the feature space exhibits all four requirements, we call it a reservoir.

Regarding the property of separation it is often recommended for conventional reservoirs that parameters of the system should be set close to the



so-called edge of chaos [106, 107], where the system is close to exhibit chaotic behaviour. This should support the separation of input values, but a more recent study [108] shows that this is not favourable in general and the setting depends on the nature of the tasks.

In the following section we introduce our specific implementation for physical computing with a Bose-Einstein condensate. Apart from the proper setting of the feature space (reservoir) with the physical system one has to choose the encoding to and the decoding from the system. Our approach is inspired by the papers [109, 110], which theoretically explore the use of non-linear waves for physical computing of non-temporal tasks. In [109] the authors encode inputs as a sum of plane waves and explore subsequent non-linear dynamics under the evolution of the GPE. One has to note that some results in this publication are obtained in the regime of overfitting, where a low training error is obtained by an excessive number of fitting parameters and predictive power is limited (see section 5.2.3). The paper [110] discusses the use of an attractive soliton train as a computational resource. Inputs are encoded in the position of single solitons, which are then evolved with the GPE.

5.2 Implementation

This section describes how we utilize our atomic system as a computational resource and it gives details on the experimental implementation with a quasi one-dimensional BEC. As a proof-of-concept we solve non-temporal tasks, in particular a regression and an interpolation task of the function $u(x) = \sin(\pi x)/(\pi x)$, where $x \in [-3, 3]$. This is a typical non-linear test function and we note that the choice of one input and one output dimension is no fundamental limitation for our implementation. Furthermore, we show later that our BEC can be viewed as a reservoir according to the conditions set in section 5.1 and thus refer to the atomic cloud as such. Both points are discussed in more detail in section 5.4.

Our implementation can be summarized as follows. First, an input value $x_i \in \mathbb{R}$ is encoded in the atomic cloud, where $i \in 1 \dots N_x$, with N_x the number of input values. This is performed by imprinting a jump in the phase ϕ of the condensate at position z_i . After a certain evolution time of the reservoir, the atomic density is read out by imaging the cloud, normalized and binned. This results in the density distribution $n_i \in \mathbb{R}^{N_C}$, where N_C is the number of binning points, also called output channels. The density is normalized and

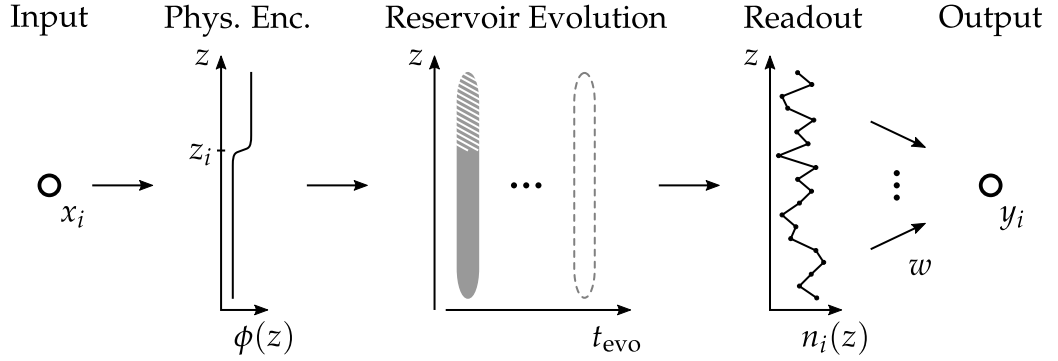


Figure 5.2: Physical Computing with a Bose-Einstein condensate. An input value x_i is encoded physically in a quasi one-dimensional BEC as the position z_i of a jump in the phase ϕ . After a time evolution of the reservoir we extract the normalized and binned density n_i . A vector multiplication with the obtained weight vector w yields the output value y_i .

multiplied with the weight vector $w \in \mathbb{R}^{N_c}$ to yield the result $y_i \in \mathbb{R}$. This weight vector w is found by minimizing the rms error ε of the results y_i with respect to the target values u_i for all N_x input values (cf. eq. (5.1)). For a single input x_i , the process is depicted in fig. 5.2 and can be summarized by

$$x_i \xrightarrow{\text{Phys. enc.}} z_i \xrightarrow{\text{Evo. \& readout}} n_i \xrightarrow{\text{Apply weights}} y_i = n_i \cdot w \quad (5.2)$$

To confirm that the procedure works we test the obtained weight vector w with different experimental realizations for the same input values. The following sections give an in-depth presentation of the single steps.

5.2.1 Physical Encoding

This section revisits the properties of our atomic cloud and introduces the encoding of the input values by a phase imprint.

After the preparation of the condensate as discussed in section 3.5.2 we end up with a quasi one-dimensional atomic cloud trapped by blue-detuned light from the pancake lattice and the DMD. The cloud has a length of $l_{\text{BEC}} = 85 \mu\text{m}$ and it is prepared at a scattering length of $50 a_B$, where a_B the Bohr radius. From the velocity of a density peak we estimate the chemical potential to be $\mu = 1.2 \text{ kHz}$ (cf. eq. (3.2)).

Subsequently, the input is encoded in the condensate as the position of a jump in its phase. We found that it is important to represent the continuous



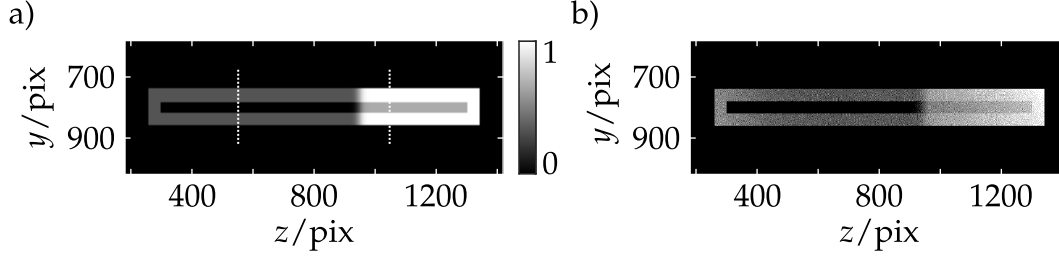


Figure 5.3: Example of a DMD image to imprint a phase. Part a) shows the desired intensity distribution for imprinting a phase jump at position z_{80} onto the BEC, normalized to the maximal intensity I_{\max} . Light with the intensity $0.67 I_{\max}$ is shone onto the atoms on the right part. The height of the box walls is $0.33 I_{\max}$ on the left and I_{\max} on the right. It is scaled accordingly to the background in order to minimize a change in trap frequency. The dashed lines show the leftmost and rightmost positions for imprinting a phase jump. The scale of the axes are the pixels of the DMD, i.e. the individual mirrors. Part b) shows the binarized image after incorporating effects of the inhomogeneous illumination and rounding the grey-scale image with the Floyd-Steinberg algorithm.

input by a continuous feature in the reservoir. Therefore, the position z_i of the phase jump associated with the input value x_i is calculated by

$$z_i = l \left(0.25 + 0.5 \left(\frac{x_i - \min_k x_k}{\max_k x_k - \min_k x_k} \right) \right), \quad (5.3)$$

where l is the size of the trap, and $\min_k x_k$ and $\max_k x_k$ are the minimal and maximal input value, respectively. This scales the input values to fit in the encoding region, which is the central half of the condensate.

The phase jump is imprinted by switching the image of the DMD from the flat box trap to a trap where one part is elevated. Figure 5.3 a) shows an example of the intensity profile for a phase jump at position z_{80} , corresponding to the input value $x_{80} = 1.79$. The dashed lines indicate the central region used for the encoding, which is 500 pix broad. The background intensity in the trap is modelled by a shifted error function of the form $I(z) \propto (0.5 + 0.5 \operatorname{erf}((z - z_i)/b))$. To avoid interference effects the width of the transition is chosen as $b = 16.7$ pix, corresponding to the integral over a Gaussian function with standard deviation $\sigma = 11.8$ pix. For a typical experiment, the DMD is illuminated with a total power of $P_{\text{DMD}} = 0.6$ W, which leads to some maximal intensity I_{\max} in the atomic plane. Atoms on the left of the phase

jump are not illuminated during the imprint. On the right, a light intensity of $0.67 I_{\max}$ is shone onto the atoms. The walls of the box trap are scaled accordingly, leading to an intensity of $0.33 I_{\max}$ on left side and I_{\max} on the right side of the phase jump. This is implemented to minimize a change of the radial trapping frequency. We estimate the light potential V_L experienced by the atoms on the right side of the transition to be

$$V_L = c_L \cdot 0.67 \cdot P_{\text{DMD}} \sim 7 \text{ kHz} , \quad (5.4)$$

where the calibration c_L is calculated in eq. (3.3). This light potential is present on the DMD for $t_L = 100 \mu\text{s}$, corresponding to the fastest switching time for images on the DMD compatible with the time steps of the experimental control system. Therefore, we can estimate the phase shift to be

$$\Delta\phi = (2\pi/h) V_L t_L \sim 1.4 \pi . \quad (5.5)$$

For our experiments, we use $N_x = 100$ input values which are evenly distributed in the input range. This leads to a spacing of 5 pix between adjacent input values on the DMD, corresponding to about $0.5 \mu\text{m}$ in the condensate.

5.2.2 Reservoir Evolution and Readout

After an input value is encoded via the structure of the phase as described before, the BEC is left to evolve in the flat box trap for a time t_{evo} and an absorption image of the resulting density distribution is taken. A single realization of the atomic cloud after an evolution of 1 ms is shown in the left panel of fig. 5.4 for the input value x_{80} . The single images are rotated using the MATLAB built-in function `imrotate`, such that they are aligned with the pixel grid for further analysis (top right panel). The rotation includes an interpolation of the data. However, possible errors can be neglected as many pixels are averaged together later in the analysis process. The atom cloud is cut out with a box of height $11 \mu\text{m}$ and length $82 \mu\text{m}$ to include the full width, but cut off the edges of the cloud. The cut-out is summed along the short axis and the resulting profile is normalized to minimize the effect of atom number fluctuations (top curve of lower right panel). Finally, the profile is binned, which significantly reduces the noise. This yields the binned density profile n_{80} plotted as the lower curve in the lower right panel of fig. 5.4. As the profile is multiplied with the weight vector w to get the output, the number of bins is directly connected to the number of parameters used in the training process,



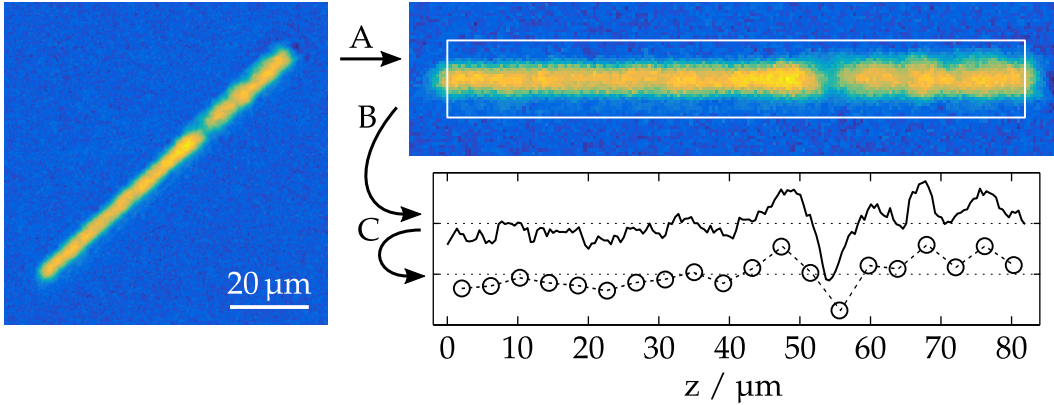


Figure 5.4: Data extraction. On the left, a single realization of the reservoir is shown for an evolution time $t_{\text{evo}} = 1$ ms. The image is rotated to align the atomic cloud with the pixel grid (A). Next, the atom cloud is cut out as indicated by the white box with size $11 \mu\text{m} \times 82 \mu\text{m}$. The edges of the cloud are removed to suppress fluctuations. The image is summed along the short axis and the resulting profile is normalized to the total atom number (B). The result is shown as the top curve in the lower right plot, and the dashed line gives the mean of the profile. Finally, the profile is binned according to the chosen number of output channels N_C , which we typically set to $N_C = 20$. The lower line in the plot gives the binned result (C).

which is the number of channels N_C . Typically, we use $N_C = 20$, which leads to a width of $4.1 \mu\text{m}$ per bin.

Figure 5.5 gives an overview of the time evolution. Each curve shows the mean over 30 realizations of the unbinned density profiles for the indicated evolution time. They are centred around their respective mean value (dashed line), share the same scale, and the standard deviation is given by the grey shaded area. One can see that a peak and a dip develop and evolve with time. The movement of the features can be understood from basic theory of superfluidity, where a gradient in the phase of the order parameter is proportional to the velocity of the fluid [52]. The features start to develop already during the imprint time, which makes sense when looking at the first $100 \mu\text{s}$ of evolution time ($0 \text{ ms} \rightarrow 0.1 \text{ ms}$). One can observe a fast evolution on this timescale, which is the same as the imprint time of $t_L = 100 \mu\text{s}$. On the right side of the density profiles fluctuations are present. They originate from an uneven light potential during the imprint phase that is caused by interference effects of the DMD light. These fluctuations do not move and

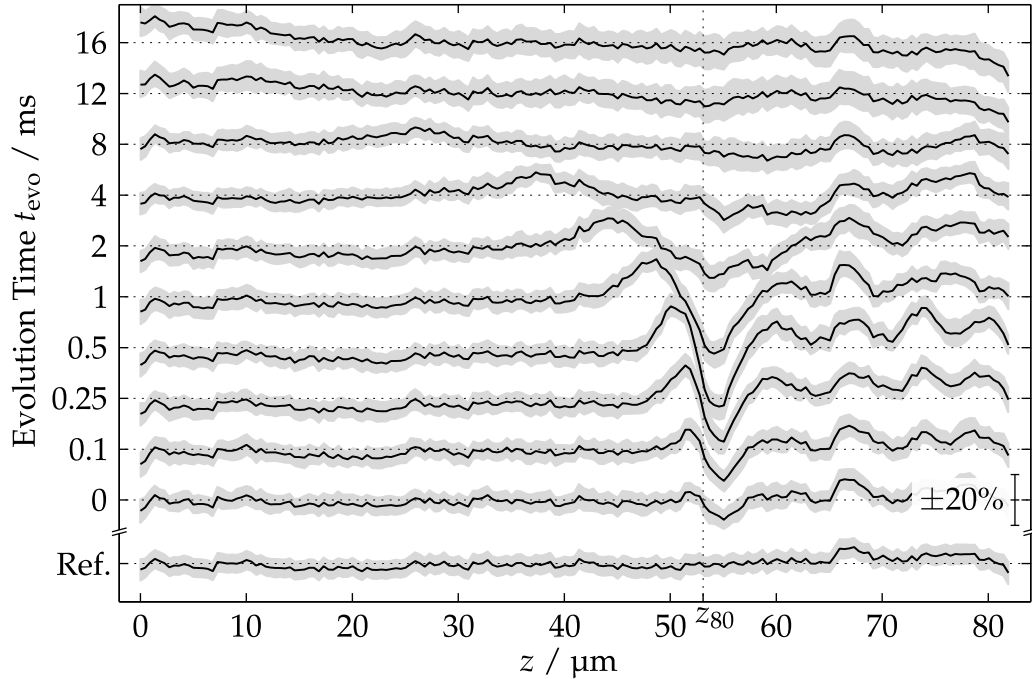


Figure 5.5: Normalized profiles of the atomic cloud. The plot shows the time evolution for a phase imprint on the right side with the transition at position z_{80} . The lowest curve depicts the profile without phase imprint as a reference. The curves above show the profiles for increasing evolution time, as indicated on the axis. All profiles are normalized to the total atom number before calculating the mean over 30 realizations. The resulting mean profiles are centred at their mean value (indicated with the dashed line) and the standard deviation is given by the shaded area. They share the same scale, and a deviation of $\pm 20\%$ from the mean is indicated. The evolution shows the development of a peak and a dip that move in opposite directions while getting broader. Furthermore, density fluctuations are imprinted on the profile where the cloud was illuminated.



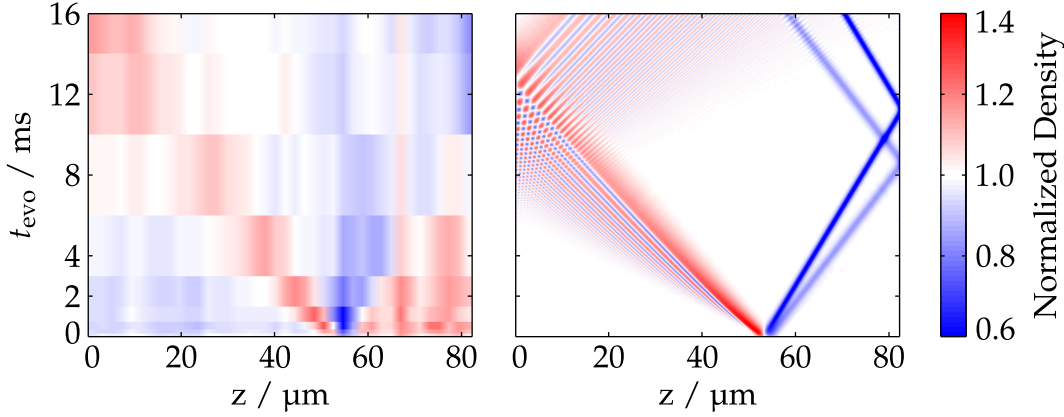


Figure 5.6: Time evolution in experiment and theory. The left panel shows the time evolution for the normalized atomic profiles after a phase imprint at position z_{80} . Each evolution time t_{evo} is represented by a bin reaching from midpoint to midpoint between adjacent times. The right panel shows a numerical simulation with the GPE that follows the same protocol as the experiment. Both plots show a broadening of the peak. The dip remains stable in the simulation but decays in experiment. We attribute this to the density fluctuations on the right side of the condensate.

decay with evolution time.

To gain a better understanding of the processes during the time evolution, we compare the experimental data to a simulation for the input value x_{80} , which is depicted in [fig. 5.6](#). The left panel shows the experimental results evaluated with $N_C = 40$ bins for a better spatial resolution. The evolution times are represented by bins that range from midpoint to midpoint between adjacent evolution times. The simulation shown in the right panel is carried out using the one-dimensional GPE to govern the dynamics (cf. [section 2.6](#)). It follows the same steps as the experiment. First, a ground state is prepared in a flat box trap, then a potential is switched on for the phase imprint and finally the atomic cloud is evolved in the flat box trap. We use the chemical potential estimated in [eq. \(3.2\)](#) and the imprint potential from [eq. \(5.4\)](#). The simulation is implemented using the split-step method with 1024 grid points and a time step of $0.1 \mu\text{s}$.

In the theoretical prediction, an over-density moves to the left and broadens, whereas under-densities travel to the right and keep their form. This behaviour can be understood from the theory of solitons [[111](#), [112](#)]. A density dip with a phase-jump on a continuous background with repulsive interac-

tions can form a stable, non-linear wave, which is called a dark soliton. They have no dispersion and their velocity decreases with increasing depth. In contrast, a density peak on such a background is not stable and will disperse as one can see in the theory results. A stable solution can only be obtained by exploiting attractive interactions [113].

In the experimental data a similar behaviour is observed for the over-density, which moves to the left and broadens. However, no solitonic excitations are observed and the under-density is dampened out rather quickly. This might result from the interaction with the density fluctuations introduced during the phase imprint on the right side of the phase jump. Such dissipative effects might affect the training and limit the accuracy of predictions for long evolution times (cf. section 5.3.1).

5.2.3 Training Procedure and Overfitting

The remaining building block is the calculation of the weight vector $w \in \mathbb{R}^{N_c}$, which we call training. As mentioned before, the output layer is simply a linear transformation. This means that for any input x_i with an associated binned density profile $n_i \in \mathbb{R}^{N_c}$ the corresponding output y_i is calculated by

$$y_i = n_i \cdot w . \quad (5.6)$$

This output should match the target output u_i . To fit the weight vector w , we minimize the root-mean-square (rms) error

$$\varepsilon = \sqrt{\frac{1}{N} \sum_k (n_k \cdot w - u_k)^2} \quad (5.7)$$

over N data points k . Typically, we use one profile corresponding to one experimental realization for every input value x_i for training, leading to $N = N_x$. This is not fixed, however, and one can use fewer data points which leads to a sparse training set. When evaluating the output corresponding to an input value not present in the training set the system has to interpolate between neighbouring data points (cf. section 5.3.4). On the other side, one could use multiple profiles for every input value x_i . As the readout from the physical system is always noisy this leads to an averaging effect and thus reduces the error. The minimal error ε is achieved by calculating the



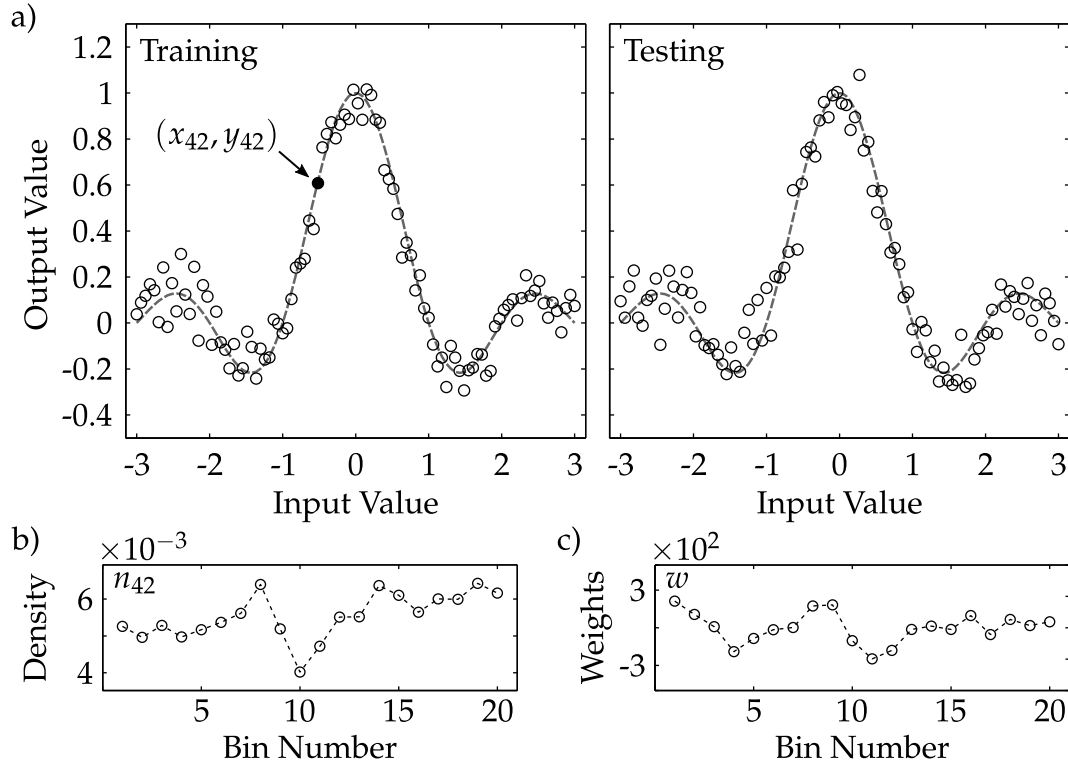


Figure 5.7: Training results for 1 ms evolution time. The top left panel shows the result for training a regression of $u(x) = \sin(\pi x)/(\pi x)$ (dashed line) to the data. Every point has an associated binned density profile, here exemplified for the input value x_{42} , and its binned density profile n_{42} is shown in part b). It is multiplied with the weight vector w (part c) to yield the output y_{42} . The weight vector w is the same for all inputs and calculated in the training procedure. The top right panel shows test data, where a new set of measurements of the density was used to calculate the results with the weight vector w trained beforehand. Both training and testing show that the regression can be performed well.

Moore-Penrose pseudo-inverse [114, 102] for the system of linear equations

$$\begin{pmatrix} - & n_1 & - \\ & \vdots & \\ - & n_N & - \end{pmatrix} \begin{pmatrix} | \\ w \\ | \end{pmatrix} = \begin{pmatrix} u_1 \\ \vdots \\ u_N \end{pmatrix}, \quad (5.8)$$

and leaves us with the best fit for the weight vector w . Alternatively, one can also use Ridge regression or logistic regression [115, 110], but we found the pseudo-inverse to be sufficient.

The result is shown in [fig. 5.7](#) for our target function $u(x) = \sin(\pi x)/(\pi x)$. The left plot of part a) depicts the regression for 1 ms evolution time of the reservoir. The data points show the calculated outputs y_i to each input x_i for all N_x training points, and the target function is plotted with a dashed line. One can see that the data points agree very well with the target function. The calculation of the output values is shown below for the input value x_{42} . Part b) gives the binned density profile n_{42} that is read out from the experiment. It is multiplied with the weight vector w shown in part c) to yield the output y_{42} . The weight vector w is determined by the pseudo-inverse as described above.

To demonstrate that the regression works properly, the right plot of part a) shows results obtained with different realizations of density profiles \tilde{n}_i for each input value x_i while the weight vector w is kept from the training. For these new test profiles \tilde{n}_i the data points show a very good agreement with the target values as well. This indicates that our implementation of physical computing works, and a weight vector can be successfully trained to fit a non-linear function. More quantitative results are given in the following section.

The last step, in which we validated the fitted weight vector w with an independent test data set, is particularly important to spot potential overfitting. This occurs, for example, if one uses too many output channels N_C , i.e. fit parameters, compared to the number of training points. As our density profiles are noisy, these small variations can be exploited by the fit to discriminate the different density profiles n_i if there are enough free parameters. Then, an independent test data set would not fit the target function well, as its noise is different.

We illustrate this by sabotaging the procedure and using reference profiles for the input profiles n_i . These are obtained before the phase imprint and therefore completely uncorrelated to their input value x_i . However, as the upper row of [fig. 5.8](#) shows, a fit becomes possible by increasing the number of output channels N_C , i.e. fit parameters in the weight vector w . Already



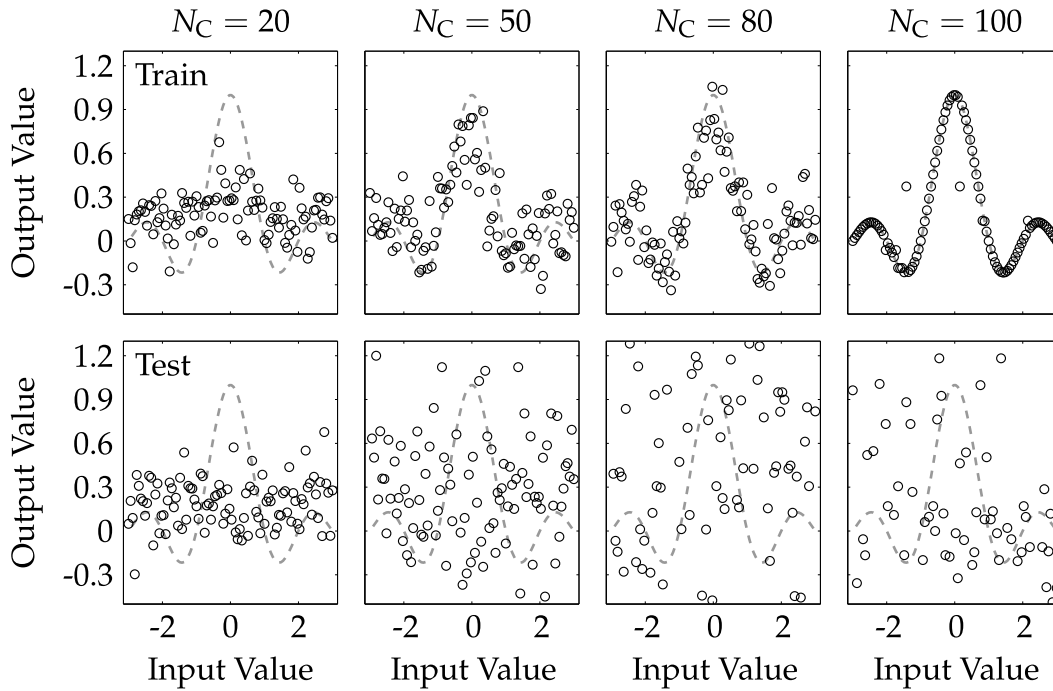


Figure 5.8: Overfitting using reference profiles. The top four plots show the result of training a regression where reference profiles were used for each input value ($N = 100$). They are completely uncorrelated to the input as they are obtained before the phase imprint. However, by increasing the number of channels N_C and hence the number of fitting parameters in the weight vector w a regression to the target function (dashed line) seems possible. Testing the obtained weight vector w with a different set of inputs reveals that no prediction can be made and the results stem from overfitting (lower row).

for $N_C = 50$ the data points start to follow the target function. Maximal overfitting occurs when the number of training points equals the number of channels N_C . If all input profiles are linearly independent eq. (5.8) becomes invertible and the data points follow the target perfectly. In this example, few profiles are linearly dependent, and therefore some points do not match the target. When we test the obtained weight vector w with a different set of profiles \tilde{n}_i , the data points do not fit the target function (fig. 5.8, lower row). No prediction is possible, and the overfitting of the model is directly visible.

5.3 Experimental Results

The first qualitative results for the regression task of a non-linear function have been shown in the last section. In this section we give a more quantitative analysis, looking at the rms error for different evolution times and the influence of noise. Furthermore, the onset of overfitting and an interpolation task is investigated.

So far we applied our physical computing framework to fit the non-linear function $u(x) = \sin(\pi x)/(\pi x)$ at $N_x = 100$ input values using one realization of the reservoir per input value for training. To gain statistics, we use a method inspired by bootstrap resampling [116]. For every input value x_i we measure N_R different density profiles $n_{i,k}$. We then compile a set of density profiles $\mathcal{N}_{\text{Train}}$ by randomly choosing one of the realizations $k_i = 1 \dots N_R$ for every input value x_i ,

$$\mathcal{N}_{\text{Train}} = \{n_{1,k_1} \dots n_{100,k_{100}}\} . \quad (5.9)$$

For this set of reservoir realizations the training is applied to obtain the weight vector w . We then calculate the rms error ε for the training set according to eq. (5.7) to judge the quality of the regression. Next, a testing set $\mathcal{N}_{\text{Test}}$ is put together the same way as the training set $\mathcal{N}_{\text{Train}}$, but using only density profiles $n_{i,k} \notin \mathcal{N}_{\text{Train}}$. Then, the rms error ε is calculated for the testing set $\mathcal{N}_{\text{Test}}$. The whole process is repeated 25 times, and mean and standard deviation of the rms error are estimated. This way we can generate statistical statements from a limited number of experimental realizations.

5.3.1 Evolution Times

First, we investigate the quality of the regression for different evolution times of the reservoir, using $N_C = 20$ output channels. The profiles $n_i = n_i(t_{\text{evo}})$ evolve in a non-linear manner and show dissipative behaviour (cf. section 5.2.2). Hence, the resulting rms error ε also depends on the evolution time t_{evo} and is plotted in fig. 5.9 for training and testing data sets. The dashed and dotted lines at the top of the plot indicate a sensible upper error bound for training and testing, respectively. They originate from calculating the rms error for training with reference profiles for $N_C = 20$ output channels as shown in fig. 5.8. These profiles do not contain any information, and the error is similar to the rms deviation of the target function to its mean. One can see that the regression for the non-evolved reservoir yields already



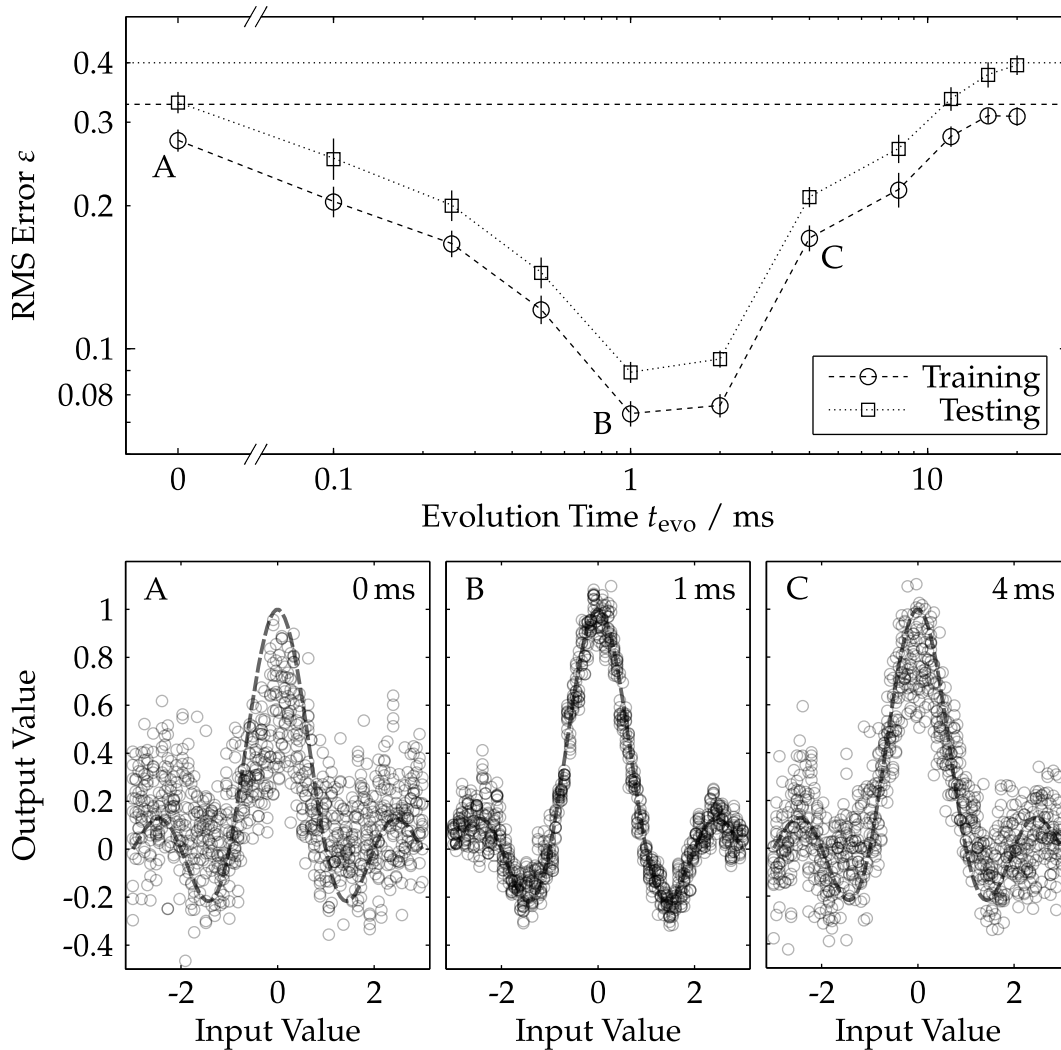


Figure 5.9: Development of the error with evolution time of the reservoir. The upper panel shows the rms error for training and testing data sets (circles and squares, respectively). It is calculated in a bootstrap resampling fashion as explained in the main text, $N_C = 20$ output channels are used. The straight lines at the top of the plot indicate the error that results from using reference profiles without any information on the input values for training (dashed line) and testing (dotted line). The error is lowest for an evolution time of 1 ms and the results of the testing data sets imply that the regression works properly. Examples of the regression are shown in the lower panel for evolution times 0 ms, 1 ms and 4 ms, where the training data for 10 sets of realizations composed in the bootstrap resampling fashion is shown by the grey transparent points. The target function is indicated with the dashed line.

better results than the error bound. Looking back at the density profiles in [fig. 5.5](#) this becomes clear since the condensate starts to evolve during the imprint duration t_L and shows a small feature at $t_{\text{evo}} = 0$ ms. With increasing evolution time the error decreases and reaches a minimum at $t_{\text{evo}} = 1$ ms. This behaviour can be understood from the evolution of the profiles (cf. [fig. 5.5](#)), where the density features resulting from the phase imprint have to develop first and stretch over multiple bins to be of use in the training process. With further evolution, the features broaden and become weaker compared to the noise. Therefore, the error increases for longer evolution times. The testing error is slightly above the training error for most times, which indicates that the regression works well.

To give a better intuitive understanding of the rms error ε , the lower panel of [fig. 5.9](#) directly compares the regression results without evolution (A), for minimal error at $t_{\text{evo}} = 1$ ms (B), and for a longer evolution $t_{\text{evo}} = 4$ ms (C). The training results for ten different sets of density profiles $\mathcal{N}_{\text{Train}}$ are overlapped to give a visual impression of the statistics. The central plot (B) shows that the data points agree well with the target function (dashed line). In comparison, the data points deviate if no evolution is performed (A) or noise effects become more relevant (C).

5.3.2 Averaged Density Profiles

We investigate the influence of noise for longer evolution times more closely by using averaged density profiles n_i^{avg} for the training,

$$n_i^{\text{avg}} = \frac{1}{N_R} \sum_{k=1}^{N_R} n_{i,k}, \quad (5.10)$$

where N_R is the number of realizations. We calculate the rms error ε for different N_R using $N_C = 20$ output channels, and we only consider the training error as the testing error behaves well (see [fig. 5.9](#)). The result is shown in [fig. 5.10](#) for the evolution times $t_{\text{evo}} = 1$ ms, 4 ms, and 8 ms. The error decreases with the number of realizations N_R used to calculate the averaged density profile n_i^{avg} . A power-law behaviour can be observed, which results in straight lines in the double-logarithmic plot. We fit the data points by

$$\varepsilon \propto N_R^{-\zeta}, \quad (5.11)$$

with the scaling exponent ζ . For the evolution time $t_{\text{evo}} = 1$ ms we find an exponent of $\zeta_1 = 0.38$. This indicates that the realizations of the density



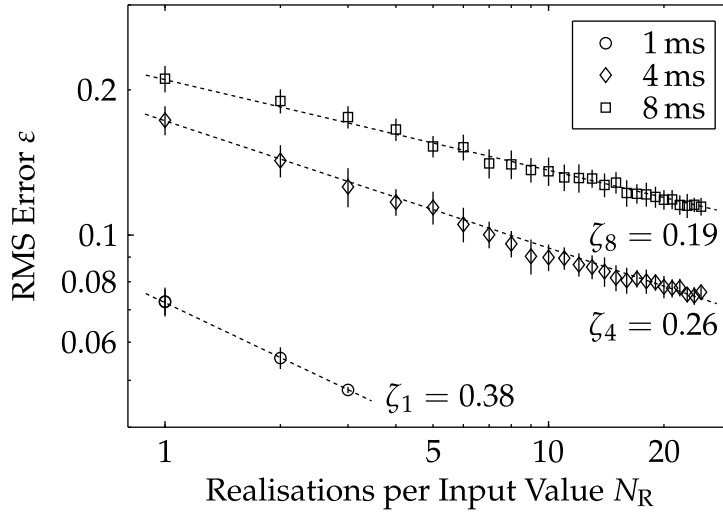


Figure 5.10: Suppression of noise using averaged density profiles. The rms training error ε is shown using averaged density profiles for three different evolution times. For each input value x_i the associated density profile n_i is calculated as the mean of N_R realizations of the profile. The error bars are estimated in the bootstrap resampling fashion described in the main text. When the number of realizations is increased shot noise averages out and the regression works better. The decrease of the error is fitted by a power-law curve, $\varepsilon \propto N_R^{-\zeta}$. The flattening of the curves for longer evolution implies that information is lost or redistributed during the evolution.

profiles differ not only by uncorrelated shot noise, where we would expect scaling with the square-root ($\zeta = 0.5$), but contain systematic deviations. With increasing evolution times the scaling exponent decreases. We thus conclude that information is lost or redistributed during the evolution, which can not be recovered by averaging an acceptable amount of profiles to suppress noise. This fits the observation presented in [fig. 5.6](#), where density fluctuations from the phase imprint disturb the dynamics. However, averaging is a legitimate strategy to improve the quality of the regression even further and works especially well for evolution times that give good results in the first place.

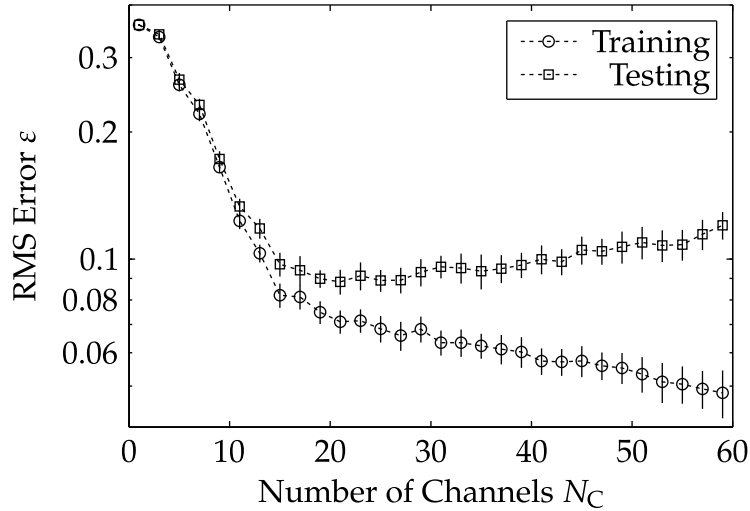


Figure 5.11: Dependence of training and testing error on the number of channels. The graph shows the dependence of the rms error ϵ for training (circles) and testing sets (squares) on the number of output channels N_C . The values are calculated in a bootstrap resampling fashion as described in the main text. For increasing N_C the error for both training and testing decreases at first. The testing error reaches a minimum at about $N_C = 20$. This is the onset of overfitting, where the testing error starts to increase again even though the training error continues to decrease.

5.3.3 Avoid Overfitting

So far, the analysis was done with a fixed number of channels, $N_C = 20$, as we claimed this works best. To illustrate what can go wrong we calculate the rms error ϵ for training and testing sets for increasing N_C . The results are shown in [fig. 5.11](#) for a fixed evolution time $t_{\text{evo}} = 1$ ms with a single realization n_i of the reservoir per input value x_i . One can see that the error drops at first with increasing N_C for both training and testing data sets. The error for the training continues to decrease, while the error for the testing features a minimum around $N_C = 20$. This is known as the bias-variance trade-off in machine learning [117]. By increasing the number of channels N_C , and therefore the number of fitting parameters, we enter the regime of overfitting. The lower error for the training arises only from fitting the excess parameters to noise features that are not present in the testing sets. We find this behaviour to be robust against sensible changes of the number of training points. Setting $N_C = 20$ for our analysis is thus a good choice.



5.3.4 Generalization

In this section we look at the performance of the system on input values that are not part of the training data set to check the system's ability of generalization. Previously, the $N_x = 100$ input values were chosen to be equally spaced in the range $[-3, 3]$. For the experiments presented in this section we leave out 20 data points and compile a training set $\mathcal{N}_{\text{Train}}$ from the density profiles of the remaining 80 data points. Single profiles with $N_C = 20$ after an evolution time of $t_{\text{evo}} = 1$ ms are used. We estimate the outputs for the 20 left-over input values by multiplying the density profiles with the obtained weight vector. This approach demonstrates the capabilities of the system to interpolate between the training data points.

Figure 5.12 a)-c) presents the generalization results, where each left plot shows the outcomes of the training process with $N = 80$ data points. Each right plot depicts the results for data points not included in the training process, and it is thus a measure for the interpolation capabilities of the system. In part a), the points to be removed are chosen randomly, in part b) on the rising edge left to the maximum, and in part c) left and right to the maximum. Each plot shows ten sets of realizations to illustrate the spread of the data. A quantitative analysis is given in part d), where the rms error ε is given for training and interpolation (estimated from 25 sets of realizations in the bootstrap resampling fashion). As a reference the training and test error for a regression with $N = 80$ data points is included.

One can see in part a) that the interpolation works well when omitting few points at any position, and the interpolated points lie close to the target function. Consistently, the rms error ε is equal to the reference obtained from the regression within the error bounds. To increase the complexity of the problem, we leave out the rising edge on the left to the central maximum for training (part b), and we get a training error ε similar to the reference error. The interpolation seems to work good for most input values, but the error is significantly higher and has a high variance. We attribute this mainly to the data points close to the local minimum at an input value of $x \sim -1$, where a large fluctuation can be observed. Leaving out the central maximum for the training procedure (part d) limits the interpolation capabilities, which is expected as no information about the structure of the maximum is known to the training procedure. However, the system interpolates smoothly between the two regions similar to the previous task and the form resembles the maximum qualitatively. As the data points deviate significantly from the target function in absolute values, a large error is obtained. These results show

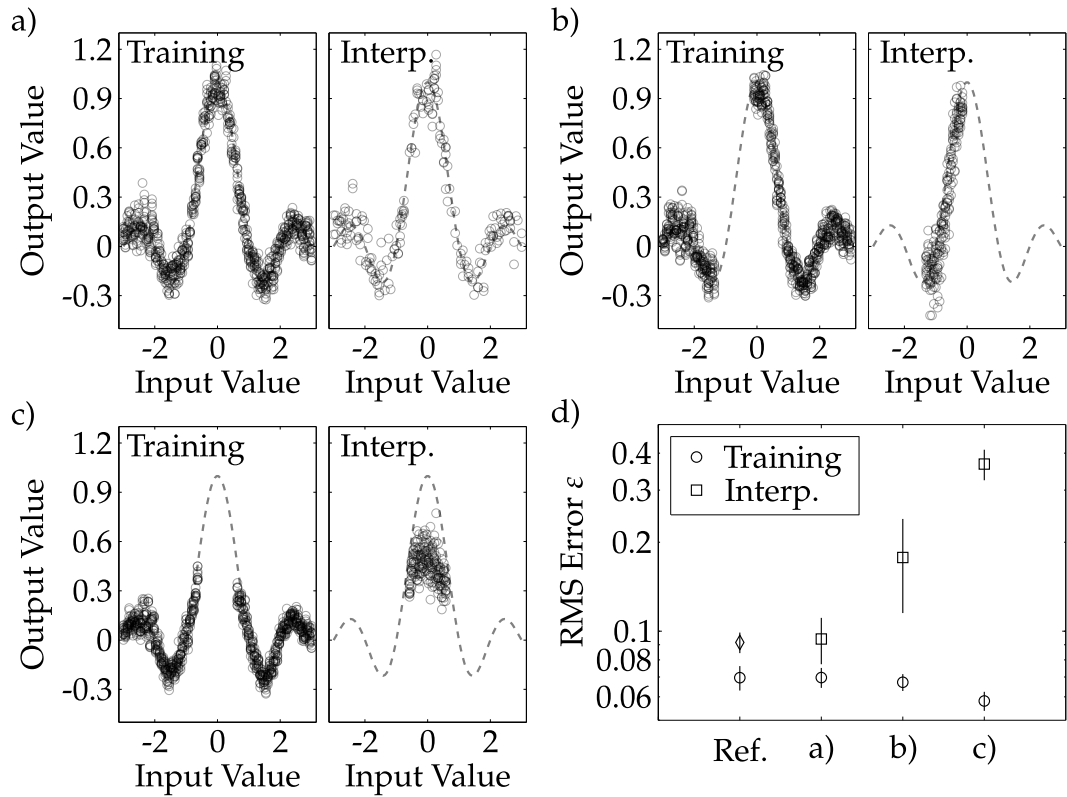


Figure 5.12: Generalization. The figure shows a strategy to test the ability of the system to interpolate between data points. We remove 20 data points from the training set and train the weight vector w on the left-over $N = 80$ points (left plots). For the remaining 20 data points the output value is calculated with the obtained weight vector (right plots). Parts a) to c) illustrate three scenarios, where ten sets of realizations are shown and the target function $u(x)$ is given by the dashed line. In part a) the data points for training are chosen randomly, in part b) they are chosen to leave out the rising edge on the left of the central maximum, and in part c) the central maximum is left out. Part d) shows the resulting rms error ϵ for the different cases. The values are calculated in the bootstrap resampling fashion. As a reference (Ref.) the training and testing error for the regression task with $N = 80$ training points is shown by the circle and diamond, respectively. Part a) gives very good results and the rms errors are similar. The interpolation of the gap in part b) works well, but the rms error is significantly higher than the reference. This is attributed mainly to fluctuations close to the minimum at $x \sim -1$. Omitting the central maximum in part c) for training, the interpolation behaves reasonable and connects the two parts smoothly. The data points deviate significantly from the target, which leads to a large rms error.



that the system is capable of interpolation and behaves well even for large gaps in the training data.

5.4 Discussion

We have shown that a quasi one-dimensional BEC can be used with our implementation of physical computing. The regression and interpolation of a non-linear function was performed as a first task. We investigated the quality of the regression for different evolution times and the effects of noise. The analysis demonstrates that the system behaves well and sensible results can be obtained. In the following, we first revisit the prerequisites for a reservoir and discuss that our physical implementation satisfies them. We then show the limitations of our implementation and discuss possible extensions.

Reservoir Our implementation of physical computing uses a quasi one-dimensional BEC on which we imprint input data by a change of the phase. The system itself has only one spatial dimension, but the feature space is spanned by the values the density distribution takes along this direction and the number of spatial points. This makes the system high dimensional, which is the first prerequisite for a reservoir as discussed in [section 5.1](#). We deliberately reduce the feature space to $N_C = 20$ output channels to avoid overfitting. Two more prerequisites are met, as the system features non-linear dynamics (cf. [fig. 5.5](#)) and it separates the inputs by a non-linear evolution (cf. [fig. 5.9](#)). The fourth, the property of fading memory, is not tested directly as we consider non-temporal tasks. However, we showed that the error of the regression task increases again after some evolution time (cf. [fig. 5.9](#)) and we observe a loss of information for long evolution times (cf. [fig. 5.10](#)). We can thus conclude that the system has a fading memory and fulfils the prerequisites for a reservoir. It should be able to solve temporal tasks as well, which is an interesting direction for further investigation.

Further Investigations In our current implementation the non-temporal task is limited to one input and one output dimension. This is no fundamental limit as the shape of the trap and the phase imprint are easily configurable with the DMD. To implement a non-temporal target function with more than one input dimension we do not need to change our approach much, as we could imprint multiple phase jumps. The same phase difference could be used at each position, or different shifts could be chosen by applying a matching

potential. In this context it would be particularly interesting to look closer into the interaction of the resulting density features and its consequences for learning. Increasing the number of output dimensions could be implemented by changing the weight vector w to a matrix. Then, multiple outputs can be calculated from one density profile n_i by effectively computing one weight vector per output dimension.

For a more complex target function it might be favourable to increase the capacity of the reservoir and encode more than $N_x = 100$ input values. This can be achieved by small changes of the encoding that are explained in the following. A total increase by a factor of 5–10 should be possible before reaching the technical limit of the implementation. By imprinting the phase jump closer to the edges of the trap we could gain at least a factor 2. For this estimation, we choose a distance of $5\ \mu\text{m}$ from the trap walls such that the resulting features are not reflected on the edge of the trap for an evolution time of $t_{\text{evo}} = 1\ \text{ms}$. Furthermore, the spacing between the input values on the DMD can be reduced. For our experiments we used a spacing of $x_{i+1} - x_i = 5\ \text{pix}$. Although single pixels of the DMD are below the resolution of the imaging optics (cf. [section 3.5](#)), the evolution of the reservoir could still reveal small shifts of few pixels. This has to be investigated in the experiment and a further factor of 5 in N_x can be reached at most. With more input values N_x at hand it is interesting to revisit the task of interpolation and check the capabilities of our system. Furthermore, the conditions for overfitting can be investigated better by having more data points available for training.

Another parameter to be investigated is the height of the phase jump. We always use the same phase difference in the experiments presented. However, it could be adapted with the DMD and should influence the non-linear response of our system. Further research on its influence on the quality of learning would be interesting and allow for a better understanding of the processes.

Technical Challenges On the technical side it would be beneficial to reduce the fluctuations introduced during the imprint of the phase. So far we used a rather simple approach to flatten the density profile by correcting the intensity along the cloud (cf. [section 3.5](#)). The same factors are used to correct the background potential which we apply during the phase imprint. However, switching on more mirrors introduces further interference patterns. These might lead to fluctuations in the density of the atom cloud and enhance dissipation and heating. To eliminate these effects all different configurations of



the DMD have to be calibrated carefully [118]. To reduce density fluctuations it would be beneficial to imprint the phase in a shorter time with a higher potential. We can change the image displayed by the DMD every 70 μs at most. To reach significantly shorter imprint times, a second DMD setup would be necessary, and the light needs to be switched with a fast external device, such as an AOM. This approach is useful in many ways, as interference effects of the light used for trapping and background potential could be separated. Furthermore, one could use a different frequency of light on the second DMD. With a frequency closer to the resonance a higher potential difference can be achieved. Another technical challenge is the repetition rate of the experiment. A typical run takes about 20 s and it is a limiting factor to gain statistics. For one-dimensional systems this could be improved by preparing multiple systems simultaneously.

Other Implementations Apart from these small modifications, different implementations of physical computing could be tested without major changes on the setup due to the configurable nature of the lateral trap. It is possible, for example, to extend the physical system and use a two-dimensional atomic cloud as feature space. This allows for a quadratic increase of possible inputs and more complex dynamics. However, the encoding we used can not be transferred to this system in a straight-forward manner. Different physical phenomena, such as vortices, could be exploited. Depending on the tasks the system has to solve, one has to take care that the implementations reflect the properties of the input features, for example continuity. A different approach would be the direct encoding of grey scale images as a dipole potential on the atomic cloud, and classification of such images might be investigated in future studies.

Another interesting direction is the investigation of temporal tasks, which could for example be implemented by consecutive inputs to the system or by an encoding of the temporal domain (partly) in space. As discussed above, these tasks might provide insights in the ability of the system to retain information and allow for a quantitative analysis. In addition, the potential loss or the redistribution of information in the system is by itself an exciting topic.

Very recently the first training of physical systems with the help of back-propagation has been demonstrated [119]. The procedure enables the training of deep physical neural networks with multiple layers. This could be a promising path as the construction of deep networks led to significant improvements

for conventional neural networks implemented with digital computers.

A distinctive feature of our reservoir are its inherent quantum properties. While the experiments presented in this thesis take place in a regime predominantly governed by classical dynamics of a macroscopic quantum-mechanical “wavefunction”, the access to “truly quantum” features might be as direct as the implementation of an advanced imaging technique [120] or the extension to a spinful system [121]. The presented framework for physical computing is versatile, and it is possible to choose implementations that include quantum processes. This might lead to new insights and help to understand quantum computing in a continuous system.



CHAPTER 6

Final Remarks

This thesis presented the experimental setup to prepare a BEC of ^{39}K , to control its interactions and shape, and a strategy for imaging. Furthermore, a shallow neural network was implemented using a quasi one-dimensional atomic cloud and the learning process is investigated for different experimental parameters. This chapter concludes the topics discussed and gives prospects for experimental upgrades and future projects.

6.1 Conclusion

The first chapters of this thesis give an overview of the components of the experimental setup, which has been developed and put together over the last few years. The different systems are optimized for stable operation, and the setup is automated to run continuously. With the high stability of the experiment this allows for measurement campaigns over many days.

A detailed description of the control setup for the magnetic coils is given. It drives a single pair of coils which can create a quadrupole field or a homogeneous field with an additional gradient in gravity direction. The control setup shows a high stability, and fluctuations of the magnetic field are estimated to be below 0.5 G at the typical Feshbach field of 550 G.

To trap the atomic cloud in two dimensions and control its shape, a configurable dipole potential was implemented with a DMD. For this thesis, the setup is utilized to prepare a quasi one-dimensional BEC. In other experiments the setup was also used to form square and circular box potentials, or more

complex ones like a potential that features a density minimum in the centre [122].

The imaging system of the experiment is discussed in detail and a scheme for absorption imaging at high magnetic fields is presented. This scheme is necessary to properly exploit tuning of the atomic interaction, and it obtains a high absorption signal of the atomic cloud immediately after the experiments are performed. It uses two transitions to form an approximately closed four-level system, and we find the best results for equal imaging intensities on both transitions. The scheme can be calibrated similar to an effective two-level system and experiments confirm that the calibration is robust against small variations of the imaging intensities. On the technical side, the objectives applied in the imaging setup are characterized, and the mechanical mounting system for the ProEM objectives above and below the science cell is presented. The MOT and grey molasses stages are successfully performed with two out of the six beams passing through the objective. This setup allows for large optical access and it shows high passive stability.

The second part of this thesis introduces physical computing and presents the physical implementation of a shallow network utilizing a Bose-Einstein condensate. As a proof-of-concept the regression and interpolation of the non-linear function $u(x) = \sin(\pi x)/(\pi x)$ are performed. Values are encoded in the physical system by the imprint of a phase, the system undergoes a free evolution and is subsequently read out by absorption imaging. Results can be obtained using single experimental realizations, and the lowest error is reached for an evolution time of 1 ms. Further parameters are investigated and the loss of information for long evolution times is observed. These promising results pave the way for further investigations of the topic.

6.2 Outlook

On the technical side a next step is to further improve the stabilization of the magnetic field. At the typical magnetic field for interaction tuning around 550 G the control setup reaches a stability better than 10^{-4} , which is mostly limited by the stability of the control voltage. To regulate the magnetic field over a wide range, a change of 10 mV in control voltage corresponds to a change of about 1 G in the magnetic field, and thus small fluctuations can have significant influence. To improve the setup, the implementation of a stable reference voltage at the control circuit is planned, which can be used as an input when working at high magnetic fields.



Improvements and prospects for physical computing are discussed in detail in [section 5.4](#), and the following paragraphs give a short overview. The experiments show that the potentials generated with the DMD lead to a flat density distribution on large scales, but persistent patterns on small scales on the order of few micrometers are observed. This can be improved by optimizing the correction factor on those scales (cf. [fig. 3.12](#)) or more advanced optimization methods for the DMD masks (see for example [118]).

Imprinting a phase with the DMD leads to fluctuations of the atomic density in the region where the light is flashed on (cf. [fig. 5.6](#)). This effect could be reduced if the flatness of the atomic cloud is improved at small scales. Greater advantages are expected from the implementation of a second DMD that is switched independently. It can use light of a frequency closer to the atomic resonance, which allows for a shorter light pulse. This gives the atoms less time to move in the dipole potential. Furthermore, it could minimize noise on the dipole potential that originates from interference effects.

On the scientific side it would be interesting to test the limits of the presented implementation. The physical limits can be investigated by encoding the input values more dense on the quasi one-dimensional system. To test the capabilities for information processing a wider range of input values can be used for the regression task. Another promising direction is studying the dynamic behaviour of the reservoir, as it was observed that the system seems to dissipate information (cf. [fig. 5.10](#)). This can be investigated in more detail with the implementation of a temporal task, which might also give insight to the memory capabilities of the system.

In general, physical computing is a versatile concept and not fixed to our implementation or our choice of encoding. The experimental system presented in this thesis allows the preparation of a BEC in two dimensions, which opens up many possibilities and might provide a rich feature space. Furthermore, the study of encoding methods that involve quantum processes might lead to new methods for quantum computing with BECs, and take the concept of physical computing to a new level.



Refocussing with Secondary Lens

As we discussed in [section 4.3](#) the secondary lens of the ProEM imaging system is mounted on a linear stage to allow for minor adjustments of the focus. To gain quantitative understanding of the connection between shifts of objective and secondary lens, we approximate our system using ray optics and a 4f-setup which is shown in [fig. A.1 a\)](#). The two lenses have focal lengths of f_a and f_b , respectively, and the distances are initially $z_{1/2} = f_a$ and $z_{3/4} = f_b$. We keep the total distance D between the object plane on the left and imaging

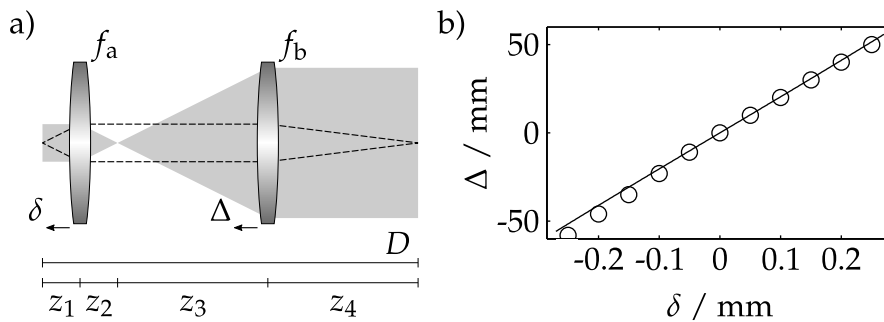


Figure A.1: Refocussing with secondary lens. Part a) shows the model system, where two lenses with focal length f_a and f_b are arranged in a 4f-setup initially. Shifting the first lens by a small distance δ we estimate with the lens formula which distance Δ the second lens has to be shifted such that the image is focussed again after a distance D . Part b) shows experimental results (circles) and theoretical (line) for a test setup with the ProEM objective and an $f_b = 500$ mm secondary lens.

plane on the right fixed. When the left lens is shifted by a small distance δ the distances $z_{1/2}$ between object and lens, and lens and intermediate image are altered according to the lens equation,

$$z_1 = f_a - \delta, \quad z_2 = \frac{z_1 f_a}{z_1 - f_a} = \frac{\delta f_a - f_a^2}{\delta}. \quad (\text{A.1})$$

Similarly, the shifts of the distances $z_{3/4}$ can be estimated and requiring D to be equal to the sum of the distances z_i we get the equation,

$$0 = \Delta^2 + \Delta \left(2f_a + 2f_b - D - \delta - f_a^2 / \delta \right) + f_b^2, \quad (\text{A.2})$$

which can be solved for Δ .

In a test setup with the ProEM objective ($f_a = f_{\text{eff}} = 35$ mm) and a secondary lens with $f_b = 500$ mm we carried out the refocussing, and the results are presented in [fig. A.1 b](#)). The theoretical prediction is close to a linear curve for small shifts δ on the order of $100 \mu\text{m}$ and matches the experimental data well. We can fit a linear curve, $\Delta = m\delta$ and get

$$m = 205 \quad \text{for } f_b = 500 \text{ mm}, \quad (\text{A.3})$$

$$m = 838 \quad \text{for } f_b = 1000 \text{ mm}, \quad (\text{A.4})$$

for the slope.



Lists of Components

The following chapter serves as a reference for components used in the experimental setup, giving details such as the manufacturer and part numbers.

B.1 Vacuum Setup and Experimental Control

Glass Cell The glass cell of the setup is manufactured from uncoated SPECTROSIL 2000, which has a refractive index of $n = 1.4535$ at a wavelength of 767 nm. The glass is 4 mm thick, and the inner/outer side length of the quadratic profile is 30 mm and 38 mm, respectively.

Experimental Control System The interface of the experiment with the computer control is established by National Instruments control cards. The single channels are broken out to BNC connectors and subsequently distributed to the experiment.

Table B.1: Interface cards.

Component	Manufacturer	Part Number
Analog Output Module	National Instruments	PXI-6733
Digital/Analog Input/Output Module	National Instruments	PXI-6254

B.2 Laser Setup

Resonant Light The resonant light is generated by DL-Pro external cavity diode lasers. We used them with different anti-reflection coated laser diodes and found that L1 works well at wavelengths of 767 nm and 770 nm. We found diode L2 to be difficult to work with at 767 nm, and it was sometimes hard to get good output power while maintaining a single mode. The diode L3 works good for us at wavelengths of 767 nm and we achieved slightly more output power than with diode L1.

To amplify the laser power we use home-built tapered amplifier units [68]. For laser shutters we use either a razorblade, which is attached to the moving switch of a relay, or a 3d printed design similar to [123]. A comprehensive overview of the laser setup with detailed schematics of the optical setup is given in [35].

Table B.2: Resonant Light Setup.

Component	Manufacturer	Part Number
ECDL	Toptica	DL-Pro
Laser diode (L1)	Toptica	LD-0790-0120-AR-2
Laser diode (L2)	Toptica	LD-0760-0080-AR-2
Laser diode (L3)	Toptica	LD-0780-0080-AR-4
Rf amplifier	Mini-Circuits	ZHL-3A+
AOM	Gooch and Housego	AOMO 3110-120 (110 MHz)
Tunable bandpass	Semrock	TBP01-790/12
Fast photodiode	Thorlabs	DET025AFC/M

Off-resonant light The experiment utilizes off-resonant light at 1064 nm and 532 nm. Comprehensive sketches of the optical setup can be found in [35].

For the green light we use special photonic crystal fibres that allow to carry high intensities while maintaining a single mode and the polarization. A special in-coupler is used that leaved the core open on the first few centimetres and allows light to escape that is not coupled in the fibre properly, thus reducing the risk of burning the fibre tip and the cladding.

The green light is shaped with a DMD from Texas Instrument. It is bought from Vialux with a control board that interfaces the DMD with the computer. It has a resolution of 2560×1600 mirrors, the individual mirrors have a side length of $7.6 \mu\text{m}$ and the whole chip hence a size of $19.4 \times 12.1 \text{ mm}^2$.



Table B.3: Off-resonant Light Setup.

Component	Manufacturer	Part Number
Laser 1064 nm	Coherent	Mephisto MOPA 55 W
AOM	Gooch and Housego	AOMO 3080-199 (80 MHz)
DMD	TI / Vialux	DLP9000X
High-power fibre	Schäfter-Kirchhoff	PMC-E-980-8.5-NA009-3-APC.EC-500-P
Fibre coupler	Schäfter-Kirchhoff	60FC-4-M15-37
Laser 532 nm	Coherent	Verdi V10
AOM	Gooch and Housego	3080-1916 (80 MHz)
High-power fibre	NKT Photonics	LMA-PM-10 (ends: SMA-905 and FC/APC)
Fibre in-coupler	Schäfter-Kirchhoff	60FC-SMA-T-23-A18-01
Fibre out-coupler	Schäfter-Kirchhoff	60FC-4-M10-01
Photodiode	Osram	SFH 206 K
Rf switch	Mini-Circuits	ZASWA-2-50DRA+
Rf amplifier	Mini-Circuits	ZHL-1-2W+

B.3 Experimental Setup at Science Chamber

Objective Holder The holder was manufactured by the workshop of the institute. Technical drawings can be found in [section D.4](#). Additional parts are listed in the table below.

Table B.4: Commercial parts of the objective holder.

Component	Manufacturer	Part Number
Micrometer heads: tip/tilt	Thorlabs	DM10
Micrometer heads: translation	Mitotuyo	148-142
Springs	Gutekunst Federn	RZ051MI
Supporting spheres	Kugel-Winnie	Zirkonoxid, 10.000 mm

Cameras The cameras used for our experiment are listed in the following table with specification of chip size and edge length of the individual pixels. More information on the imaging setup can be found in [section 4.2](#)

Table B.5: Cameras used at the experiment.

Component	Manufacturer / Part	Specs
Guppy	Allied Vision, Guppy F046B	780x582 pix, 8.3 μm size
Guppy Pro	Allied Vision, Guppy Pro 125B	1280x960 pix, 3.75 μm size
Pixis	Princeton Instruments, Pixis BR1024	1024x1024 pix, 13 μm size
ProEM	Princeton Instruments, ProEM-HS 1024B eXelon	1024x1024 pix, 13 μm size



Imaging Setup The following table lists the parts utilized for the imaging setups. The camera shutter is used for the ProEM imaging and the Pixis imaging setup.

To move parts of the MOT setup we use two pressure stages that allow for linear translation. The stage has two end points which can be set with a screw and it shows high repeat accuracy for the end positions. It contains two magnets at the pistons for position sensing which we removed. The cylinder can be opened and one can break off the magnets from the piston without damaging it. A few parts of the stage like the linear rail and screws are magnetizable. For one stage we swapped the linear rail with a plastic replacement, and we did not find significant degrading of the precision.

Table B.6: Parts of the imaging setups.

Component	Manufacturer	Part Number
Dichroic mirror (DMD light)	Thorlabs	DMLP650L
Pressure stage (MOT optics)	Festo	DGST-8-80-Y12A
Flow control valve	Festo	GRLA-M5-QS-6-D
Solenoid valve	Festo	VUUG-L10-M52-MT-M5-1R8L
Translation stage (Secondary lens)	Thorlabs	ELL20/M
External camera shutter	Vincent Associates	Uniblitz CS45S3T0
Bandpass filter (ProEM imaging)	Semrock	FF01-766/13-25
Notch filter (ProEM imaging)	Chroma	ZET532NF
Translation stage (Pixis objective)	Physik Instrumente	Micos VT-80

—

Control Circuits for Magnetic Fields

The main coils allow for different configurations of the magnetic field, which is enabled by an H-bridge and two passbanks. This chapter gives an overview of the systems and details on the drive circuits.

The wiring of the main coils is depicted in [fig. C.1](#), and the setup is powered by a power supply that provides up to 400 A at 15 V. The direction of the current in the upper coil is controlled with an H-bridge, which is discussed in [section C.1](#). The current is measured by two current transducers (LEM IT 400-S Ultrastab) and controlled with two passbanks, which is detailed in [section C.2](#). The coils are shorted with bi-directional TVS diodes (15KP58C) that break down at about 60 V and dissipate power when the current is switched.

C.1 H-bridge

The H-bridge consists of four banks that are each equipped with six field effect transistors connected in parallel (MOSFET, IRFP4668). The mechanical design is shown in [section D.5](#). An overview of the drive circuit is given in [fig. C.2](#). It is powered by an isolated power supply at 20 V, and the ground reference for the circuits is connected to the source of the lower transistor banks. First, this ensures that the MOSFETs can be switched if the transistors of the passbanks are non-conducting. Second, it ensures that a sufficient voltage is provided at the gates of the MOSFETs to switch them in a conducting state as the upper transistor banks are located above the load and the gate voltage thus needs to be at least the voltage drop over the coil plus the gate threshold

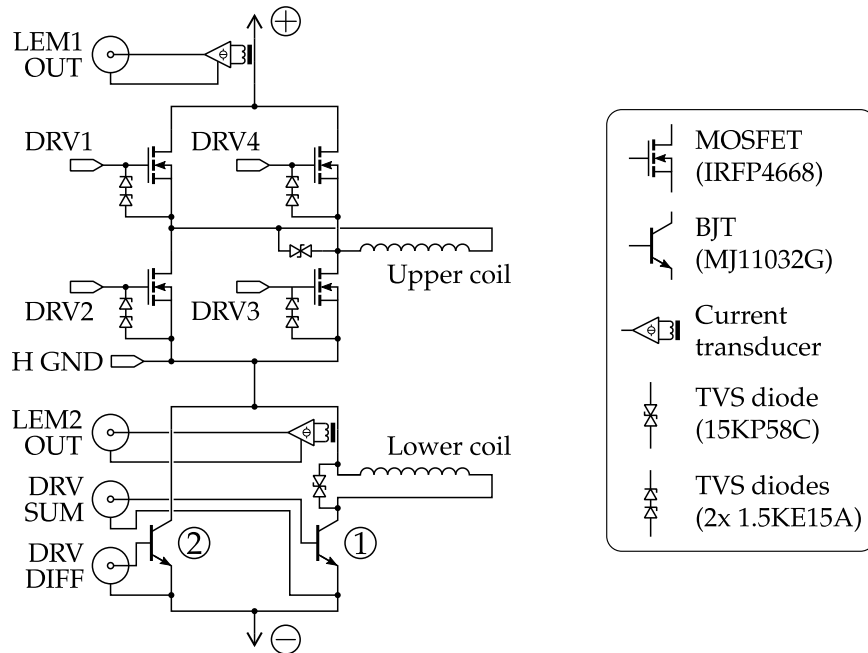


Figure C.1: Schematics of the main coil setup. The single transistors shown in the schematics represent multiple transistors connected in parallel to handle high currents, and the current transducer we use is the LEM IT 400-S Ultrastab.

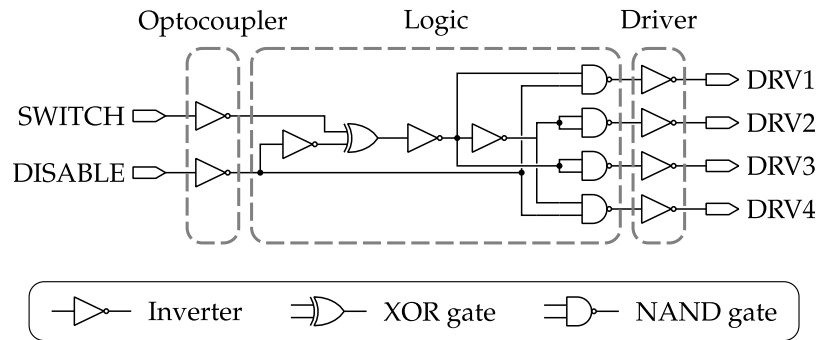


Figure C.2: Driver setup for H-bridge. The sketch shows an abstract representation of the different parts. The opto-isolators ensure decoupling from the ground of the experiment control system and invert the signal. The second stage contains TTL elements that switch between transistor bank 1 and 3, or 2 and 4 when SWITCH is toggled. The DISABLE signal switches bank 2 and 3 non-conducting and toggles the upper transistor banks (cf. fig. 3.4). The logic is followed by the MOSFET driver which inverts the signal again.



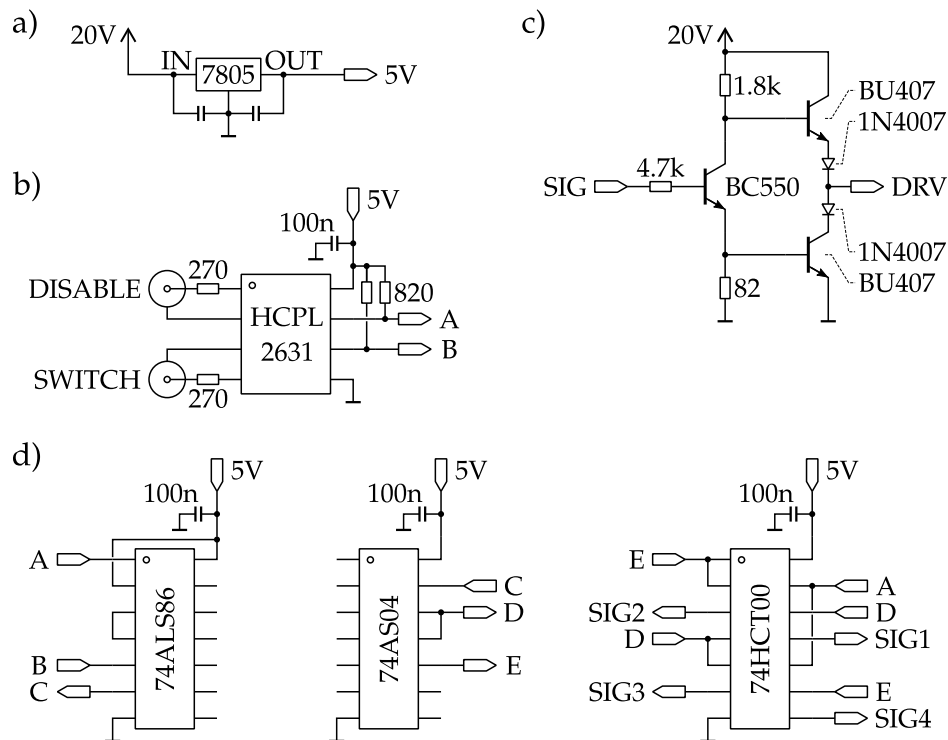


Figure C.3: Electronic schematics for H-bridge driver. Panel a) shows the power supply which derives the low voltage for the components from the 20 V to avoid ground loops. Panel b) shows the input stage that features an opto-isolator to decouple the ground, and panel d) shows the subsequent TTL modules. Panel c) shows the output stage which is a totem pole drive circuit.

voltage. The gates of the MOSFETs are protected against high voltage with two unidirectional TVS diodes (1.5KE15A) connected in series.

The schematics of the drive circuit is presented in [fig. C.3](#). The two inputs allow switching the direction of the current in the upper coil (and thus switching from the quadrupole configuration to the Feshbach configuration), and switching off the current by switching the two lower transistor banks to non-conducting. The input stage of the drive circuit features an opto-isolater that decouples the signals and prevents a ground connection to the experiment control (panel b). Subsequently, the logic is implemented by three TTL modules that address the four transistor banks (panel d). The output stage for each transistor bank is a totem pole driver which is depicted in panel c). It is powered with 20 V to ensure that the high-side MOSFETs can be switched to a

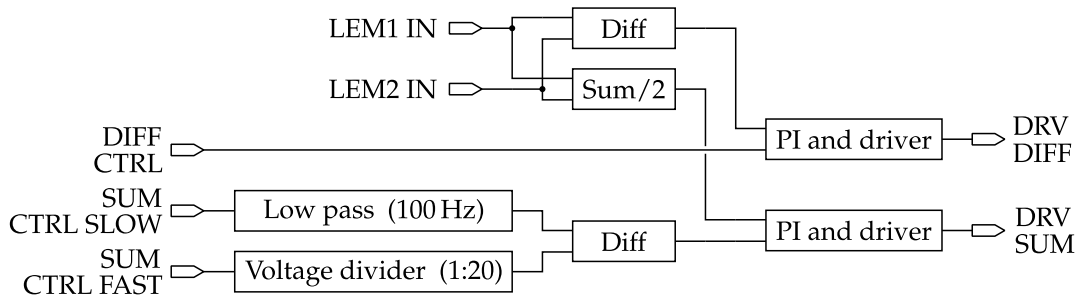


Figure C.4: Schematics of the current control. The total current and the current difference between the two coils are measured with two current transducers (LEM1 and LEM2). The current is subsequently regulated with a PI loop that drives the passbanks. To suppress noise two channels are used to control the total current.

conducting state. Additional diodes at the output prevent charge or discharge of the MOSFET gate when the current of the coil is switched, which might lead to substantial shifts of the potential at the source/drain of the transistor banks as the coils are clamped at 60 V by the TVS diodes. The lower resistor is chosen small to enable fast switching, but it has to be large enough to allow the lower transistor to open completely. The low voltage for the logic components is derived from the isolated power supply to avoid ground loops (panel a).

C.2 Passbank

The two passbanks control the current in the upper and lower coil. They employ bipolar transistors (MJ11032G) connected in parallel to handle high currents. Details on the passbank can be found in [60], and a technical drawing is provided in section D.6. An abstract diagram of the control circuit is presented in fig. C.4. The total current is regulated with passbank 1, which is placed below the lower coil in the circuit (cf. fig. C.1). Passbank 2 acts as a shunt for the lower coil and diverts the current, which leads to less current flowing through the lower coil compared to the upper coil.

The current is measured by two current transducers placed at the input cable (LEM1) and above the lower coil (LEM2). As a measure for the total current half of the sum of the signals is derived, and to measure the current imbalance in the two coils the difference of the signals is used. Detailed schematics of the circuit are shown in fig. C.5. The signal from the transducers



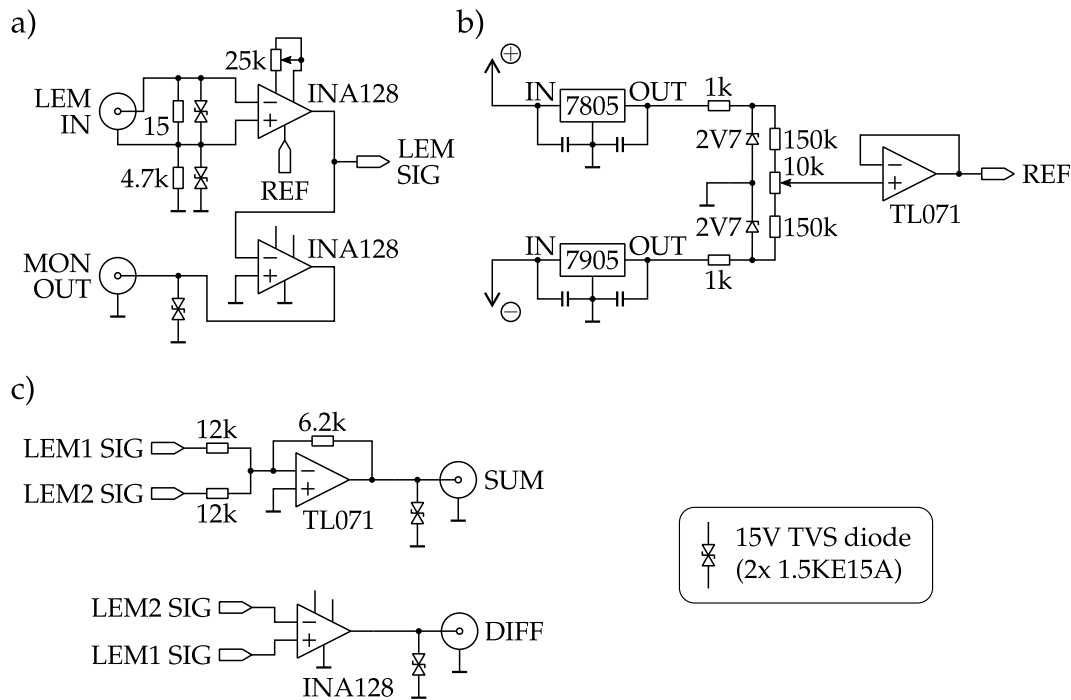


Figure C.5: Electronic schematics for generation of the current signal. Panel a) shows the circuit that converts the current from the current transducers (LEM) to a voltage, and provides a monitor signal. The instrumentation amplifier needs a stable reference which is used to calibrate the offset of the transducer. It is provided by the circuit shown in panel b). Finally, the sum and difference signals are derived from the signal of the current transducers by the circuit shown in panel c). Over-voltage protection is provided by uni-directional TVS diodes that are put back-to-back.

is a current which is sensed by a resistor implemented with many resistors in parallel to avoid heating and subsequent changes of the resistance. The voltage drop is amplified by an instrumentation amplifier (panel a). It is important that the amplifier is provided with a stable reference signal to calibrate the offset. The corresponding circuit is shown in panel b), where a stable voltage is provided by voltage regulators and subsequently clamped with Zener diodes. Finally, the sum and difference of the two LEM signals are provided by operational amplifiers (panel c).

To increase the stability of the set point, two analog channels of the experiment control are utilized to control the total current. One channel provides large changes in the signal. It is filtered with a low pass to suppress noise and

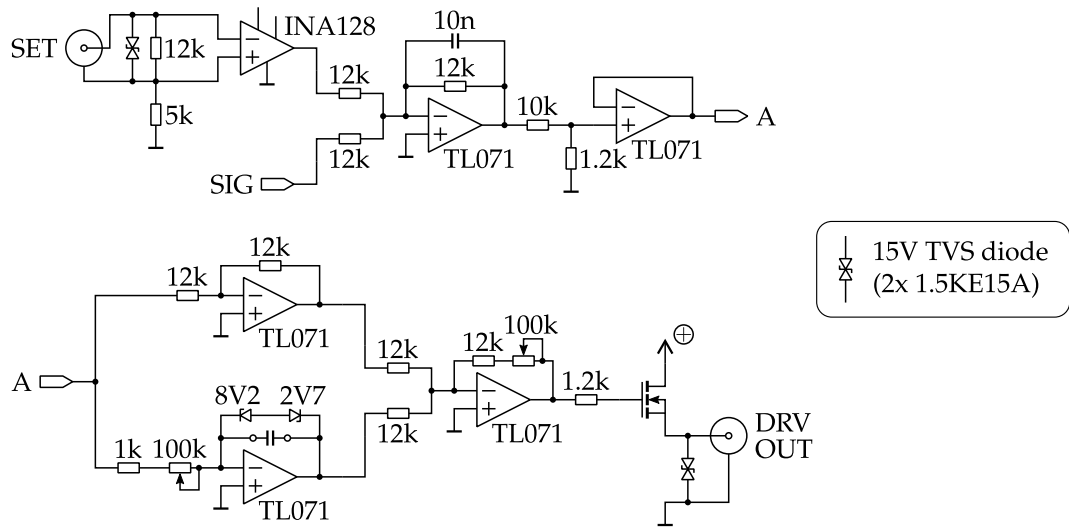


Figure C.6: Electronic schematics of the PI controller. The drive circuits for the passbanks use a PI controller to stabilize the current. The output stage is implemented with a high-current MOSFET. Over-voltage protection is provided by uni-directional TVS diodes that are put back-to-back.

hence allows only for slow changes of the set point. The second channel is attenuated with a voltage divider to suppress noise. It thus allows for smaller but fast changes of the signal. The two signals are subtracted and used as set point for the total current. For the difference the signal from the experiment control is used directly.

The current is regulated with a PI controller which drives the bipolar transistors of the passbank, and the schematics are shown in [fig. C.6](#). The first stage sums the input signal (SUM or DIFF) with the inverted set point and filters high frequencies with its capacitor (cutoff frequency 2 kHz). It is followed by an attenuator that adapts the voltage levels and allows setting the gain of the following amplifier stages above one. The attenuator is buffered and followed by one more unity-gain buffer which is connected in parallel to the integral stage. The latter features two Zener diodes that limit the loading of the capacitor and allow faster switching after the PI controller was at a limit. Both signals are summed and amplified. They drive a high-current MOSFET, which provides the drive current for the passbank.

APPENDIX **D**

Technical Drawings

In this chapter technical drawings and sketches of experimental parts and the setup are presented. The measurements are given in millimeters if not specified differently.

This space is intentionally left blank.

D.1 Objective (ProEM imaging)

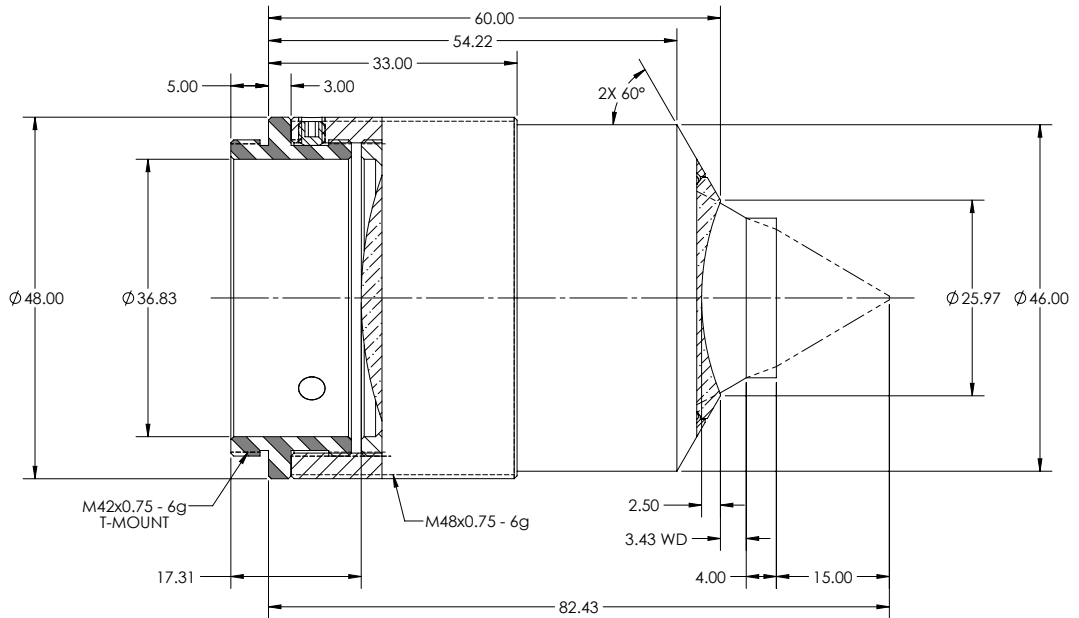


Figure D.1: Technical drawing of the ProEM objective. We removed the grey/white striped part as the objective is fixed by its outer thread. Adapted from a technical drawing by *Special Optics*.

D.2 Objective (Pixis imaging)

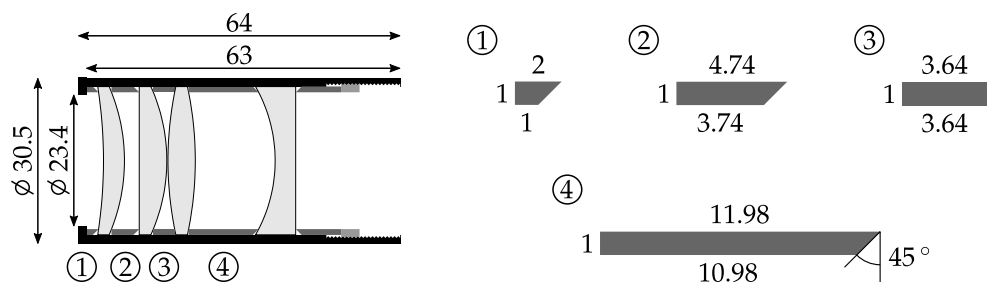


Figure D.2: Technical drawing of the Pixis objective. The drawing gives the dimensions of lens tube and spacer rings. The tube is manufactured from PEEK and the spacers from ceramic.



D.3 Distances in Vertical Plane at the Glass Cell

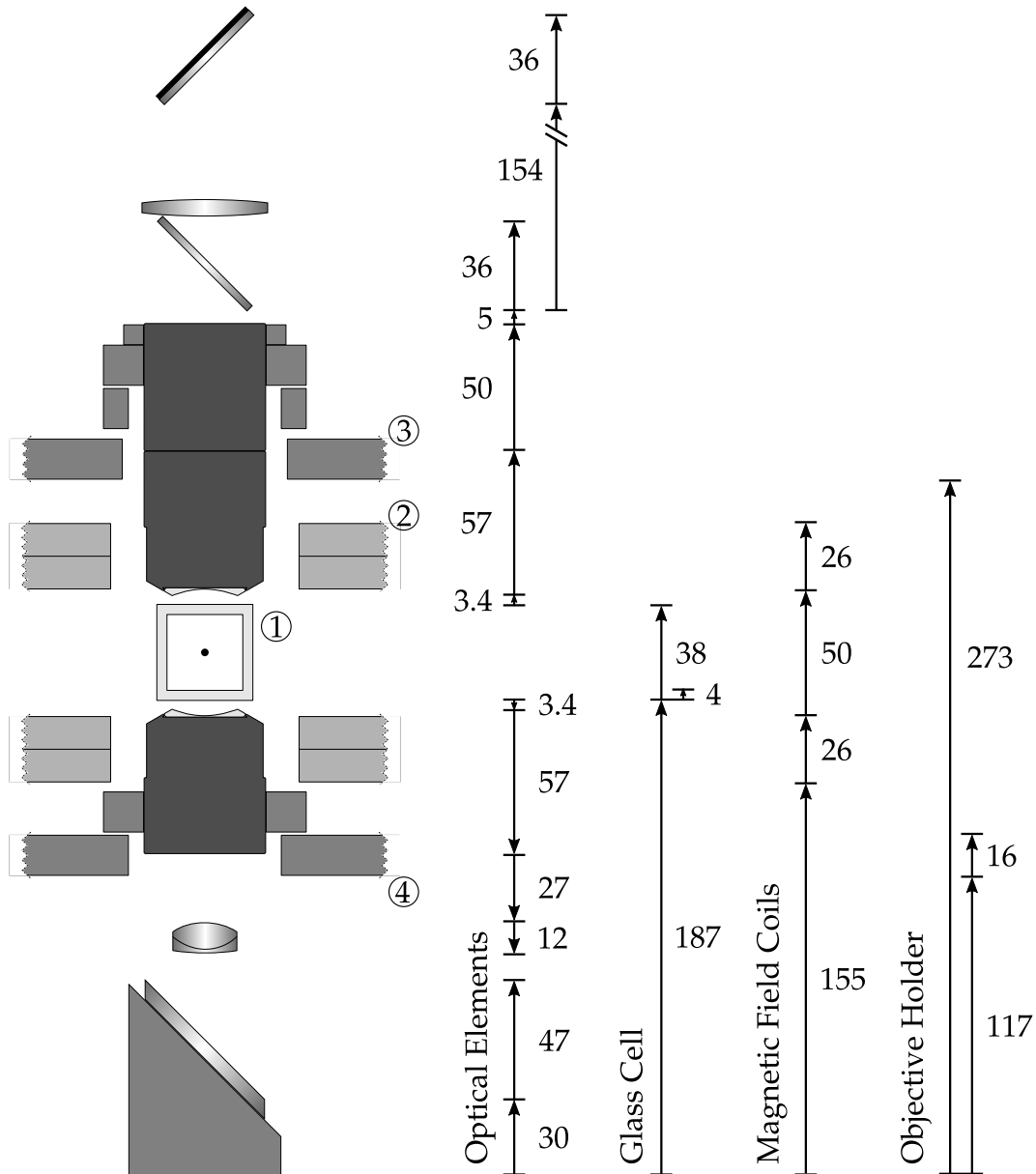


Figure D.3: Vertical dimensions of the experimental setup. The sketch shows the glass cell (1) in the centre, with objectives above and below. The magnetic field coils (2), the upper (3) and lower (4) objective holders, and the optics of the vertical beam path are displayed.

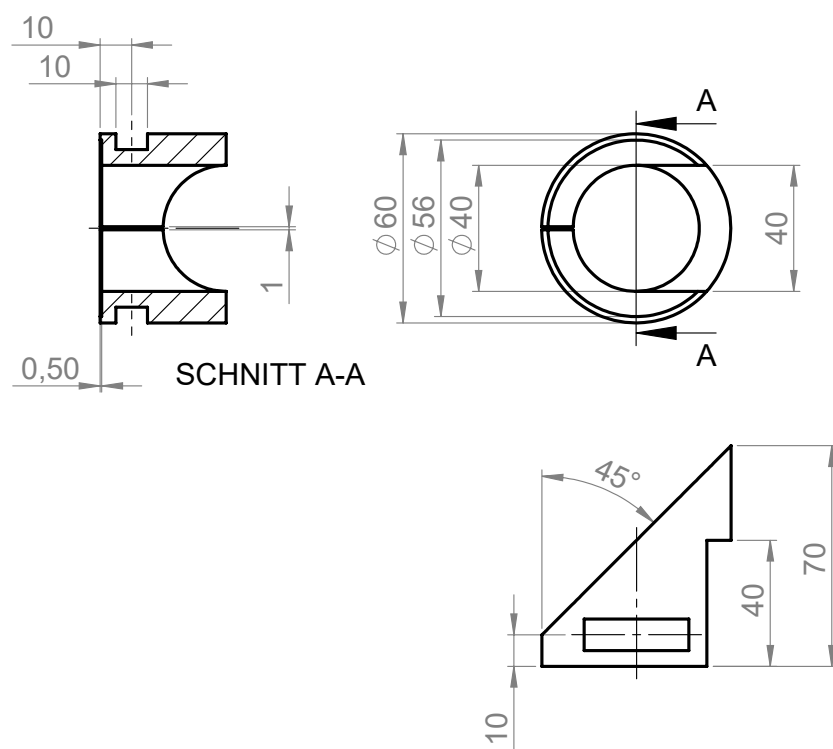


Figure D.4: Holder for lower MOT mirror. The holder is designed such that a beam can be guided from below through the mirror, and it has a cut to avoid eddie currents as it is manufactured from brass. The mirror is glued onto the holder. Adapted from a technical drawing by David Jansen.



D.4 Objective Holder

The holder is manufactured from PEEK, and the commercial parts are given in table B.4. All figures are adapted from technical drawings by David Jansen.

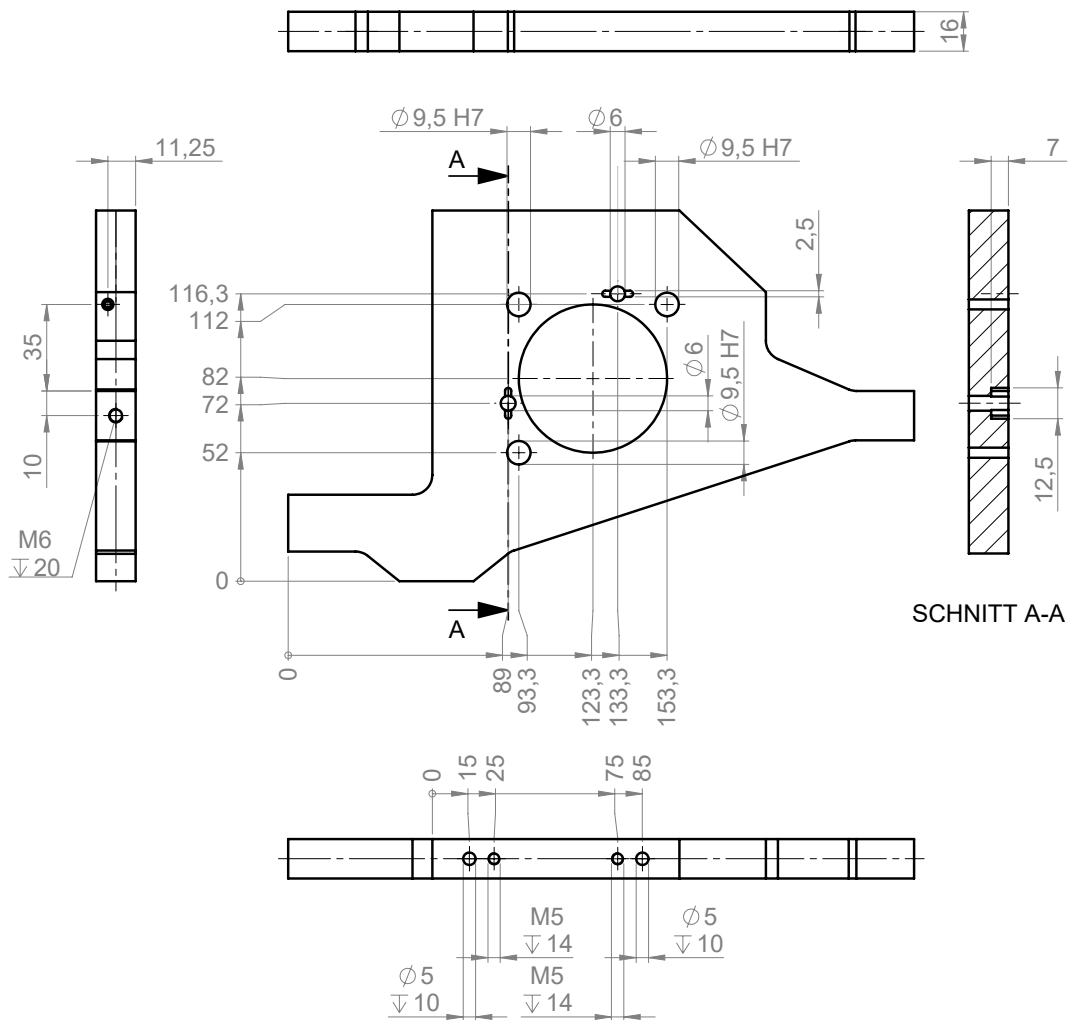


Figure D.5: Lower holder, part 1.

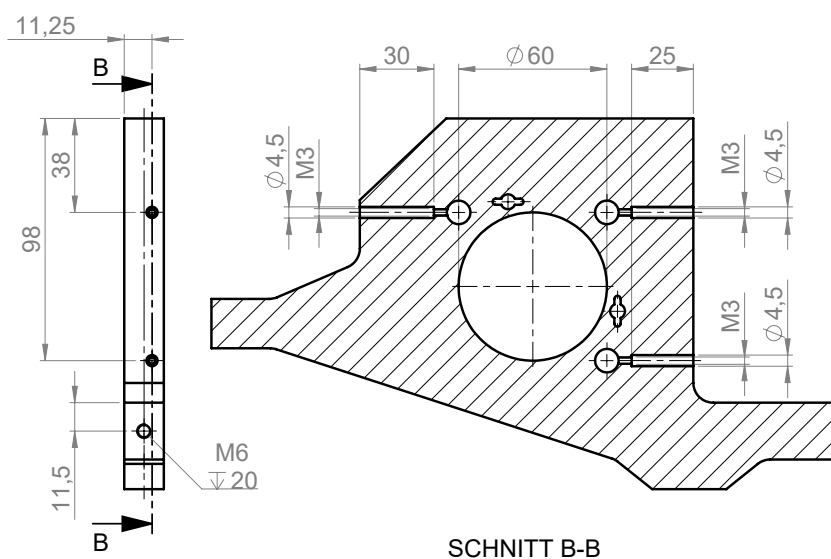


Figure D.6: Lower holder, part 2.

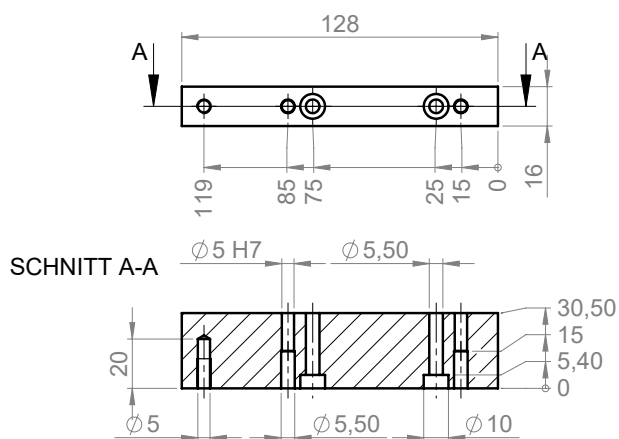


Figure D.7: Extension for lower holder. The lower holder consists of two parts to be installed without removing the main magnetic coils. This part was screwed to the holder after it was in place.



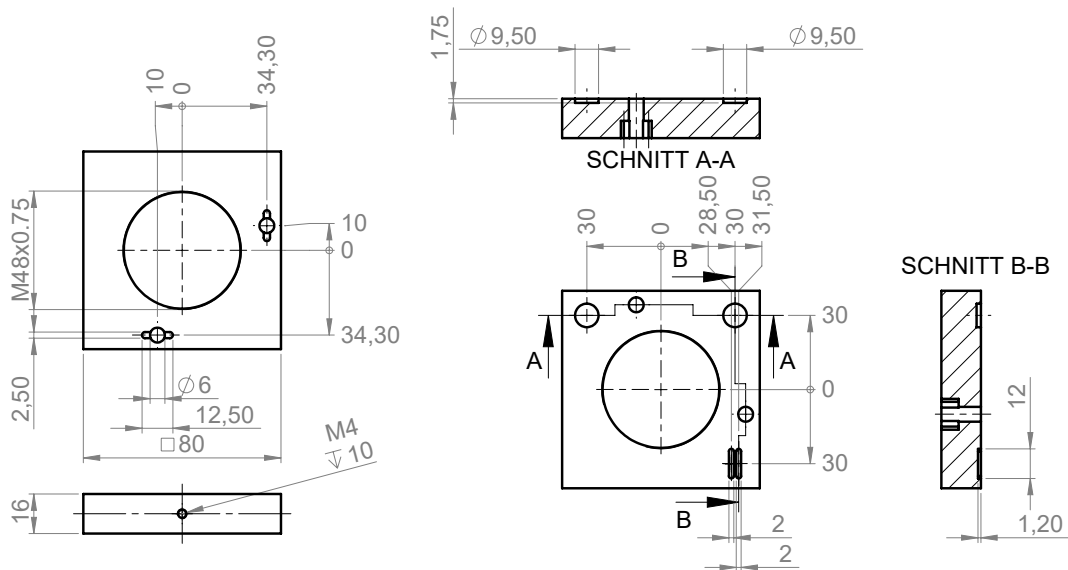


Figure D.8: Tip/tilt stage for lower holder.

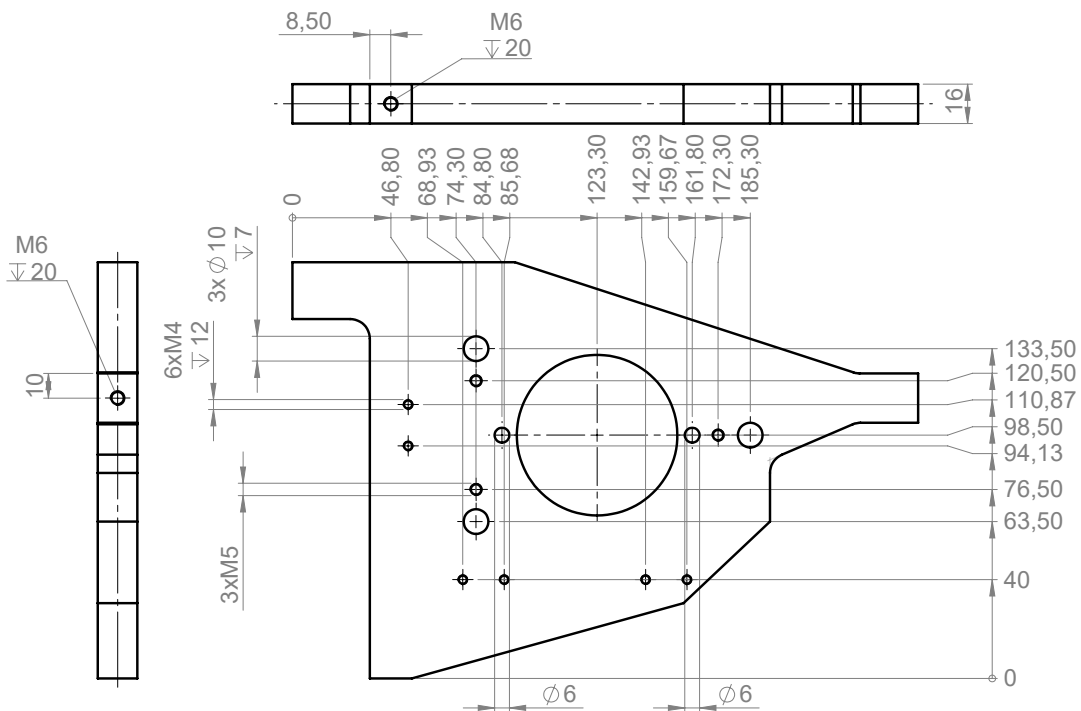


Figure D.9: Upper holder, part 1.

D.5 H-bridge

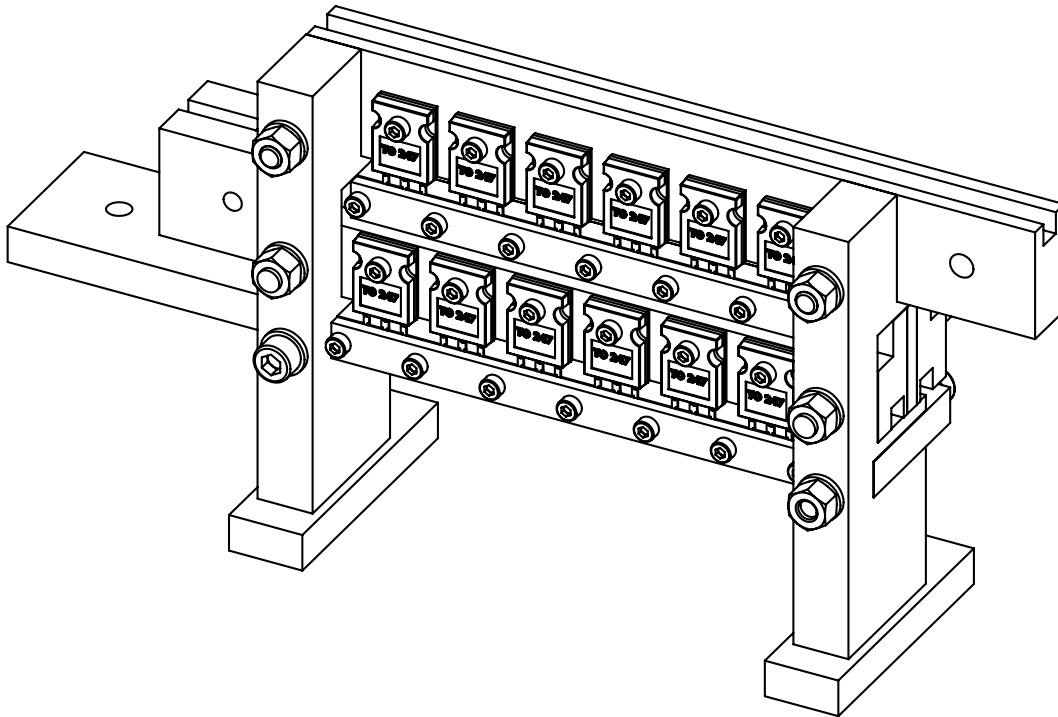


Figure D.12: Sketch of the H-bridge assembly. The electrical connection of the transistors is realized with the backplane (drain) and one leg (source), which is connected to the lower bar. The electrical connection of the gate is not shown in the sketch. The bars for mounting the transistors are manufactured from copper. They are water-cooled with copper pipes which are soldered into the channels visible in the sketch. The figure is adapted from a technical drawing by David Jansen.

D.6 Passbank

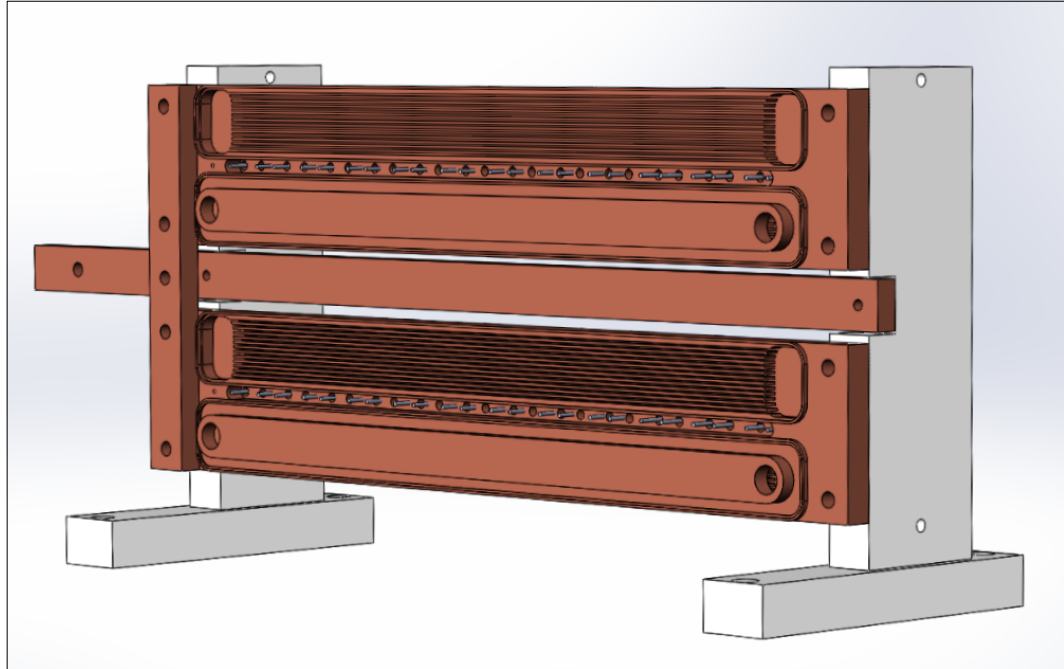


Figure D.13: Sketch of the passbank assembly. The sketch shows the back of the passbank without electrical connections. The transistors are mounted on the other side and their legs are visible in the sketch. The copper bars are each cooled with two channels. Each channel features narrow grooves milled in the copper to increase the contact area with the cooling water, and the channel is sealed with a copper lid, which is welded onto the bar. The passbank cools the transistors very well, and it was designed and manufactured by David Jansen.

List of Publications

- M. Hans, F. Schmutte, C. Viermann, N. Liebster, M. Sparn, M. K. Oberthaler, and H. Strobel, “High signal to noise absorption imaging of alkali atoms at moderate magnetic fields”, *Rev. Sci. Instrum.* **92**, 023203 (2021)
- C. Viermann, M. Sparn, N. Liebster, M. Hans, E. Kath, Á. Parra-López, M. Tolosa-Simeón, N. Sánchez-Kuntz, T. Haas, H. Strobel, S. Floerchinger, and M. K. Oberthaler, “Quantum field simulator for dynamics in curved spacetime”, [arXiv:2202.10399](https://arxiv.org/abs/2202.10399) (2022), accepted by Nature
- M. Tolosa-Simeón, Á. Parra-López, N. Sánchez-Kuntz, T. Haas, C. Viermann, M. Sparn, N. Liebster, M. Hans, E. Kath, H. Strobel, M. K. Oberthaler, and S. Floerchinger, “Curved and expanding spacetime geometries in Bose-Einstein condensates”, [arXiv:2202.10441](https://arxiv.org/abs/2202.10441) (2022), accepted by Phys. Rev. A

Bibliography

- [1] T. Freeth, Y. Bitsakis, X. Moussas, J. H. Seiradakis, A. Tselikas, H. Mangou, M. Zafeiropoulou, R. Hadland, D. Bate, A. Ramsey, M. Allen, A. Crawley, P. Hockley, T. Malzbender, D. Gelb, W. Ambrisco, and M. G. Edmunds, “Decoding the ancient Greek astronomical calculator known as the Antikythera Mechanism”, *Nature* **444**, 587–591 (2006).
- [2] J. Thomson and W. Thomson, “On an integrating machine having a new kinematic principle”, *Proc. R. Soc. Lond.* **24**, 262–265 (1876).
- [3] V. Bush, “The differential analyzer. A new machine for solving differential equations”, *J. Frankl. Inst.* **212**, 447–488 (1931).
- [4] B. Parker, “The tide predictions for D-Day”, *Physics Today* **64**, 35–40 (2011).
- [5] A. Clymer, “The mechanical analog computers of Hannibal Ford and William Newell”, *IEEE Ann. Hist. Comput.* **15**, 19–34 (1993).
- [6] J. E. Tomayko, “Helmut Hoelzer’s Fully Electronic Analog Computer”, *IEEE Ann. Hist. Comput.* **7**, 227–240 (1985).
- [7] W. Haensch, T. Gokmen, and R. Puri, “The Next Generation of Deep Learning Hardware: Analog Computing”, *Proceedings of the IEEE* **107**, 108–122 (2019).
- [8] R. P. Feynman, “Simulating physics with computers”, *Int. J. Theor. Phys.* **21**, 467–488 (1982).
- [9] T. H. Johnson, S. R. Clark, and D. Jaksch, “What is a quantum simulator?”, *EPJ Quantum Technol.* **1**, 1–12 (2014).
- [10] S. N. Bose, “Plancks Gesetz und Lichtquantenhypothese”, *Z. Physik* **26**, 178–181 (1924).
- [11] A. Einstein, “Quantentheorie des einatomigen idealen Gases”, *Sitzber. Kgl. Preuss. Akad. Wiss.*, 261–267 (1924).

Bibliography

- [12] M. H. Anderson, J. R. Ensher, M. R. Matthews, C. E. Wieman, and E. A. Cornell, "Observation of Bose-Einstein Condensation in a Dilute Atomic Vapor", *Science* **269**, 198–201 (1995).
- [13] K. B. Davis, M.-O. Mewes, M. R. Andrews, N. J. van Druten, D. S. Durfee, D. M. Kurn, and W. Ketterle, "Bose-Einstein Condensation in a Gas of Sodium Atoms", *Phys. Rev. Lett.* **75**, 3969–3973 (1995).
- [14] C. C. Bradley, C. A. Sackett, J. J. Tollett, and R. G. Hulet, "Evidence of Bose-Einstein Condensation in an Atomic Gas with Attractive Interactions", *Phys. Rev. Lett.* **75**, 1687–1690 (1995).
- [15] D. M. Stamper-Kurn, M. R. Andrews, A. P. Chikkatur, S. Inouye, H.-J. Miesner, J. Stenger, and W. Ketterle, "Optical Confinement of a Bose-Einstein Condensate", *Phys. Rev. Lett.* **80**, 2027–2030 (1998).
- [16] S. Inouye, M. R. Andrews, J. Stenger, H.-J. Miesner, D. M. Stamper-Kurn, and W. Ketterle, "Observation of Feshbach resonances in a Bose-Einstein condensate", *Nature* **392**, 151–154 (1998).
- [17] C. D'Errico, M. Zaccanti, M. Fattori, G. Roati, M. Inguscio, G. Modugno, and A. Simoni, "Feshbach resonances in ultracold ^{39}K ", *New J. Phys.* **9**, 223–223 (2007).
- [18] G. Gauthier, I. Lenton, N. M. Parry, M. Baker, M. J. Davis, H. Rubinsztein-Dunlop, and T. W. Neely, "Direct imaging of a digital-micromirror device for configurable microscopic optical potentials", *Optica* **3**, 1136–1143 (2016).
- [19] R. Saint-Jalm, P. C. M. Castilho, É. Le Cerf, B. Bakkali-Hassani, J.-L. Ville, S. Nascimbene, J. Beugnon, and J. Dalibard, "Dynamical Symmetry and Breathers in a Two-Dimensional Bose Gas", *Phys. Rev. X* **9**, 021035 (2019).
- [20] F. Rosenblatt, "The perceptron: A probabilistic model for information storage and organization in the brain", *Psychological Review* **65**, 386–408 (1958).
- [21] D. Verstraeten, B. Schrauwen, M. D'Haene, and D. Stroobandt, "An experimental unification of reservoir computing methods", *Neural Networks* **20**, 391–403 (2007).
- [22] M. Lukoševičius and H. Jaeger, "Reservoir computing approaches to recurrent neural network training", *Comput. Sci. Rev.* **3**, 127–149 (2009).

- [23] G. Tanaka, T. Yamane, J. B. Héroux, R. Nakane, N. Kanazawa, S. Takeda, H. Numata, D. Nakano, and A. Hirose, “Recent advances in physical reservoir computing: A review”, *Neural Networks* **115**, 100–123 (2019).
- [24] K. Nakajima, “Physical reservoir computing—an introductory perspective”, *Jpn. J. Appl. Phys.* **59**, 060501 (2020).
- [25] K. Nakajima and I. Fischer, eds., *Reservoir Computing: Theory, Physical Implementations, and Applications* (Springer Singapore, Singapore, 2021).
- [26] W. D. Phillips, “Nobel Lecture: Laser cooling and trapping of neutral atoms”, *Rev. Mod. Phys.* **70**, 721–741 (1998).
- [27] T. G. Tiecke, “Properties of potassium”, Appendix A of PhD thesis, v1.02 (University of Amsterdam, 2011).
- [28] A. F. Impertro, “Laser system for magneto-optical cooling and trapping of potassium”, BA thesis (Universität Heidelberg, 2017).
- [29] H. J. Metcalf and P. van der Straten, *Laser cooling and trapping* (Springer, New York, 1999).
- [30] G. K. Woodgate, *Elementary atomic structure* (Clarendon Press, Oxford, 1992).
- [31] G. Breit and I. I. Rabi, “Measurement of Nuclear Spin”, *Phys. Rev.* **38**, 2082–2083 (1931).
- [32] E. Arimondo, M. Inguscio, and P. Violino, “Experimental determinations of the hyperfine structure in the alkali atoms”, *Rev. Mod. Phys.* **49**, 31–75 (1977).
- [33] C. Pethick and H. Smith, *Bose-Einstein condensation in dilute gases* (Cambridge University Press, Cambridge, 2008).
- [34] C. Chin, R. Grimm, P. Julienne, and E. Tiesinga, “Feshbach resonances in ultracold gases”, *Rev. Mod. Phys.* **82**, 1225–1286 (2010).
- [35] C. Viermann, “Cosmological particle production and curved spaces in an ultracold quantum gas”, PhD thesis (Universität Heidelberg, 2022).
- [36] M. Landini, “A tunable Bose-Einstein condensate for quantum interferometry”, PhD thesis (Università degli Studi di Trento, Trento, 2011).
- [37] P. D. Lett, R. N. Watts, C. I. Westbrook, W. D. Phillips, P. L. Gould, and H. J. Metcalf, “Observation of Atoms Laser Cooled below the Doppler Limit”, *Phys. Rev. Lett.* **61**, 169–172 (1988).

Bibliography

- [38] J. Dalibard and C. Cohen-Tannoudji, "Laser cooling below the Doppler limit by polarization gradients: simple theoretical models", *J. Opt. Soc. Am. B* **6**, 2023 (1989).
- [39] S. A. Hopkins and A. V. Durrant, "Parameters for polarization gradients in three-dimensional electromagnetic standing waves", *Phys. Rev. A* **56**, 4012–4022 (1997).
- [40] M. Landini, S. Roy, L. Carcagní, D. Trypogeorgos, M. Fattori, M. Inguscio, and G. Modugno, "Sub-Doppler laser cooling of potassium atoms", *Phys. Rev. A* **84**, 043432 (2011).
- [41] V. Gokhroo, G. Rajalakshmi, R. K. Easwaran, and C. S. Unnikrishnan, "Sub-Doppler deep-cooled bosonic and fermionic isotopes of potassium in a compact $2D^+ - 3D$ MOT set-up", *J. Phys. B: At. Mol. Opt. Phys.* **44**, 115307 (2011).
- [42] A. Aspect, E. Arimondo, R. Kaiser, N. Vansteenkiste, and C. Cohen-Tannoudji, "Laser Cooling below the One-Photon Recoil Energy by Velocity-Selective Coherent Population Trapping", *Phys. Rev. Lett.* **61**, 826–829 (1988).
- [43] M. Weidemüller, T. Esslinger, M. A. Ol'shanii, A. Hemmerich, and T. W. Hänsch, "A Novel Scheme for Efficient Cooling below the Photon Recoil Limit", *EPL* **27**, 109–114 (1994).
- [44] G. Salomon, L. Fouché, P. Wang, A. Aspect, P. Bouyer, and T. Bourdel, "Gray-molasses cooling of ^{39}K to a high phase-space density", *EPL* **104**, 63002 (2013).
- [45] D. Nath, R. K. Easwaran, G. Rajalakshmi, and C. S. Unnikrishnan, "Quantum-interference-enhanced deep sub-Doppler cooling of ^{39}K atoms in gray molasses", *Phys. Rev. A* **88**, 053407 (2013).
- [46] W. H. Wing, "On neutral particle trapping in quasistatic electromagnetic fields", *Prog. Quantum Electron.* **8**, 181–199 (1984).
- [47] R. Grimm, M. Weidemüller, and Y. B. Ovchinnikov, "Optical Dipole Traps for Neutral Atoms", in *Advances In Atomic, Molecular, and Optical Physics*, Vol. 42, edited by B. Bederson and H. Walther (Academic Press, 2000), pp. 95–170.
- [48] B. Lee, "Introduction to ± 12 degree orthogonal digital micromirror devices (DMDs)", *Texas Instruments* (2008).

- [49] C. C. Bradley, C. A. Sackett, and R. G. Hulet, “Bose-Einstein Condensation of Lithium: Observation of Limited Condensate Number”, *Phys. Rev. Lett.* **78**, 985–989 (1997).
- [50] M. Landini, S. Roy, G. Roati, A. Simoni, M. Inguscio, G. Modugno, and M. Fattori, “Direct evaporative cooling of ^{39}K atoms to Bose-Einstein condensation”, *Phys. Rev. A* **86**, 033421 (2012).
- [51] W. Ketterle, D. S. Durfee, and D. M. Stamper-Kurn, *Making, probing and understanding Bose-Einstein condensates*, 1999, [arXiv:cond-mat/9904034](https://arxiv.org/abs/cond-mat/9904034).
- [52] L. P. Pitaevskii and S. Stringari, *Bose-Einstein condensation* (Clarendon Press, Oxford, 2003).
- [53] D. S. Petrov, G. V. Shlyapnikov, and J. T. M. Walraven, “Regimes of Quantum Degeneracy in Trapped 1D Gases”, *Phys. Rev. Lett.* **85**, 3745–3749 (2000).
- [54] G. Roati, M. Zaccanti, C. D’Errico, J. Catani, M. Modugno, A. Simoni, M. Inguscio, and G. Modugno, “ ^{39}K Bose-Einstein Condensate with Tunable Interactions”, *Phys. Rev. Lett.* **99**, 010403 (2007).
- [55] G. Salomon, L. Fouché, S. Lepoutre, A. Aspect, and T. Bourdel, “All-optical cooling of ^{39}K to Bose-Einstein condensation”, *Phys. Rev. A* **90**, 033405 (2014).
- [56] G. Semeghini, “Ultracold atoms in three-dimensional disorder: measurement of the mobility edge and effect of weak interactions”, PhD thesis (Università degli Studi di Firenze, 2015).
- [57] R. J. Fletcher, “Bose-Einstein Condensation and Superfluidity in Two Dimensions”, PhD thesis (University of Cambridge, 2015).
- [58] C. R. Cabrera Córdova, “Quantum liquids droplets in a mixture of Bose-Einstein condensates”, PhD thesis (Universidad Politécnica de Cataluña, 2018).
- [59] J. L. Ville, T. Bienaimé, R. Saint-Jalm, L. Corman, M. Aidelsburger, L. Chomaz, K. Kleinlein, D. Perconte, S. Nascimbène, J. Dalibard, and J. Beugnon, “Loading and compression of a single two-dimensional Bose gas in an optical accordion”, *Phys. Rev. A* **95**, 013632 (2017).
- [60] M. Hans, “An experimental setup for a potassium Bose-Einstein condensate with tunable interactions”, MA thesis (Universität Heidelberg, 2017).

Bibliography

- [61] M. Sparn, "Magnetic Fields for Cooling and Trapping of Potassium Atoms", BA thesis (Universität Heidelberg, 2017).
- [62] A. A. Beikert, "Controlled Frequency Generation for Grey Molasses Cooling", BA thesis (Universität Heidelberg, 2021).
- [63] M. Sparn, "A Setup for Creating Arbitrary Potentials in a Two-dimensional ^{39}K BEC with a Digital Micromirror Device", MA thesis (Universität Heidelberg, 2020).
- [64] J. Krieger, "Zeeman-Slower und Experimentsteuerung für das NaLi-Experiment", Diploma thesis (Universität Heidelberg, 2008).
- [65] W. Müssel, "Characterization of a Two-dimensional MOT for ^{39}K ", Diploma thesis (Universität Heidelberg, 2011).
- [66] I. Stroescu, "On a cold beam of potassium atoms", Diploma thesis (Universität Heidelberg, 2010).
- [67] C. J. Foot, *Atomic physics* (Oxford University Press, Oxford, 2005).
- [68] F. Nicolai, "Design and construction of a fiber-coupled tapered amplifier system", MA thesis (Universität Heidelberg, 2017).
- [69] B. E. A. Saleh and M. C. Teich, *Fundamentals of photonics* (Wiley Interscience, Hoboken, NJ, 2007).
- [70] E. A. Donley, T. P. Heavner, F. Levi, M. O. Tataw, and S. R. Jefferts, "Double-pass acousto-optic modulator system", *Rev. Sci. Instrum.* **76**, 063112 (2005).
- [71] E. Kath, "Feasibility of Single-Atom-Resolved Fluorescence Imaging of Freely Propagating ^{39}K Atoms", MA thesis (Universität Heidelberg, 2022).
- [72] A. Bergschneider, V. M. Klinkhamer, J. H. Becher, R. Klemt, G. Zürn, P. M. Preiss, and S. Jochim, "Spin-resolved single-atom imaging of ^6Li in free space", *Phys. Rev. A* **97**, 063613 (2018).
- [73] B. Erdmann, "Wechselwirkung von atomaren Mehrniveau-Systemen mit Laserlicht", BA thesis (Universität Heidelberg, 2019).
- [74] F. A. Schmutte, "Closed Optical Cycle Scheme for Absorption Imaging of ^{39}K Atoms at Intermediate Magnetic Field Strengths", BA thesis (Universität Heidelberg, 2020).
- [75] J. Dreher, "An Offset Locking Scheme for Absorption Imaging of ^{39}K at High Magnetic Fields", BA thesis (Universität Heidelberg, 2019).

- [76] M. Hans, F. Schmutte, C. Viermann, N. Liebster, M. Sparn, M. K. Oberthaler, and H. Strobel, “High signal to noise absorption imaging of alkali atoms at moderate magnetic fields”, *Rev. Sci. Instrum.* **92**, 023203 (2021).
- [77] M. Berninger, “Universal three- and four-body phenomena in an ultracold gas of cesium atoms”, PhD thesis (Universität Innsbruck, 2011).
- [78] M. Berninger, A. Zenesini, B. Huang, W. Harm, H.-C. Nägerl, F. Ferlaino, R. Grimm, P. S. Julienne, and J. M. Hutson, “Universality of the Three-Body Parameter for Efimov States in Ultracold Cesium”, *Phys. Rev. Lett.* **107**, 120401 (2011).
- [79] G. Reinaudi, T. Lahaye, Z. Wang, and D. Guery-Odelin, “Strong saturation absorption imaging of dense clouds of ultracold atoms”, *Opt. Lett.* **32**, 3143 (2007).
- [80] M. Born and E. Wolf, *Principles of optics: electromagnetic theory of propagation, interference and diffraction of light* (Cambridge University Press, Cambridge, 1999).
- [81] T. B. Ottenstein, “A New Objective for High Resolution Imaging of Bose-Einstein Condensates”, Diploma thesis (Universität Heidelberg, 2006).
- [82] W. Müssel, H. Strobel, M. Joos, E. Nicklas, I. Stroescu, J. Tomkovič, D. B. Hume, and M. K. Oberthaler, “Optimized absorption imaging of mesoscopic atomic clouds”, *Appl. Phys. B* **113**, 69–73 (2013).
- [83] L. M. Bennie, P. T. Starkey, M. Jasperse, C. J. Billington, R. P. Anderson, and L. D. Turner, “A versatile high resolution objective for imaging quantum gases”, *Opt. Express* **21**, 9011 (2013).
- [84] J. D. Pritchard, J. A. Isaacs, and M. Saffman, “Long working distance objective lenses for single atom trapping and imaging”, *Rev. Sci. Instrum.* **87**, 073107 (2016).
- [85] U. Schünemann, H. Engler, R. Grimm, M. Weidemüller, and M. Zielonkowski, “Simple scheme for tunable frequency offset locking of two lasers”, *Rev. Sci. Instrum.* **70**, 242–243 (1999).
- [86] B. Widrow, W. H. Pierce, and J. B. Angell, “Birth, Life, and Death in Microelectronic Systems”, *IRE Transactions on Military Electronics MIL-5*, 191–201 (1961).

- [87] N. H. Farhat, D. Psaltis, A. Prata, and E. Paek, “Optical implementation of the Hopfield model”, *Appl. Opt.* **24**, 1469–1475 (1985).
- [88] D. Psaltis, D. Brady, X.-G. Gu, and S. Lin, “Holography in artificial neural networks”, *Nature* **343**, 325–330 (1990).
- [89] W. Maass, T. Natschläger, and H. Markram, “Real-Time Computing Without Stable States: A New Framework for Neural Computation Based on Perturbations”, *Neural Comput.* **14**, 2531–2560 (2002).
- [90] T. Natschläger, W. Maass, and H. Markram, “The “liquid computer”: A novel strategy for real-time computing on time series”, *Telematik* **8**, 39–43 (2002).
- [91] C. Fernando and S. Sojakka, “Pattern Recognition in a Bucket”, in *Advances in Artificial Life*, edited by W. Banzhaf, J. Ziegler, T. Christaller, P. Dittrich, and J. T. Kim (2003), pp. 588–597.
- [92] B. Schölkopf and A. J. Smola, *Learning with kernels: support vector machines, regularization, optimization, and beyond* (The MIT Press, Cambridge, Massachusetts, 2002).
- [93] V. Kecman, “Support Vector Machines – An Introduction”, in *Support Vector Machines: Theory and Applications*, edited by L. Wang, Studies in Fuzziness and Soft Computing (Springer, Berlin, Heidelberg, 2005), pp. 1–47.
- [94] K. Vandoorne, P. Mechet, T. Van Vaerenbergh, M. Fiers, G. Morthier, D. Verstraeten, B. Schrauwen, J. Dambre, and P. Bienstman, “Experimental demonstration of reservoir computing on a silicon photonics chip”, *Nat. Commun.* **5**, 3541 (2014).
- [95] L. Larger, A. Baylón-Fuentes, R. Martinenghi, V. S. Udaltsov, Y. K. Chembo, and M. Jacquot, “High-Speed Photonic Reservoir Computing Using a Time-Delay-Based Architecture: Million Words per Second Classification”, *Phys. Rev. X* **7**, 011015 (2017).
- [96] U. Teğın, M. Yıldırım, İ. Oğuz, C. Moser, and D. Psaltis, “Scalable optical learning operator”, *Nat. Comput. Sci.* **1**, 542–549 (2021).
- [97] Z. Denis, I. Favero, and C. Ciuti, “Photonic Kernel Machine Learning for Ultrafast Spectral Analysis”, *Phys. Rev. Applied* **17**, 034077 (2022).

- [98] F. Hadaeghi, “Neuromorphic Electronic Systems for Reservoir Computing”, in *Reservoir Computing: Theory, Physical Implementations, and Applications*, edited by K. Nakajima and I. Fischer, Natural Computing Series (Springer, Singapore, 2021), pp. 221–237.
- [99] F. Wyffels, M. D’Haene, T. Waegeman, K. Caluwaerts, C. Nunes, and B. Schrauwen, “Realization of a passive compliant robot dog”, in *2010 3rd IEEE RAS & EMBS International Conference on Biomedical Robotics and Biomechatronics* (2010), pp. 882–886.
- [100] K. Nakajima, H. Hauser, T. Li, and R. Pfeifer, “Information processing via physical soft body”, *Sci. Rep.* **5**, 10487 (2015).
- [101] H. Hauser, “Physical Reservoir Computing in Robotics”, in *Reservoir Computing: Theory, Physical Implementations, and Applications*, edited by K. Nakajima and I. Fischer, Natural Computing Series (Springer, Singapore, 2021), pp. 169–190.
- [102] H. Jaeger, “The “echo state” approach to analysing and training recurrent neural networks-with an erratum note”, *German Nat. Res. Cent. Inf. Technol. GMD Tech. Rep.* **148**, 13 (2001).
- [103] L. Grigoryeva and J.-P. Ortega, “Echo state networks are universal”, *Neural Networks* **108**, 495–508 (2018).
- [104] W. Maass, T. Natschläger, and H. Markram, “Fading memory and kernel properties of generic cortical microcircuit models”, *J. Physiol. Paris* **98**, 315–330 (2004).
- [105] I. B. Yildiz, H. Jaeger, and S. J. Kiebel, “Re-visiting the echo state property”, *Neural Networks* **35**, 1–9 (2012).
- [106] N. Bertschinger and T. Natschläger, “Real-time computation at the edge of chaos in recurrent neural networks”, *Neural computation* **16**, 1413–1436 (2004).
- [107] R. Legenstein and W. Maass, “Edge of chaos and prediction of computational performance for neural circuit models”, *Neural Networks* **20**, 323–334 (2007).
- [108] B. Cramer, D. Stöckel, M. Kreft, M. Wibrals, J. Schemmel, K. Meier, and V. Priesemann, “Control of criticality and computation in spiking neuromorphic networks with plasticity”, *Nat. Commun.* **11**, 2853 (2020).

Bibliography

- [109] G. Marcucci, D. Pierangeli, and C. Conti, “Theory of Neuromorphic Computing by Waves: Machine Learning by Rogue Waves, Dispersive Shocks, and Solitons”, *Phys. Rev. Lett.* **125**, 093901 (2020).
- [110] N. A. Silva, T. D. Ferreira, and A. Guerreiro, “Reservoir computing with solitons”, *New J. Phys.* **23**, 023013 (2021).
- [111] D. J. Frantzeskakis, “Dark solitons in atomic Bose–Einstein condensates: from theory to experiments”, *J. Phys. A: Math. Theor.* **43**, 213001 (2010).
- [112] P. G. Kevrekidis and D. J. Frantzeskakis, “Solitons in coupled nonlinear Schrödinger models: A survey of recent developments”, *Rev. Phys.* **1**, 140–153 (2016).
- [113] K. E. Strecker, G. B. Partridge, A. G. Truscott, and R. G. Hulet, “Bright matter wave solitons in Bose–Einstein condensates”, *New J. Phys.* **5**, 73–73 (2003).
- [114] R. Penrose, “On best approximate solutions of linear matrix equations”, *Mathematical Proceedings of the Cambridge Philosophical Society* **52**, 17–19 (1956).
- [115] B. Schrauwen, D. Verstraeten, and J. Van Campenhout, “An overview of reservoir computing: theory, applications and implementations”, *Proceedings of the 15th European Symposium on Artificial Neural Networks*, 471–482 (2007).
- [116] B. Efron and R. J. Tibshirani, *An introduction to the bootstrap* (CRC press, 1994).
- [117] C. M. Bishop, *Pattern Recognition and Machine Learning* (Springer, 2006).
- [118] G. Gauthier, “Transport and Turbulence in Quasi-Uniform and Versatile Bose-Einstein Condensates”, PhD thesis (University of Queensland, 2020).
- [119] L. G. Wright, T. Onodera, M. M. Stein, T. Wang, D. T. Schachter, Z. Hu, and P. L. McMahon, “Deep physical neural networks trained with backpropagation”, *Nature* **601**, 549–555 (2022).
- [120] P. Kunkel, M. Prüfer, S. Lannig, R. Strohmaier, M. Gärttner, H. Strobel, and M. K. Oberthaler, “Detecting Entanglement Structure in Continuous Many-Body Quantum Systems”, *Phys. Rev. Lett.* **128**, 020402 (2022).

- [121] J. Sanz, A. Frölian, C. S. Chisholm, C. R. Cabrera, and L. Tarruell, “Interaction Control and Bright Solitons in Coherently Coupled Bose-Einstein Condensates”, *Phys. Rev. Lett.* **128**, 013201 (2022).
- [122] C. Viermann, M. Sparn, N. Liebster, M. Hans, E. Kath, Á. Parra-López, M. Tolosa-Simeón, N. Sánchez-Kuntz, T. Haas, H. Strobel, S. Floerchinger, and M. K. Oberthaler, *Quantum field simulator for dynamics in curved spacetime*, 2022, [arXiv:2202.10399](https://arxiv.org/abs/2202.10399).
- [123] G. H. Zhang, B. Braverman, A. Kawasaki, and V. Vuletić, “Note: Fast compact laser shutter using a direct current motor and three-dimensional printing”, *Rev. Sci. Instrum.* **86**, 126105 (2015).

Acknowledgements

Zum Abschluss dieser Arbeit möchte ich einigen Menschen danken, die es mir durch ihre Unterstützung ermöglicht haben diesen Punkt zu erreichen.

Zuerst danke ich Markus, der mich vor vielen Jahren in seine Gruppe aufgenommen und so für die Physik kalter Gase begeistert hat, dass ich mich nach meiner Bachelorarbeit auch zur Masterarbeit und Promotion mit ihnen beschäftigt habe. Danke für deine Unterstützung, deinen Einfallsreichtum und deine ansteckende Neugierde.

Special thanks to Lauriane Chomaz for reviewing this work, I am looking forward to interesting discussions.

Helmut danke ich für viele geduldige Erklärungen, die einmal mit dem Prinzip eines Wäscheleinenlangwellenradioempfängers angefangen und bis zu Operationsverstärkern wohl wenige Elektronik- oder Nichtelektronikthemen ausgelassen haben. Vielen Dank für die Zeit im Labor und dass du immer zur Stelle warst, wenn mal etwas schief gegangen ist. Du hast mich auch in schwierigen Situationen unterstützt und ich bin dankbar, dass ich so viel von dir lernen durfte.

Dem BECK Team danke ich für die gute Zusammenarbeit, die gemeinsamen Abende, spannende Diskussionen und die gute Zeit, die wir zusammen hatten. Danke an Ceila, Marius, Nikolas und Elinor für die vielen Jahre gemeinsamer Laborarbeit und eure Unterstützung. Es ist mir eine große Freude, das Experiment in gute Hände zu übergeben und ich bin gespannt, welche coolen Projekte dabei noch herauskommen. Vielen Dank auch an all unsere Bachelorstudent:innen, die mit ihren Projekten zum Erfolg des Experiments beigetragen haben, Alexander, Benedikt, Jan, Finn und Alexandra.

Liebes Experiment, auch wenn du diese Arbeit nie lesen wirst, danke ich dir, dass du über die Jahre gut durchgehalten hast und mit Vakuumproblemen

Acknowledgements

gewartet hast, bis meine Messungen abgeschlossen waren. Bitte sei meinen Nachfolgern gegenüber genauso zuvorkommend.

Danke an die gesamte Matterwave/SynQS Gruppe, ihr seid einfach ein cooler Haufen! Ob bei Frühstück, Weihnachtsfeier, Tagungen, Running Dinner, Abschlussfeiern, Fahrrad- oder Bootstour, danke für die schöne gemeinsame Zeit.

Dagmar und Christiane, vielen Dank für eure tatkräftige Unterstützung im Verwaltungsdschungel.

Vielen Dank an die feinmechanische Werkstatt, ohne die es das Experiment so nicht gäbe. Besonderer Dank gilt David, der viele Bauteile präzise gefertigt hat, auch zu später Stunde noch für uns da war und kreative Ideen mit eingebracht hat.

Felix, du bist nicht nur ein guter Freund und langjähriger Mitbewohner, sondern hast mir mit deinem Wissen zu Machine Learning sehr weiter geholfen. Vielen Dank für die vielen Erklärungen mit deren Hilfe ich das Experiment zum Rechnen bewegen konnte.

Zum Abschluss danke ich meiner ganzen Familie und Hanna, auf euch kann ich mich blind verlassen. Ich weiß euch immer an meiner Seite und bin dankbar für eure Unterstützung!